

**Micromanipulation
Using Dielectrophoresis:
Modeling and Real-Time
Optimization-Based Control**

Tomáš Michálek

**Czech Technical University in Prague
2020**

MICROMANIPULATION USING DIELECTROPHORESIS:

modeling and real-time
optimization-based control

Doctoral Thesis

Tomáš Michálek

This research was conducted under the auspices of the Czech Technical University in Prague and supported by the Czech Science Foundation within the project P206/12/G014 (Center for advanced bioanalytical technology).

Czech Technical University in Prague

Faculty of Electrical Engineering
Department of Control Engineering

MICROMANIPULATION USING DIELECTROPHORESIS:

modeling and real-time
optimization-based control

Doctoral Thesis

Tomáš Michálek

Prague, July 2020

Ph.D. Program: Electrical Engineering and Information Technology
Branch of Study: Control Engineering and Robotics

Advisor: doc. Ing. Zdeněk Hurák, Ph.D.

Tomáš Michálek
Micromanipulation Using Dielectrophoresis:
Modeling and Real-Time Optimization-Based Control
145 pages
PhD thesis, Czech Technical University in Prague,
Prague, Czech Republic
(2020)

The work was written in L^AT_EX using the Memoir class. The image on the cover and the images at the beginning of each chapter were obtained by stitching together over 100 automatically grabbed microscope photo snapshots.

Declaration

This doctoral thesis is submitted in partial fulfillment of the requirements for the degree of doctor (Ph.D.). The work submitted in this dissertation is the result of my own investigation, except where otherwise stated. I declare that I worked out this thesis independently and I quoted all used sources of information in accord with Methodical instructions of CTU in Prague about ethical principles for writing academic thesis. Moreover I declare that it has not already been accepted for any degree and is also not being concurrently submitted for any other degree.

Prague, 22nd July, 2020

Tomáš Michálek

Declaration

Abstract

This thesis describes a novel computational framework for position and orientation control of arbitrarily-shaped microscopic objects using dielectrophoresis. A suitable control-oriented model, that is, evaluable online (in real time) coupling the dielectrophoretic and hydrodynamic effects is derived. It can predict not only the dielectrophoretic force and torque but also the final translational and rotational velocities of micro-objects in a liquid medium. Subsequently, a control structure and model-based computational methods for design of a feedback controller are proposed. Finally, the functionality of the introduced framework is demonstrated in experiments. Discussion of important design and fabrication issues is included.

Keywords

noncontact micromanipulation, electrokinetics, dielectrophoresis, electrorotation, mathematical modeling, control system, feedback control, real-time optimization

Abstrakt

Tato práce popisuje nový výpočetní framework pro řízení pozice a orientace mikroskopických objektů libovolných tvarů pomocí dielektroforézy. V práci je odvozen matematický model vhodný pro účely řízení, tedy spočítatelný online (v reálném čase), zahrnující jak dielektroforetické, tak hydrodynamické fyzikální účinky. Díky tomu je možno spočítat nejen vyvozenou dielektroforetickou sílu a moment, ale i konečnou posuvnou a rotační rychlost mikroobjektu v kapalném prostředí. Následně je navržena řídicí struktura a na modelu založené výpočetní metody pro návrh zpětnovazebního regulátoru. Nakonec je funkčnost předloženého frameworku experimentálně demonstrována. Práce také zahrnuje diskuzi důležitých otázek návrhu a výroby použitých experimentálních zařízení.

Klíčová slova

bezkontaktní mikromanipulace, elektrokinetika, dielektroforéza, elektrorotace, matematické modelování, řídicí systém, zpětnovazební řízení, optimalizace v reálném čase

Contents

Declaration	i
Abstract	iii
1 Introduction	1
2 Dielectrophoretic model for a sphere	21
3 Dielectrophoretic model of arbitrarily-shaped object	43
4 Hydrodynamic model of arbitrarily-shaped object	75
5 Manipulation of arbitrarily-shaped micro-objects	101
6 Conclusion	127
Summary	137
List of publications	139
Acknowledgements	143
About the author	145



A Tetrakis-shaped micro-object resting
on an euro cent coin

CHAPTER 1

Introduction

The microscopic world is a fascinating place. Since the invention of a microscope approximately 400 years ago, people were attracted to this kind of a new universe and particularly to all of the tiny biological creatures living there that nobody could see before. With the following further advances in optics, this new world became suddenly wide open for scientific exploration.

1.1 Miniaturization and newly emerged opportunities at microworld

The newly gained ability to see smaller things also enabled the construction of miniature machines utilized for a long time mainly just in the domain of watchmaking. It was at the end of 1959, when Richard Feynman in his famous talk “There’s Plenty of Room at the Bottom” draw attention to the many of, back then, unexplored applications related to miniaturization. These included topics like space-efficient information storage, creation of nano-scale machines for micro-fabrication, computing, or even medical care. He argued that many of the proposed ideas, whatever crazy they can sound, should be feasible and in compliance with all the known physical laws. The Albert R. Hibbs’s idea of a miniature mechanical surgeon operating inside the human body, also mentioned in the Feynman’s talk, was in 1966 even adapted for a science-fiction movie *Fantastic Voyage* (and even later once again for a movie *Innerspace*). The story follows an adventure of a small team operating a submarine, which is miniaturized and injected into the body of a dying scientist. Their goal is to save his life by surgical intervention in an otherwise inaccessible part of his brain.

From the 1950’s, the miniaturization is strongly connected with the advances in computer technology. At that epoch started the manufacturing of integrated circuits and further miniaturization of electromechanical devices

and their components, which continues today.

The utilization of other than just semiconductor materials (such as polymeric and metallic) led to the construction of the so-called *hybrid microsystems* featuring increased performance and functionality over their macro-scale counterparts [1, 2]. The only thing that limits their massive appearance on a market is that the assembly process is not yet fully automatized and thus prohibitively expensive.

Furthermore, there is a rising interest in tools capable of automatized manipulation with biological micro-objects like cells ranging in size from $1\ \mu\text{m}$ to $100\ \mu\text{m}$. Replacement of conventional analytical techniques by a low cost, higher-throughput lab-on-a-chip devices opens yet another broad set of applications related to biology and medical sciences [3].

1.2 Micro-manipulation

Starting with the analysis of biological samples and ending with the assembly of artificially-made components into functional units, micro-manipulation is obviously a naturally required task. The ability to move and orient the micro-object of interest in the desired way not only dramatically facilitates its study, but it can also pave the way for many exciting applications sketched above.

New challenges as a consequence of scaling laws

Although the usage of conventional tweezers historically worked to some extent, with the rising magnification of microscopes and decreasing size of objects of interest, it began evident that some more specialized tools will be needed. Moreover, such manipulation using a hand-held tweezer is exhausting, especially when done repeatedly on many samples. But couldn't we just miniaturize and use the conventional robotic manipulators? What makes the micro-manipulation such a difficult problem?

As the objects shrink in size, different physical phenomena enter the game. Since the volume scales as $\sim L^3$, while the surface area scales as $\sim L^2$, where L is a characteristic length of object, the proportion between surface and volume related physical effects changes. Thus, for example, friction, and surface forces become more critical than inertia, weight, and body forces when shrinking the dimensions of objects [2, 4–7]. This has many consequences in the shape and behavior of micro-organisms [8, 9] and

it also brings new engineering challenges related to micromanipulation. The micro-objects, for example, tend to “stick” to the manipulation tools (e.g., tweezers), and thus although we can grab some object, it is then difficult to release it.

As a result, the manipulation principles known from the macro-scale can not be adapted entirely. Novel approaches either trying to avoid or overcome these surface effects or, on the contrary, to take advantage of them, need to be developed.

Contact vs. non-contact manipulation

The currently proposed solutions can be categorized into two classes: *contact* and *non-contact* (or *contact-free*). In the former, there is some tool that directly touches the micro-object. In the latter, it is actuated remotely, for example, through fluid flow or some physical fields exerting force directly on the object of interest. Each of them has its advantages and disadvantages, and each of them is suitable for different purposes.

Generally, one has to always take into account the material of manipulated micro-objects, their structural properties and requirements posed on their handling. Sometimes the shape of the objects or roughness of its surface prevents it from being reliably gripped by a contact-based manipulator. In other cases, the micro-object of interest might be harmed by its exposure to electric or magnetic fields [1]. The speed of manipulation, the pressure applied to the object, or parallelization possibilities may play an important role.

The contact-based approaches usually utilize well developed and already commercially available single or multi-axis manipulation piezo or stepper motor driven stages capable of sub-micron resolution with a working range of several millimeters or even centimeters [4]. These manipulators are equipped with a specialized tool like micro-pipette or micro-gripper capable of handling the object of interest. The possibilities of actuation include electrostatic or capillary attraction, utilization of the liquid-solid phase change, adhesive, vacuum, or classical friction grippers [1]. The last-mentioned can be actuated, for example, using electrostatics, thermal expansion, piezoelectrics, magnetism, or shape memory alloys [4]. Once the micro-object is grabbed and moved to its desired location, it can be released utilizing, for example, mechanical vibrations, some other auxiliary tool, electric re-

pulsion, pressure pulse, or rolling, to name a few of the developed release strategies [1].

The problem of the object's release is entirely overcome by the non-contact manipulation approaches. These approaches, however, often require the manipulated object to have some specific material properties so that the underlying physical phenomena can be used. The investigated principles include various electrokinetic effects, utilization of magnetic field, optical or acoustic pressure, and controlled fluid flow [1].

1.3 Dielectrophoresis

In this work we focus on the non-contact micro-manipulation and specifically on a manipulation utilizing the electrokinetic effect of *dielectrophoresis* (DEP). First described by Pohl [10] in 1951, it is a phenomena that causes the polarizable (but uncharged) objects to move due to the presence of an inhomogeneous electric field. This movement is a result of Coulomb forces acting on a newly emerged charge structure inside of and in a close vicinity of the polarized object. At the macro-scale, this effect is responsible, for example, for the attraction of uncharged pieces of paper to a comb with which somebody previously rubbed his hair.

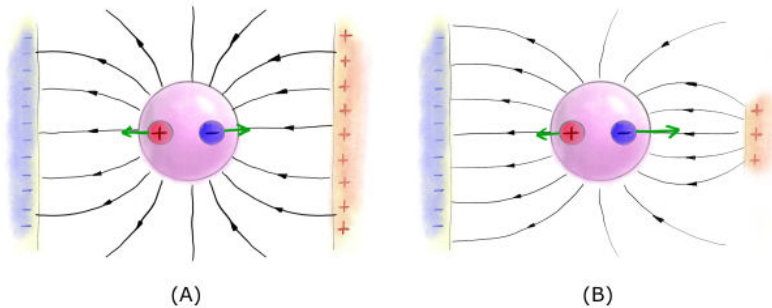


Figure 1.1: A simplified illustration of the DEP principle—the polarization induced charge structure is represented by an equivalent electric dipole (which is possible for a sphere). The black lines represent the electric field lines. The green arrows represent the Coulomb forces acting on individual charges. Cases of A) homogeneous, and B) inhomogeneous external fields are shown.

The above described is in a simplified way illustrated in Fig. 1.1, where a polarizable sphere is placed in between two electrodes generating the electric field. It is shown here that the requirement of the field's inhomogeneity is crucial since otherwise, all of the Coulomb forces would altogether cancel each other. In Fig. 1.1A, the sphere is surrounded by a homogeneous electric field leading to the cancellation of the forces acting on the individual charges of a formed dipole. Whereas in Fig. 1.1B, there is a sphere located in an inhomogeneous electric field, giving a rise to a net DEP force propelling the object.

The polarizing electric field for DEP is generated by harmonic voltage signals to avoid other unwanted electrokinetic behavior like electrolysis or electrophoresis (interaction between the external field and an intrinsic charge potentially present inside the object). Based on the properties of materials of the object and the surrounding medium (usually some liquid), the DEP force attracts or repels the object from the region of high electric field intensity. These two situations are denoted as *positive* and *negative* DEP, respectively. Although initially, the term DEP referred strictly to just this type of the electrokinetic behavior induced by a spatially varying magnitude of the electric field, nowadays it covers much wider spectrum of closely related electrokinetic effects. We thus call the above-described phenomenon more specifically as *conventional DEP* (cDEP).

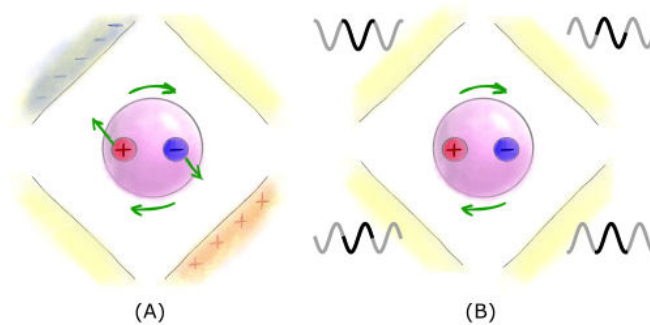


Figure 1.2: A) electroorientation (OR), B) electrorotation (ROT)

Besides the cDEP, we distinguish the *traveling-wave DEP* (twDEP), which arises rather from a spatially varying phase of the electric field. If the micro-object is not spherical, it orients itself along the lines of the un-

derlying electric field. This mechanism of torque generation is denoted as *electroorientation* (EO). In the case of a permanently rotating electric field, the objects constantly strive for orienting along the field lines resulting in the so-called *electrorotation* (ROT). Both EO and ROT are visualized in Fig. 1.2A and Fig. 1.2B, respectively. A single term *generalized DEP* (gDEP) is sometimes used for all of the above mentioned modes [11]. Other, separately investigated, uses of DEP include insulator based DEP (iDEP) [12, 13], and *multiple frequency DEP* (mfDEP) [14], with which we will not deal in this work. A more detailed explanation of DEP and all the related phenomena is given in excellent texts [15–20].

What sets the DEP apart from the other mentioned approaches to non-contact micro-manipulation is a combination of several factors. The DEP does not pose any substantial requirements on the material of the micro-objects. It is sufficient for them to belong to a quite broad class of polarizable objects. The whole necessary instrumentation can be miniaturized down to a single printed circuit board, which enables us to truly fulfill the lab-on-a-chip paradigm rather than to create another chip-in-the-lab apparatus. Lastly, although not for prolonged periods, DEP can be used with living biological cells without causing them any damage [21].

Current DEP applications

The biocompatibility of DEP is proved by a wide range of biological and biomedical applications. The standard use of DEP includes, for example, selective isolation of cell subpopulations without the need of any biochemical labels or tags as opposed to the conventional flow cytometry or magnetic bead-coupled cell separation. This makes the process easier, faster, and cheaper and also less intruding since the cells are not influenced by the presence of the bioengineering tags any more [20]. The use of DEP was reported, for example, in differentiation, fractionation, isolation, and sorting of stem-cells [20], in bacteria, virus, mycoses, and oncology research [22, 23], in manipulation of DNA [24, 25] and proteins [26], in targeted drug delivery, and in in-vivo tissue engineering [27]. A great review of these and other applications is given, for example, in [20, 28, 29]. Other uses of DEP include environmental and polymer research, or biosensing.

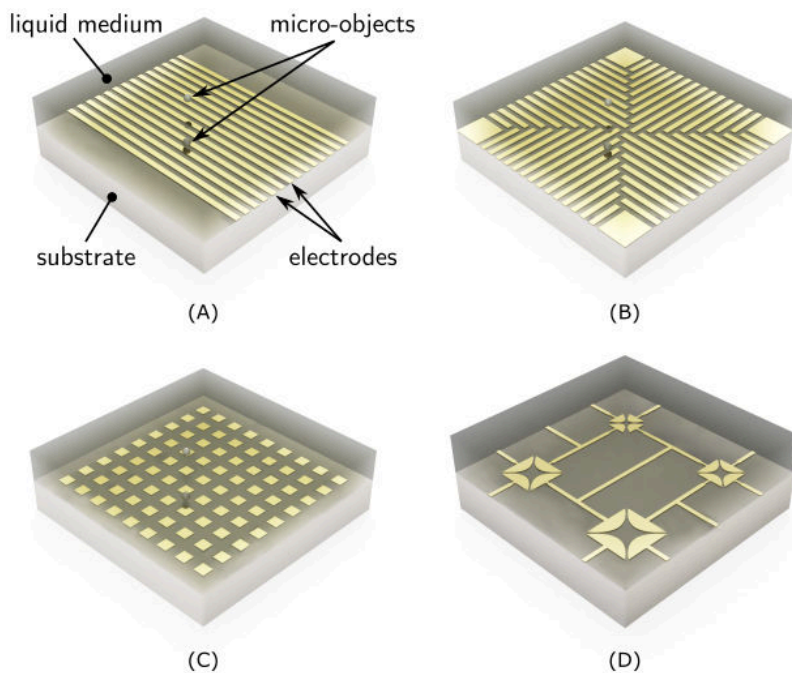


Figure 1.3: Examples of various layouts of electrodes used in DEP manipulators. Namely, A) parallel, B) four-sector, C) matrix, and D) quadrupolar electrode array.

Arrangement of a DEP based manipulator

The typical arrangement of the DEP-based micro-manipulator is shown in Fig. 1.3A. The micro-objects are placed in a liquid medium enclosed in a miniature container, which defines the manipulation space. The floor of this container is patterned with micro-electrodes—planar structures etched into a thin conductive layer—used for generation of the polarizing inhomogeneous electric field. In negative DEP, utilized in this work, the micro-object is essentially repelled from the high-electric field intensity locations at the edges of the electrodes. As a result, it levitates in the fluid above the electrodes.

The specific structure and size of the micro-electrodes define the achievable “profiles” of electric field intensity and, as a consequence, the manipulator capabilities to transport objects in various directions. For example, the parallel layout used in Fig. 1.3A permits only the movement perpendic-

ular to the electrode stripes. Figure 1.3B shows an electrode array obtained by a clever combination of four segments with parallel electrodes called *four-sector electrode array*. This arrangement of electrodes enables us to move the object in any direction as long as it resides in the central area. The farther the object is from the center of the electrode array, the more its movement capabilities resemble the ones of the parallel electrode array. The structure, which is shown in Fig. 1.3C would then enable us to steer the object in any direction no matter where it is located. However, as opposed to the four-sector array, this electrode layout can not be fabricated using just single layer technology, and it is thus more costly. In this thesis, yet another special arrangement of electrodes is used. Figure 1.3D shows four instances of the *quadrupolar electrode array*, typically used for ROT. In this case, the object of interest does not hover above and travel across the electrodes, but it is rather located and manipulated in the space in between them.

The range of achievable translation in electrode arrays in Fig. 1.3A-C is naturally given by the area covered by the electrode pattern. If a large number of electrodes is used, the manipulation space can span an area as large as we want.

As described above, the motion of the manipulated micro-object is a result of the DEP force and torque, which themselves are created by the inhomogeneous electric field. The field is generated and controlled by applying suitable voltage signals to the electrodes. Determination of these voltages is a responsibility of the control algorithm.

Control approaches

In the biological and biomedical applications mentioned above, the DEP is mostly used in an open-loop regime. Some specific predefined voltage signals are applied to the electrodes and then remain intact during the whole process. The selectivity in the separation or trapping tasks is thus given solely by the difference in their electrical properties. Some of these manipulation methods, including separation, transportation, trapping and sorting are reviewed in [3, 30–32].

Although a camera mounted on a microscope is used in many of the open-loop studies, it always serves just for inspection and recording of the experiment. By processing the image in real-time, one can, for example, automatically determine the position or type of the micro-objects and utilize

this information for further decision making. This closes the feedback loop around the system.

With feedback, it is, for example, possible to use DEP for sorting of subpopulations just based on the visual appearance of the micro-objects, not their electrical properties. If the object belongs to a specific group of interest, a kind of DEP “railroad” switch could be activated pulling the object out of the main stream of the micro-fluidic channel and storing it in some collector for later inspection. Another application of visual feedback is steering of the micro-objects to specific places or along specified trajectories. Knowing the current and the target location of the object, the system could determine in which direction a DEP force should be exerted and change the driving voltages on the micro-electrodes accordingly. This was shown, for example, in [33–35] and even in a commercially available product called *DEPArray* [36]. In all of these cases, a specific pattern of voltage signals is used to attract the micro-object and to trap it at one of a discrete set of locations. By moving the “DEP trap” to a close enough neighboring position, the micro-object will follow it. By repeating this process, it is therefore possible to translate the object between a regular grid of stable locations. The achievable positioning resolution of such a trap-based manipulator will, however, be always limited by the density of the used electrode pattern.

In [37], the authors demonstrated simultaneous manipulation of several micro-objects in 1D by controlling the amplitude of voltage signals applied to a set of parallel electrodes. Later, this work was extended to micro-manipulation in two dimensions [38]. This was enabled by a novel design of electrodes and by an application of control utilizing phase-shifts between the voltage signals, rather than adjustment of their amplitudes, which has positive practical consequences. Edwards and Engheta demonstrated in [39] simultaneous position and orientation control of a single nanorod in a space encompassed by five circular electrodes. Later, in [40], the same group demonstrated simultaneous independent manipulation with two spherical micro-object along complex trajectories. Other examples of feedback closed-loop control can be seen in [41, 42] by Kharboutly et al. Contrary to the trap-based approaches, in all of these works, the position of the micro-object is not limited to any discrete grid. This is achieved by using more general input voltage configurations to be applied to the electrodes. There is no more any finite “alphabet” of potential configurations to be used. This makes the control problem far more difficult to solve since the controller

has to provide in real-time the tailored voltage signals, which should be applied to the electrodes based on the current situation. This work extends the current capabilities of this type of manipulation system.

The DEP manipulation systems, and generally most of the other micro-manipulation approaches, lack the dynamics we are habituated to from the macro scale. Due to the small mass of the micro-objects, their inertia does not play such an important role and can be effectively neglected. When there is some difference in electric potential between the electrodes, a force and torque are exerted on the object, which immediately starts moving. Bringing all the electrodes to the same potential causes the force and torque to vanish and the object to stop moving immediately. From the control point-of-view, it is the nonlinear behavior of the system embodied in the DEP itself, which makes it challenging to control.

Control-oriented modeling

For control purposes, a rapid evaluation of the model may be a necessity, especially when it is not used only for the design of a controller, but when it directly forms its part. As such, it may be evaluated even many times during a single control period lasting, for example, just a fraction of a second on its own. Often a trade-off between the computational speed and the accuracy of model predictions has to be made. Nevertheless, all of the significant and dominant physical effects need to be taken into account.

In the described scenario of DEP micro-manipulation, these are namely the DEP force itself, gravity, buoyancy, and hydrodynamics at low Reynolds number. The first three, when combined, rule the force and torque acting on the object of interest, and the last one determines what translational and rotational speeds of the object will cause this force and torque. The influence of other physical effects, like Brownian motion, diffusion, thermal gradients, and others, are discussed in [43].

As it will be shown in the subsequent chapters of this thesis, the most challenging part is the computation of the DEP force and torque themselves. As noted above, the awareness of the DEP phenomenon is not new, and its physical aspects are already well described. There exist two basic modeling schemes for DEP force simulations—the Maxwell Stress Tensor (MST) method [44] and the effective multipole method (EM) [45, 46]. The former one is now considered as the most rigorous approach to DEP force

calculation, while the latter one is just its approximation to a chosen level. This relation between the MST and EM is shown in [47].

Although the MST model provides a way to calculate the DEP force accurately under any possible scenario, its evaluation is time demanding. A finite element method (FEM) has to be usually employed. It is, therefore, not particularly well suitable for control purposes. When combined with an efficient method of electric field computation like [48–52], the EM is much more promising. The only problem is that up to now, only spherical objects could be treated, which severely limited the use of the method. This is one of the problems solved in this thesis.

1.4 Goals of the thesis

The goal of this work was to create a computational framework and experimental system for a micro/mesoscale noncontact manipulation using dielectrophoresis, keeping the envisioned scientific (mostly biological) and engineering applications (e.g. micro-assembly) in mind. Since many of the biological objects are non-spherical (red blood cells are the obvious example), and so are the artificially made components for micro-assembly, such a system should handle objects of arbitrary shapes and to control not only their position but also their orientation.

1.5 Foundations of the thesis

This work is a continuation of the still ongoing research of the Advanced Algorithms for Control and Communication (AA4CC) research group at the Department of control engineering at the Faculty of electrical engineering, Czech Technical University in Prague. This research is documented by a series of bachelor [53–55], masters [56–59] and dissertation theses [60] and related journal [37, 38, 49, 61] and conference papers [62], some of which were authored or co-authored by me. Namely, in [54], I utilized a modeling approach based on a method of moments to simulate a DEP force above a matrix electrode array and use the gained insight for the design and testing of a couple of position controllers. In [57], I presented the optimization-based feedback simultaneous and independent control of several spherical micro-objects. This work resulted in journal publications [37] and [38] describing the 1D and 2D cases, respectively.

1.6 Brief content of the following chapters

The work is documented in the subsequent four chapters, each of them corresponding to an either already published or a submitted journal paper. Chapter 2 reviews and compares the available approaches for modeling the DEP force acting on spherical objects. Particular interest is dedicated to a case when the object is of a comparable size and relatively close (up to the sphere's diameter) to the electrodes. In chapter 3, a control-oriented DEP model for arbitrarily-shaped and possibly even inhomogeneous objects is derived. This model is coupled with a control-oriented model of hydrodynamics in chapter 4, so it could be used for predicting the motion of the micro-objects in a fluidic environment. The complete model is validated against experimental observations using a quadrupolar electrode array and parameterized ROT experiments. Finally, in chapter 5, a feedback control system using real-time optimization is presented, which is capable of simultaneous and independent control of position and orientation of arbitrarily-shaped micro-objects. This is demonstrated in a series of experiments involving position and orientation control of several Tetris-shaped SU-8 micro-objects. Video from this final experiment is available at https://youtu.be/SBepX_Xk1BM. The work concludes by a general discussion and prospect of future research directions.

1.7 Bibliography

- [1] S. Ruggeri, G. Fontana, and I. Fassi. Micro-assembly. In I. Fassi and D. Shipley, editors, *Micro-Manufacturing Technologies and Their Applications*, chapter 9, pages 223–259. Springer, Cham, January 2017. ISBN 978-3-319-39651-4. doi: 10.1007/978-3-319-39651-4.
- [2] W. S. N. Trimmer. Microrobots and micromechanical systems. *Sensors and Actuators*, 19(3):267–287, September 1989. ISSN 0250-6874. doi: 10.1016/0250-6874(89)87079-9.
- [3] C. H. Kua, Yee Cheong Lam, C. Yang, and Kamal Youcef-Toumi. Review of bio-particle manipulation using dielectrophoresis. *Singapore-MIT Alliance*, January 2005.
- [4] Jake J. Abbott, Zoltan Nagy, Felix Beyeler, and Bradley J. Nelson. Robotics in the Small, Part I: Microbotics. *IEEE Robotics Au-*

-
- tomation Magazine*, 14(2):92–103, June 2007. ISSN 1558-223X. doi: 10.1109/mra.2007.380641.
- [5] M. Sitti. *Mobile Microrobotics*. Intelligent Robotics and Autonomous Agents series. MIT Press, 2017. ISBN 9780262036436.
- [6] Claudia Pagano and Irene Fassi. Introduction to Miniaturisation. In Irene Fassi and David Shipley, editors, *Micro-Manufacturing Technologies and Their Applications: A Theoretical and Practical Guide*, Springer Tracts in Mechanical Engineering, pages 1–22. Springer International Publishing, Cham, 2017. ISBN 978-3-319-39651-4. doi: 10.1007/978-3-319-39651-4_1.
- [7] Michel Wautelet. Scaling laws in the macro-, micro- and nanoworlds. *European Journal of Physics*, 22(6):601–611, October 2001. ISSN 0143-0807. doi: 10.1088/0143-0807/22/6/305.
- [8] E. M. Purcell. Life at low Reynolds number. *American Journal of Physics*, 45(1):3–11, January 1977. ISSN 0002-9505. doi: 10.1119/1.10903.
- [9] Igor Paprotny and Sarah Bergbreiter. Small-Scale Robotics : An Introduction. In Igor Paprotny and Sarah Bergbreiter, editors, *Small-Scale Robotics. From Nano-to-Millimeter-Sized Robotic Systems and Applications*, Lecture Notes in Computer Science, pages 1–15, Berlin, Heidelberg, 2014. Springer. ISBN 978-3-642-55134-5. doi: 10.1007/978-3-642-55134-5_1.
- [10] Herbert A. Pohl. The Motion and Precipitation of Suspensoids in Divergent Electric Fields. *Journal of Applied Physics*, 22(7):869–871, July 1951. ISSN 0021-8979. doi: 10.1063/1.1700065.
- [11] X.-B. Wang, Y. Huang, F. F. Becker, and P. R. C. Gascoyne. A unified theory of dielectrophoresis and travelling wave dielectrophoresis. *Journal of Physics D: Applied Physics*, 27(7):1571–1574, July 1994. ISSN 0022-3727. doi: 10.1088/0022-3727/27/7/036.
- [12] Claire V. Crowther and Mark A. Hayes. Refinement of Insulator-based Dielectrophoresis. *The Analyst*, 142(9):1608–1618, May 2017. ISSN 0003-2654. doi: 10.1039/c6an02509a.
-

- [13] Blanca H. Lapizco-Encinas. On the recent developments of insulator-based dielectrophoresis: A review. *ELECTROPHORESIS*, 40(3):358–375, 2019. ISSN 1522-2683. doi: 10.1002/elps.201800285.
- [14] Mario Urdaneta and Elisabeth Smela. Multiple frequency dielectrophoresis. *ELECTROPHORESIS*, 28(18):3145–3155, 2007. ISSN 1522-2683. doi: 10.1002/elps.200600786.
- [15] Ronald R. Pethig. *Dielectrophoresis: Theory, Methodology and Biological Applications*. Wiley, Hoboken, NJ, 1 edition edition, May 2017. ISBN 978-1-118-67145-0.
- [16] Thomas B. Jones and Thomas Byron Jones. *Electromechanics of Particles*. Cambridge University Press, September 2005. ISBN 978-0-521-01910-1. doi: 10.1017/cbo9780511574498.
- [17] Hywel Morgan and Nicolas G. Green. *AC Electrokinetic: Colloids and Nanoparticles*. Research Studies Pr, Philadelphia, PA, 1st edition edition, June 2002. ISBN 978-0-86380-255-3.
- [18] Michael Pycraft Hughes. *Nanoelectromechanics in Engineering and Biology*. CRC Press, October 2002. ISBN 978-0-8493-1183-3.
- [19] T.B. Jones. Basic theory of dielectrophoresis and electrorotation. *IEEE Engineering in Medicine and Biology Magazine*, 22(6):33–42, November 2003. ISSN 1937-4186. doi: 10.1109/MEMB.2003.1304999.
- [20] Ronald Pethig, Anoop Menachery, Steve Pells, and Paul De Sousa. Dielectrophoresis: A Review of Applications for Stem Cell Research. *Journal of Biomedicine & Biotechnology*, pages 1–7, January 2010. ISSN 11107243. doi: 10.1155/2010/182581.
- [21] Khashayar Khoshmanesh, Jin Akagi, Saeid Nahavandi, Joanna Skommer, Sara Baratchi, Jonathan M. Cooper, Kouros Kalantar-Zadeh, David E. Williams, and Donald Wlodkovic. Dynamic analysis of drug-induced cytotoxicity using chip-based dielectrophoretic cell immobilization technology. *Analytical Chemistry*, 83(6):2133–2144, March 2011. ISSN 1520-6882. doi: 10.1021/ac1029456.

-
- [22] Liju Yang. A Review of Multifunctions of Dielectrophoresis in Biosensors and Biochips for Bacteria Detection. *Analytical Letters*, 45(2-3):187–201, January 2012. ISSN 0003-2719. doi: 10.1080/00032719.2011.633182.
- [23] Peter R. C. Gascoyne and Sangjo Shim. Isolation of Circulating Tumor Cells by Dielectrophoresis. *Cancers*, 6(1):545–579, March 2014. doi: 10.3390/cancers6010545.
- [24] Martina Viefhues and Ralf Eichhorn. DNA dielectrophoresis: Theory and applications a review. *ELECTROPHORESIS*, 38(11):1483–1506, 2017. ISSN 1522-2683. doi: 10.1002/elps.201600482.
- [25] R. Hölzel and F. F. Bier. Dielectrophoretic manipulation of DNA. *IEE Proceedings - Nanobiotechnology*, 150(2):47–53, November 2003. ISSN 1740-9748. doi: 10.1049/ip-nbt:20031006.
- [26] Asuka Nakano and Alexandra Ros. Protein dielectrophoresis: Advances, challenges, and applications. *ELECTROPHORESIS*, 34(7): 1085–1096, 2013. ISSN 1522-2683. doi: 10.1002/elps.201200482.
- [27] Gerard H. Markx. The use of electric fields in tissue engineering. *Organogenesis*, 4(1):11–17, January 2008. ISSN 1547-6278. doi: 10.4161/org.5799.
- [28] Nurhaslina Abd Rahman, Fatimah Ibrahim, and Bashar Yafouz. Dielectrophoresis for Biomedical Sciences Applications: A Review. *Sensors*, 17(3):449, March 2017. doi: 10.3390/s17030449.
- [29] Ronald Pethig and Gerard H. Markx. Applications of dielectrophoresis in biotechnology. *Trends in Biotechnology*, 15(10):426–432, October 1997. ISSN 0167-7799. doi: 10.1016/S0167-7799(97)01096-2.
- [30] Peter R. C. Gascoyne and Jody Vykoukal. Particle separation by dielectrophoresis. *ELECTROPHORESIS*, 23(13):1973–1983, 2002. ISSN 1522-2683. doi: 10.1002/1522-2683(200207)23:13<1973::aid-elps1973>3.0.co;2-1.
- [31] Swagatika Dash and Swati Mohanty. Dielectrophoretic separation of micron and submicron particles: A review. *ELECTROPHORESIS*, 35(18):2656–2672, 2014. ISSN 1522-2683. doi: 10.1002/elps.201400084.
-

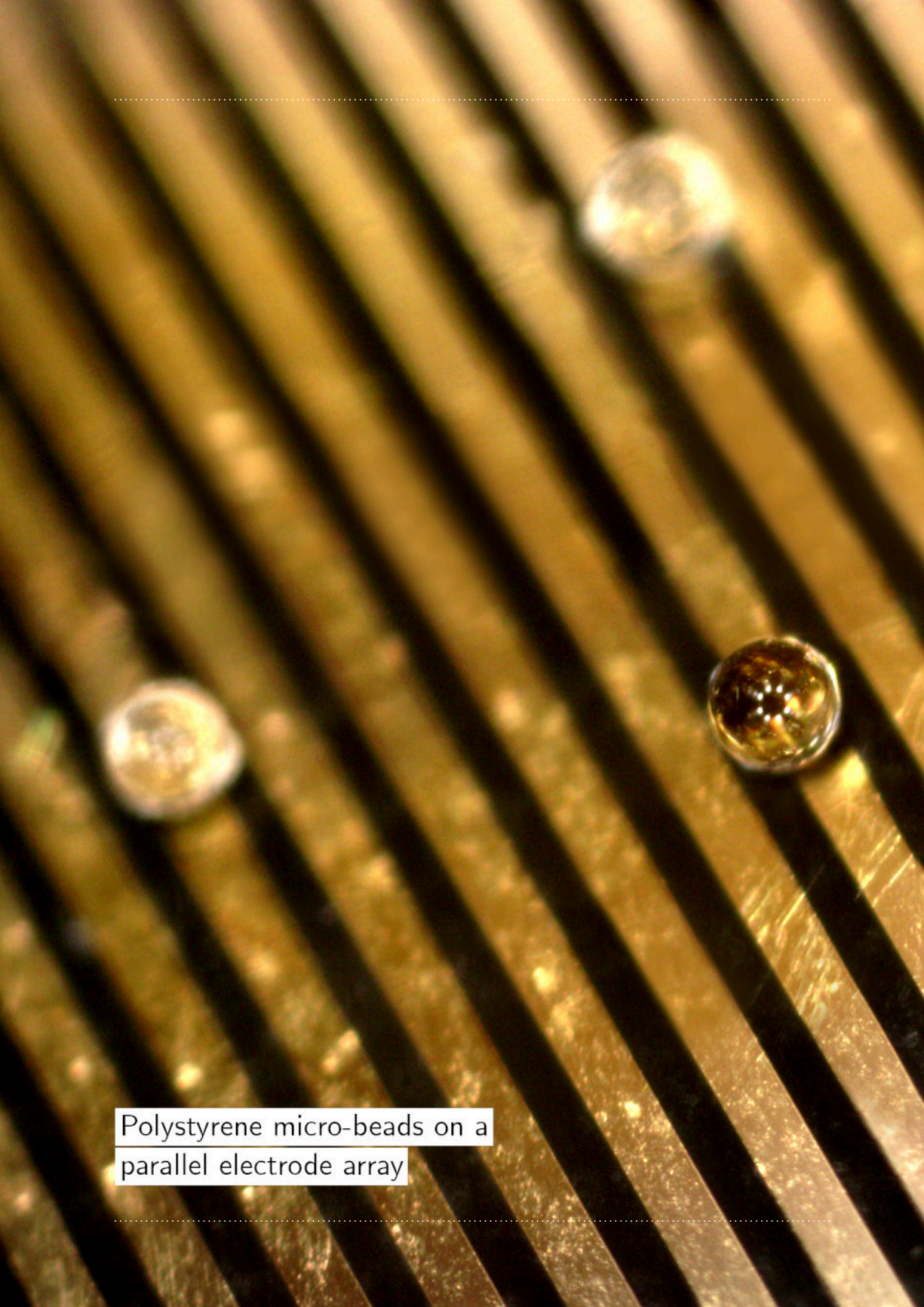
- [32] Talukder Z. Jubery, Soumya K. Srivastava, and Prashanta Dutta. Dielectrophoretic separation of bioparticles in microdevices: A review. *ELECTROPHORESIS*, 35(5):691–713, 2014. ISSN 1522-2683. doi: 10.1002/elps.201300424.
- [33] Junya Suehiro and Ronald Pethig. The dielectrophoretic movement and positioning of a biological cell using a three-dimensional grid electrode system. *Journal of Physics D: Applied Physics*, 31(22):3298–3305, November 1998. ISSN 0022-3727. doi: 10.1088/0022-3727/31/22/019.
- [34] N. Manaresi, A. Romani, G. Medoro, L. Altomare, A. Leonardi, M. Tartagni, and R. Guerrieri. A CMOS chip for individual cell manipulation and detection. *IEEE Journal of Solid-State Circuits*, 38(12):2297–2305, December 2003. ISSN 1558-173X. doi: 10.1109/JSSC.2003.819171.
- [35] G. Medoro, N. Manaresi, A. Leonardi, L. Altomare, M. Tartagni, and R. Guerrieri. A lab-on-a-chip for cell detection and manipulation. *IEEE Sensors Journal*, 3(3):317–325, June 2003. ISSN 2379-9153. doi: 10.1109/JSEN.2003.814648.
- [36] Menarini Silicon Biosystems. Menarini Silicon Biosystems, A Menarini Group Company- Home. URL <http://www.siliconbiosystems.com>.
- [37] Jiří Zemánek, Tomáš Michálek, and Zdeněk Hurák. Feedback control for noise-aided parallel micromanipulation of several particles using dielectrophoresis. *ELECTROPHORESIS*, 36(13):1451–1458, July 2015. ISSN 1522-2683. doi: 10.1002/elps.201400521.
- [38] Jiří Zemánek, Tomáš Michálek, and Zdeněk Hurák. Phase-shift feedback control for dielectrophoretic micromanipulation. *Lab on a Chip*, 18(12):1793–1801, 2018. ISSN 1473-0197. doi: 10.1039/c8lc00113h.
- [39] Brian Edwards, Nader Engheta, and Stephane Evoy. Electric tweezers: Experimental study of positive dielectrophoresis-based positioning and orientation of a nanorod. *Journal of Applied Physics*, 102(2):024913, July 2007. ISSN 0021-8979. doi: 10.1063/1.2753584.
- [40] B. Edwards and N. Engheta. Electric tweezers: negative dielectrophoretic multiple particle positioning. *New Journal of Physics*,

14(6):063012, June 2012. ISSN 1367-2630. doi: 10.1088/1367-2630/14/6/063012.

- [41] Mohamed Kharboutly and Michaël Gauthier. High speed closed loop control of a dielectrophoresis-based system. In *2013 IEEE International Conference on Robotics and Automation*, pages 1446–1451. IEEE, May 2013. doi: 10.1109/ICRA.2013.6630761. ISSN: 1050-4729.
- [42] Mohamed Kharboutly, Michaël Gauthier, and Nicolas Chaillet. Predictive control of a micro bead’s trajectory in a dielectrophoresis-based device. In *2010 IEEE/RSJ International Conference on Intelligent Robots and Systems*, pages 5616–5621. IEEE, October 2010. doi: 10.1109/IROS.2010.5650669. ISSN: 2153-0858.
- [43] A. Ramos, H. Morgan, N. G. Green, and A. Castellanos. Ac electrokinetics: a review of forces in microelectrode structures. *Journal of Physics D: Applied Physics*, 31(18):2338, September 1998. ISSN 0022-3727. doi: 10.1088/0022-3727/31/18/021.
- [44] H. Fröhlich and F. Kremer, editors. *Coherent Excitations in Biological Systems*. Proceedings in Life Sciences. Springer-Verlag, Berlin Heidelberg, 1983. ISBN 978-3-642-69188-1. doi: 10.1007/978-3-642-69186-7.
- [45] T. B. Jones and Masao Washizu. Multipolar dielectrophoretic and electrorotation theory. *Journal of Electrostatics*, 37(1):121–134, May 1996. ISSN 0304-3886. doi: 10.1016/0304-3886(96)00006-x.
- [46] Masao Washizu and T. B. Jones. Multipolar dielectrophoretic force calculation. *Journal of Electrostatics*, 33(2):187–198, September 1994. ISSN 0304-3886. doi: 10.1016/0304-3886(94)90053-1.
- [47] Xujing Wang, Xiao-Bo Wang, and Peter R. C. Gascoyne. General expressions for dielectrophoretic force and electrorotational torque derived using the Maxwell stress tensor method. *Journal of Electrostatics*, 39(4):277–295, August 1997. ISSN 0304-3886. doi: 10.1016/S0304-3886(97)00126-5.
- [48] Xujing Wang, Xiao-Bo Wang, F. F. Becker, and Peter R. C. Gascoyne. A theoretical method of electrical field analysis for dielectrophoretic electrode arrays using Green’s theorem. *Jour-*

- nal of Physics D: Applied Physics*, 29(6):1649–1660, June 1996. ISSN 0022-3727. doi: 10.1088/0022-3727/29/6/035.
- [49] Martin Gurtner, Kristian Hengster-Movric, and Zdeněk Hurák. Green’s function-based control-oriented modeling of electric field for dielectrophoresis. *Journal of Applied Physics*, 122(5):054903, August 2017. ISSN 0021-8979. doi: 10.1063/1.4997725.
- [50] Hywel Morgan, Alberto García Izquierdo, David Bakewell, Nicolas G. Green, and Antonio Ramos. The dielectrophoretic and travelling wave forces generated by interdigitated electrode arrays: analytical solution using Fourier series. *Journal of Physics D: Applied Physics*, 34(10):1553–1561, May 2001. ISSN 0022-3727. doi: 10.1088/0022-3727/34/10/316.
- [51] Vladimir Gauthier, Aude Bolopion, and Michaël Gauthier. Analytical Formulation of the Electric Field Induced by Electrode Arrays: Towards Automated Dielectrophoretic Cell Sorting. *Micromachines*, 8(8):253, August 2017. ISSN 2072-666X. doi: 10.3390/mi8080253.
- [52] Mohamed Kharboutly, Michaël Gauthier, and Nicolas Chaillet. Modeling the trajectory of a microparticle in a dielectrophoresis device. *Journal of Applied Physics*, 106(11):114312, December 2009. ISSN 0021-8979. doi: 10.1063/1.3257167.
- [53] Jakub Drs. Four-sector microelectrode array for dielectrophoresis (in Czech). Bachelor’s thesis, Czech Technical University in Prague, Prague, Czech Republic, 2012.
- [54] Tomáš Michálek. Matrix electrode array for dielectrophoresis—basic position control (in Czech). Bachelor’s thesis, Czech Technical University in Prague, Prague, Czech Republic, 2013.
- [55] Jakub Tomášek. Optically controlled and sensed micromanipulation—basic setup. Bachelor’s thesis, Czech Technical University in Prague, Prague, Czech Republic, 2013.
- [56] Jiří Zemánek. Noncontact parallel manipulation with micro- and mesoscale objects using dielectrophoresis. Master’s thesis, Czech Technical University in Prague, Prague, Czech Republic, 2009.

-
- [57] Tomáš Michálek. Real-time optimization-based control for dielectrophoresis. Master's thesis, Czech Technical University in Prague, Prague, Czech Republic, 2015.
- [58] Jakub Drs. Micromanipulation platform for droplets (in Czech). Master's thesis, Czech Technical University in Prague, Prague, Czech Republic, 2015.
- [59] Martin Gurtner. Real-time optimization-based control and estimation for dielectrophoretic micromanipulation. Master's thesis, Czech Technical University in Prague, Prague, Czech Republic, 2016.
- [60] Jiří Zemánek. *Distributed manipulation by controlling force fields through arrays of actuators*. PhD thesis, Czech Technical University in Prague, Prague, Czech Republic, 2018.
- [61] Martin Gurtner and Jiří Zemánek. Twin-beam real-time position estimation of micro-objects in 3D. *Measurement Science and Technology*, 27(12):127003, November 2016. ISSN 0957-0233. doi: 10.1088/0957-0233/27/12/127003.
- [62] J. Zemánek, J. Drs, and Z. Hurák. Dielectrophoretic actuation strategy for micromanipulation along complex trajectories. In *2014 IEEE/ASME International Conference on Advanced Intelligent Mechatronics (AIM)*, pages 19–25. IEEE, July 2014. doi: 10.1109/aim.2014.6878040.

A scanning electron micrograph (SEM) showing a parallel array of gold electrodes. The electrodes are represented by diagonal gold lines. Several spherical polystyrene micro-beads are positioned on the electrodes. One bead in the lower right is in sharp focus, showing its spherical shape and the underlying electrode structure. Other beads are visible in the background, some in focus and some blurred. The overall image has a golden-yellow color scheme.

Polystyrene micro-beads on a
parallel electrode array

CHAPTER 2

Dielectrophoretic model for a sphere

Mathematical models of dielectrophoresis play an important role in the design of experiments, analysis of results, and even operation of some devices. In this paper, we test the accuracy of existing models in both simulations and laboratory experiments. We test the accuracy of the most common model that involves a point-dipole approximation of the induced field, when the small-particle assumption is broken. In simulations, comparisons against a model based on the Maxwell stress tensor show that even the point-dipole approximation provides good results for a large particle close to the electrodes. In addition, we study a refinement of the model offered by multipole approximations (quadrupole, and octupole). We also show that the voltages on the electrodes influence the error of the model because they affect the positions of the field nulls and the nulls of the higher-order derivatives. Experiments with a parallel electrode array and a polystyrene microbead reveal that the models predict the force with an error that cannot be eliminated even with the most accurate model. Nonetheless, it is acceptable for some purposes such as a model-based control system design.

This chapter was published as:

Tomáš Michálek and Jiří Zemánek. Dipole and multipole models of dielectrophoresis for a non-negligible particle size: Simulations and experiments. *ELECTROPHORESIS*, 38(11):1419–1426, June 2017. ISSN 1522-2683. doi: 10.1002/elps.201600466 © 2017 WILEY-VCH Verlag GmbH & Co. KGaA, Weinheim

2.1 Introduction

Dielectrophoresis, used as a tool for tasks such as separation, transportation, and analysis, was first systematically studied in 1951 [2]. Since then, several mathematical models have appeared in the literature. The models differ, in principle, in two aspects: how the field is calculated and how the induced field is modeled. Type of the mathematical model determines its accuracy as well as time and memory complexity. Therefore, for a given application, one has to pick the most suitable mathematical model. For example, the processing time may be limited as in the case of model-based control systems, where the model has to be evaluated several times per second.

According to how a model calculates the electric field, we can classify methods as those based on the analytical solution [3–7], the numerical solution [8], [9], and hybrid methods[10], which lay somewhere in between. Analytical methods, reported in the literature, usually work only for specific boundary conditions (B.C.s). Such models calculate the force very quickly, but they do not allow for a change of the electrodes' voltages. A numerical method can find the force for arbitrary voltages, but it is more demanding on memory and processing time. In section 2.2.3, we present a hybrid model that keeps advantages of the numerical simulation but is significantly faster. Methods can also differ in the kind of the boundary conditions used—these can be either exact or approximate (for example, linearly varying).

The simulation methods also differ in how they represent the induced electric field. The most common way involves dipolar approximation, which supposes the particle to be smaller than the size of inhomogeneity of the electric field. This approximation can be improved using so-called multipoles (such as quadrupoles and octupoles) corresponding to higher order terms in a Taylor series. Multipoles require higher order derivatives of the electric field. The most accurate—yet computationally very demanding—method is considered to be the *Maxwell Stress Tensor* (MST). It is based on the integration of the Maxwell stress tensor over the surface of the particle. The use of a *finite element method* (FEM) in 3D is necessary in this case.

Methods based on an approximation of the induced field use the electric field without taking into account presence of the particle. Calculation based on MST requires an electric field where the particle is present. This means that the electric field has to be calculated again if the particle moves, which

makes the method very computationally demanding.

Some comparison studies demonstrate the importance of higher-order multipolar contributions. Dalir et al. show in a set of simulations [11] how quadrupolar contribution becomes more significant as the particle approaches an array of parallel electrodes or as it grows in size. The insufficiency of the dipolar model—especially near the electrodes—is also reported by Benselama et al. [12], where a comparison between the MST and the dipolar model is made for a tip-plane electrode geometry. Kua et al. also investigate the influence of multipolar effects [6], in this case for a particular electrode design for a so-called moving DEP. A study by Rosales and Lim [13], which uses MST as a reference solution, deals with an analysis of widely used DEP cages. The authors declare that care must be taken when the particle is near the high field inhomogeneity, or near *field null* (a place with zero electric intensity), or when it is relatively large compared to the electrodes.

We examine the performance of a basic dipolar model and its multipolar extensions (quadrupolar and octupolar) especially when the assumptions for the approximation are not met. We also study the influence of the applied voltage on the error of the models related to the existence of the field nulls. We show that also the places where the gradients of the electric field or its higher-order derivatives vanish are prone to the presence of a significant relative error when using lower-order approximations.

Our study is based both on simulations and on experiments (experimental verifications of the mathematical models of DEP are rather rare in the literature). Three approximate mathematical models are first compared against the MST model, which we consider as a reference method. All of these models are well documented in the literature; we focus merely on their comparison. A computationally efficient implementation of the mentioned approximate models is described, but we do not present any new method overcoming the existing ones in accuracy. Simulations allow us to focus on the difference between the mathematical models, because they share the same material properties, geometry, etc. In the experiments, on the other hand, there is always some uncertainty regarding material properties, the influence of non-modeled phenomena, etc.

Our motivation comes from our previous work [14] where we realized that, although not all of the assumptions of a point-dipole model are satisfied, the model-based control algorithm performed surprisingly well in the experiments. Although this initial motivation is strongly related to our

particular application, we believe that this thorough analysis, made for one of the most utilized designs of electrodes, is rather general and can be of interest and use in the DEP community.

2.2 Materials and methods

2.2.1 Comparison setup

All the comparisons and experiments in this paper involve a parallel electrode array and a spherical particle. A schematic view of our setup is in Fig. 2.1; eight parallel ITO bars form an electrode array on a glass substrate. The width of one electrode is $100\ \mu\text{m}$ and the gap in between them has the same width. A polystyrene microbead immersed in a deionized water above the electrodes serves as the manipulated particle.

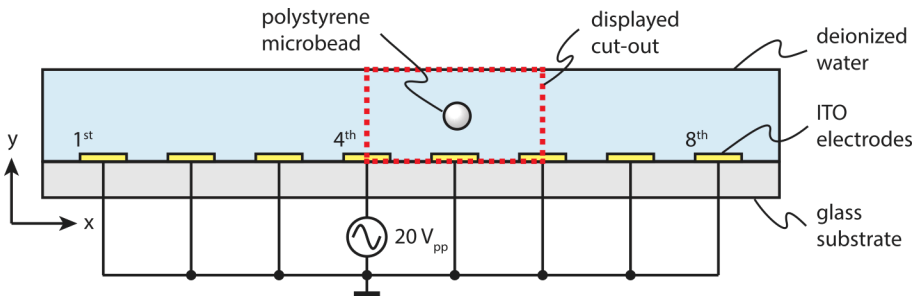


Figure 2.1: A scheme of the experimental setup used for comparisons of the approximate mathematical models of DEP to the MST model and the experimental measurements.

2.2.2 MST reference simulation

An overview of the MST method and its relation to the multipolar models is described, for instance, in [15]. For the implementation, we used Comsol (version 4.3)—a finite element method (FEM) solver, which can also calculate DEP force using the MST method. Unlike the approximate multipolar methods, the MST requires the electric field to be computed with the particle present in the field. We modeled the particle as a sphere, which makes the scene heterogeneous in all the three spatial dimensions. Thus a full 3D simulation is necessary. This significantly raises the computational and

memory demands, since these are related to the number of mesh elements used. A trade-off between the size of the simulated area (the greater, the better) and the size of the mesh elements (the smaller, the better), both influencing the solution accuracy, has to be made. The former helps to avoid edge effects, the latter increases the resolution of the result. We overcame this issue using so-called *Infinite Element Domains*, which simulate the unbounded regions at the domain boundaries. This way, the simulated area can be smaller allowing a finer mesh to be created. *Electric currents study* with the *Force Calculation* node then computes the DEP force based on the MST theory.

2.2.3 Point-dipole and multipole simulations

The derivation of the multipolar approximations of the DEP force is described, for example, in [15, 16]. From [15] we use an expression (49) for the time-averaged multipolar DEP force contribution. Since we consider only real-valued potentials to be applied to the electrodes, we can reduce the formula to the following form

$$\left\langle \mathbf{F}_{\text{gDEP}}^{(l)} \right\rangle = \frac{2\pi \text{Re}(\epsilon_m^*) r^{2l+1}}{l!(2l-1)!!} \text{Re} \left(f_{\text{CM}}^{(l)} \right) \quad (2.1)$$

$$(E_{a,i_1,i_2,\dots,i_{l-1}} \nabla E_{a,i_1,i_2,\dots,i_{l-1}}), \quad l = 1, 2, 3,$$

where l denotes the order of a contribution ($l=1$ for dipolar, $l = 2$ for quadrupolar, and $l = 3$ for octupolar contributions). The Einstein summation notation is used in the last bracket of Eq. (2.1), where E_a , $a \in \{x, y\}$ stands for a component of the electric field intensity evaluated at the position of the particle's center. Note that it is sufficient to take into account just two spatial components of the electric field for the force computation. Because the electric field along the third axis is constant (due to the electrode's geometry), no DEP force is induced in that direction. ∇ is the gradient operator. The subscripts i_1, i_2, \dots, i_{l-1} take on values from a set $\{x, y\}$ and denote along which direction the given quantity is differentiated. For example, the entry $E_{x,x,y,x}$ is an abbreviation for $\frac{\partial^3 E_x}{\partial^2 x \partial y}$. r is the particle radius and $f_{\text{CM}}^{(l)}$ denotes the so-called Clausius-Mossotti factor, which is given by

$$f_{\text{CM}}^{(l)} = \frac{l(\epsilon_p^* - \epsilon_m^*)}{l\epsilon_p^* + (l+1)\epsilon_m^*}, \quad (2.2)$$

where ϵ_m^* , ϵ_p^* are complex permittivities of the medium and the particle, respectively. These are computed as $\epsilon^* = \epsilon + \sigma/j\omega$ with ϵ being a permittivity of the given material and σ being its conductivity. $\omega = 2\pi f$ is an angular frequency of the harmonic electric field of frequency f , and $j = \sqrt{-1}$ is an imaginary unit.

As noted above, Eq. (2.1) gives just the multipolar contributions. The whole model is constructed as their sum

$$\langle \mathbf{F}_{\text{gDEP}} \rangle = \sum_{l=1}^N \langle \mathbf{F}_{\text{gDEP}}^{(l)} \rangle \quad (2.3)$$

where for $N = 1$ we get the dipolar, for $N = 2$ the quadrupolar, and for $N = 3$ the octupolar model. In this process, the most demanding step is the evaluation of the electric field and its higher-order derivatives for the point in space where the particle resides. A convenient and accurate way of getting these (in cases where no analytical solution exists) is again to involve the numerical FEM solver. Since the principle of superposition holds for both the electric potential and its derivatives (and thus also for the electric field and its derivatives), we can speed up the computations by forming a solution basis. We apply a potential of 1 V successively on all the eight electrodes, while the rest are kept at 0 V, and let the Comsol compute the electric field by solving Laplace's equation. From these eight elements, we can construct an electric field generated by arbitrary potentials applied to the electrodes in the following way

$$\begin{aligned} E_x(x, y) &= \sum_{i=1}^8 u_i E_{x,i}(x, y) = \mathbf{u}^T \mathbf{E}_x(x, y), \\ E_y(x, y) &= \sum_{i=1}^8 u_i E_{y,i}(x, y) = \mathbf{u}^T \mathbf{E}_y(x, y), \end{aligned} \quad (2.4)$$

where u_i corresponds to the unitless voltage magnitude on the i th electrode and $E_{x,i}(x, y)$ respectively $E_{y,i}(x, y)$ is an electric intensity corresponding to a unit voltage on the i th electrode (our solution basis), which can be arranged in a vector form \mathbf{E}_x , respectively \mathbf{E}_y . The same applies to all the different spatial electric field derivatives. Then the expression Eq. (2.3) can be transformed to the following matrix form, where the source voltages appear explicitly

$$F_b = \mathbf{u}^T \mathbf{P}_b(x, y) \mathbf{u}, \quad b \in \{x, y\}, \quad (2.5)$$

where

$$\mathbf{P}_b(x, y) = \sum_{l=1}^N \frac{2\pi \text{Re}(\epsilon_m^*) r^{2l+1}}{l!(2l-1)!!} \text{Re} \left(f_{\text{CM}}^{(l)} \right) \times \left(\mathbf{E}_{a, i_1, i_2, \dots, i_{l-1}}(x, y) \mathbf{E}_{a, b, i_1, i_2, \dots, i_{l-1}}^{\text{T}}(x, y) \right). \quad (2.6)$$

The derivation can be readily extended to include the 3rd dimension if needed (for non-symmetric electrode array). Note that the matrix $\mathbf{P}_b(x, y)$ does not depend on voltages; therefore it can be calculated only once for a given electrode array and used to calculate force for various voltages.

2.2.4 Validation of model implementation

We have compared the solutions obtained by our implementation of the dipolar model with the results of analytical models described in the literature. Namely, we used the solutions for a standing wave boundary potential generated by both approximate and exact B.C.s, as derived in [5], and another solution by approximate B.C. taken from [7]. Since both of these papers assume an infinite number of electrodes—which is infeasible in our approach—we had to include as many of them as possible to have comparable results. Despite this issue, the models match each other sufficiently well (relative errors in the order of thousandths of a percent for approximate B.C.s and the order of several percents for exact B.C.s), especially in the lower levitation height region, where the influence of distant electrodes is negligible.

Furthermore, we have also checked for numerical errors and boundary effects, which can always emerge in FEM simulation. Apart from the usual mesh refinement and simulation area extension performed to see if the result converges, we also compared our solution with the analytical one obtained by Green's function [17]. The numerically computed exact B.C. was approximated by a large sum of trapezoidal B.C.s. For every one of these B.C.s, an analytical solution of potential exists and by summing them we converge to a potential caused by the original exact B.C. Although this computation is still based on a numerically obtained B.C., the resulting electric field and especially its higher-order derivatives should at least not suffer from numerical differentiation issues reported in [6]. The correspondence of the two results implies that there are no such problems in our case.

2.3 Results and discussion

2.3.1 Comparison of models

We did a comparison with the MST solution for the following set of potentials on the electrodes—all the electrodes were grounded except the 4th one to which a sinusoidal signal of 10 V was applied. Other parameters used in the simulations are: $f = 300$ kHz, $r = 25$ μm , $\epsilon_m = 80$, $\sigma_m = 5.49$ $\mu\text{S m}^{-1}$, $\epsilon_p = 2.5$ and $\sigma_p = 0.27$ mS m^{-1} . Figure 2.1 shows a schematic of this comparison setting. If not stated otherwise, all models used exact B.C. The DEP force was computed in a grid of points corresponding to the different horizontal as well as vertical positions of the particle. Obtained results are compared in a series of graphs capturing a cut-out represented in Fig. 2.1 by a dashed rectangle. Particularly, a magnitude of error of the approximate models with respect to the reference model is compared. For brevity, we will use just the term error throughout the whole subsequent discussion.

Figure 2.2A, 2.2B, 2.2C, and 2.2D show the relative and absolute errors of the individual multipolar models for both the magnitude and the direction of the DEP force. The origin of the coordinates lies in the electrode plane in the middle of the array (between the 4th and the 5th electrode). Black bars on the x -axis indicate the location of the electrodes; the leftmost visible has the potential of 10 V according to the previous description.

For the moment, we will ignore the biggest peak (located at around $x = 225$ μm and $y = 61$ μm) appearing at majority of the referred graphs, which we will comment on later. It can be seen that otherwise, for the dipolar approximation, the errors in magnitude (Fig. 2.2A and 2.2C) are the most significant near the edges of the 4th electrode (because of the presence of the highest field inhomogeneities). The error is much greater for the dipolar approximation than for the quadrupolar or the octupolar models. The same holds for the errors in the force direction shown in Fig. 2.2B and 2.2D, but these are smaller. Although the dipolar predictions are in general worse than predictions of the higher-order models, they are surprisingly better at some locations.

Now we will comment on the (previously skipped) most significant peak in the referred graphs. In Fig. 2.3A a similar peak can be seen when comparing the relative error of the dipolar model against the octupolar one. Note that if we replace the exact B.C. by an approximate B.C. (potential varies linearly in between each pair of neighboring electrodes), such error

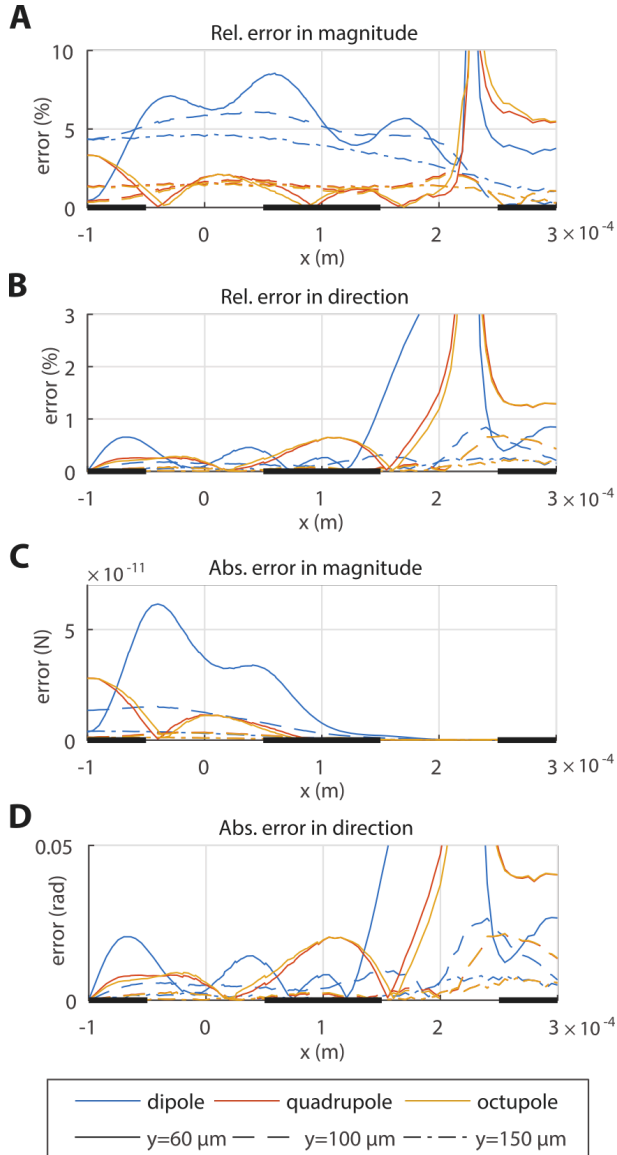


Figure 2.2: A, B, C, D) The relative and absolute errors of the dipolar, the quadrupolar, and the octupolar model (compared to MST model) for the magnitude and direction of the DEP force as they change with the position of the microbead.

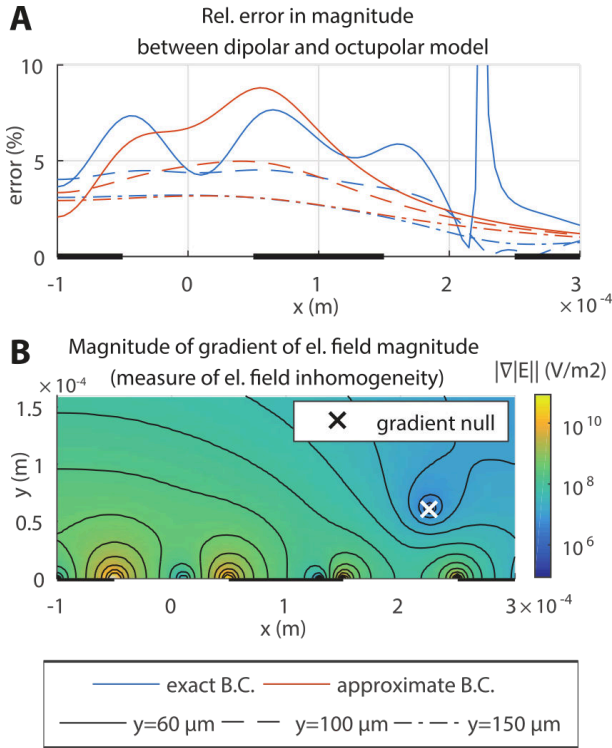
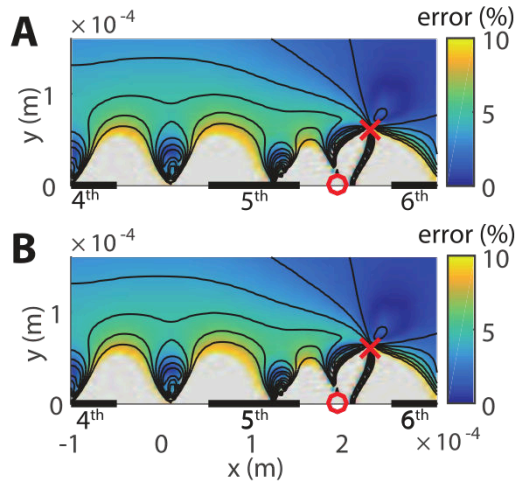


Figure 2.3: A) The relative error between the dipolar and the octupolar model for exact and approximate B.C. as they change with the position of the microbead. B) Magnitude of the electric field gradient.

disappears. It is therefore related to the electric field. Specifically, the peak location corresponds to a point where the magnitude of an electric intensity gradient vanishes (see Fig. 2.3B), which is further referred to as a “gradient null”. In contrast to the field null, in the case of the gradient null not only the dipolar contribution to the force vanishes but also the quadrupolar one is zero (see Eq. (2.1)). The DEP force is thus determined solely by contributions of order even higher than quadrupolar. As a consequence, all models of lower order than octupolar will always have large relative errors at such places. Finally, note from Fig. 2.2D that also the absolute error of the direction is significant at the null point. This is natural since the direction of zero force vector is not well defined. This discussion could also be generalized to the zero points of $\nabla^2\mathbf{E}$, $\nabla^3\mathbf{E}$ and nulls of higher-order

field derivatives.

Relative errors when scaling potentials on electrodes



Absolute errors when scaling potentials on electrodes

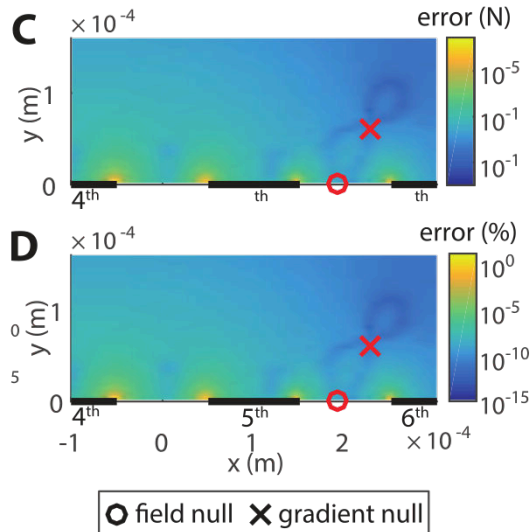


Figure 2.4: The relative and B, D) the absolute errors of the dipolar model w.r.t. the octupolar model and their change as we scale the applied voltage. In A, B) a 10 V potential, whereas in C, D) a 100 V potential was applied on the 4th electrode, while the rest of them were grounded.

When we just scale the voltage amplitudes, the relative errors remain unchanged, while the absolute errors increase or decrease appropriately. Thus, although the absolute errors emerging in gradient null locations are smaller than those present in the field null locations, they can be still arbitrarily large depending on the applied voltage. We present this using a comparison of the dipolar and the octupolar model shown in Fig. 2.4. Note, that when the gradient null is located near the field null, there is a tendency for an error originated in the field null to spread towards the gradient null location. We can observe this in Fig. 2.4A, 2.4B as a high error region extends from the center between the 5th and 6th electrode (field null location) towards the gradient null point.

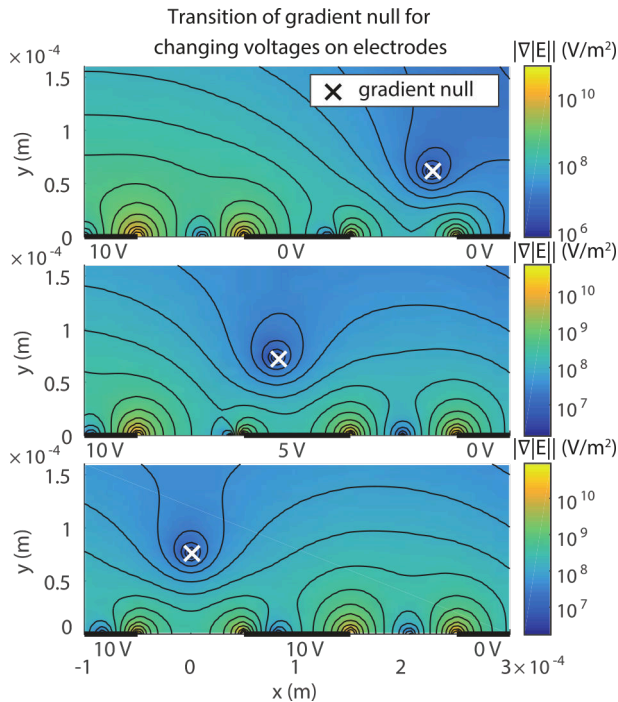


Figure 2.5: Location of a null of the electric field gradient for several different potentials applied to the electrodes.

The gradient null typically forms in between the electrodes of the same or a similar potential. By changing the mutual potential difference, the null points translate in a horizontal direction gradually from the inter-electrode

gap over the electrode to the neighboring gap. Figure 2.5 shows such behavior for a case when 10 V was applied to the 4th electrode and we gradually increased the voltage on the 5th electrode so that in the end both electrodes had the same potential. By suitable potential settings, the null point can be moved even to different levitation heights.

Finally, we also explored how the error evolves with a change in the size of the particle. Figure 2.6 shows the relative errors of the dipolar model against the MST solution for particles with a diameter of 5 μm , 40 μm and 75 μm . Apparently, the relative error grows with the size of a particle as well as with the vicinity of the electrode edges. For the 75 μm particle located at the levitation height of 90 μm the error is only 12 %.

2.3.2 Comparison with experiments

The accuracy of the various models can also be shown by comparing their predictions against the experimental results. Due to our previous work, we can control the movement of the particle and, using a measurement system [18], we are also able to track the position of the particle in 3D.

From measured position data we obtain the velocity of the particle by differentiation. We can plug the velocity into Stokes' law and solve for the force acting on the particle. To get the DEP force, we have to compensate for the sedimentation force. We get

$$\begin{aligned}
 F_{\text{DEP},x} &= 6\pi\mu r \lambda_x \frac{dx(t)}{dt}, \\
 F_{\text{DEP},y} &= 6\pi\mu r \lambda_y \frac{dy(t)}{dt} - \frac{4}{3}\pi r^3 (\rho_m - \rho_p) g,
 \end{aligned}
 \tag{2.7}$$

where $x(t)$ and $y(t)$ give the measured position of the particle as a function of time, μ is the dynamic viscosity of the medium and ρ_m and ρ_p are densities of the medium and the particle respectively. The electrode array can cause a wall effect on a particle moving in the vicinity of the surface, which leads to increased drag. We compensated the wall effect through corrections to Stokes' law λ_x and λ_y [19] [Eq. 7-4.28 and 7-4.38].

Plots of these forces together with the predictions of the dipolar, the octupolar approximations, and partially the MST models are shown in Fig. 2.7A and 2.8A for two experiments. In the first, the particle followed a trajectory plotted in Fig. 2.7C resulting from manual control by a human operator. In the second experiment a control system followed a

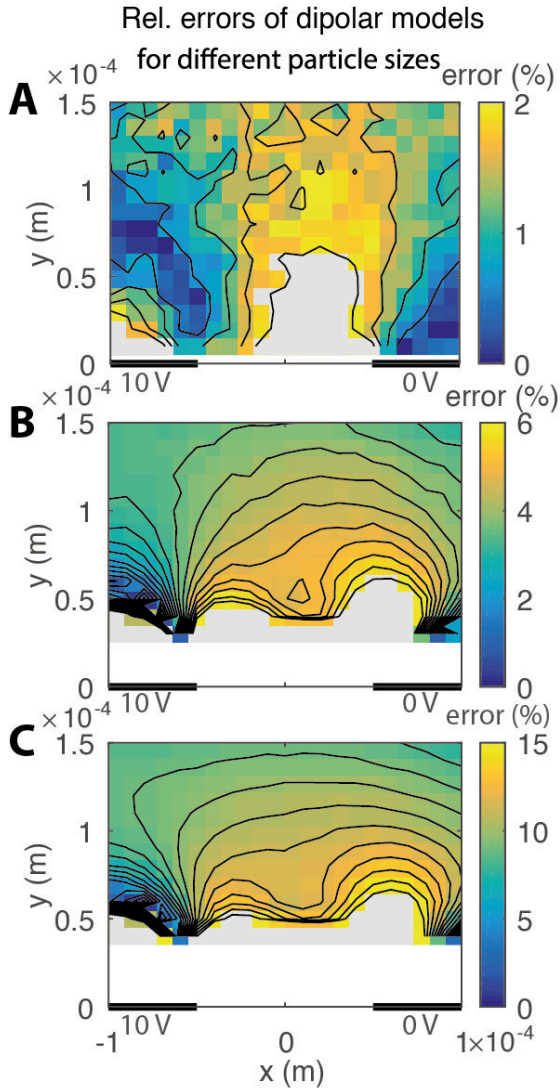


Figure 2.6: Influence of the particle size on the error of the dipolar approximation (compared to MST model). Diameters of the particles are A) $5\ \mu\text{m}$, B) $40\ \mu\text{m}$, and C) $75\ \mu\text{m}$.

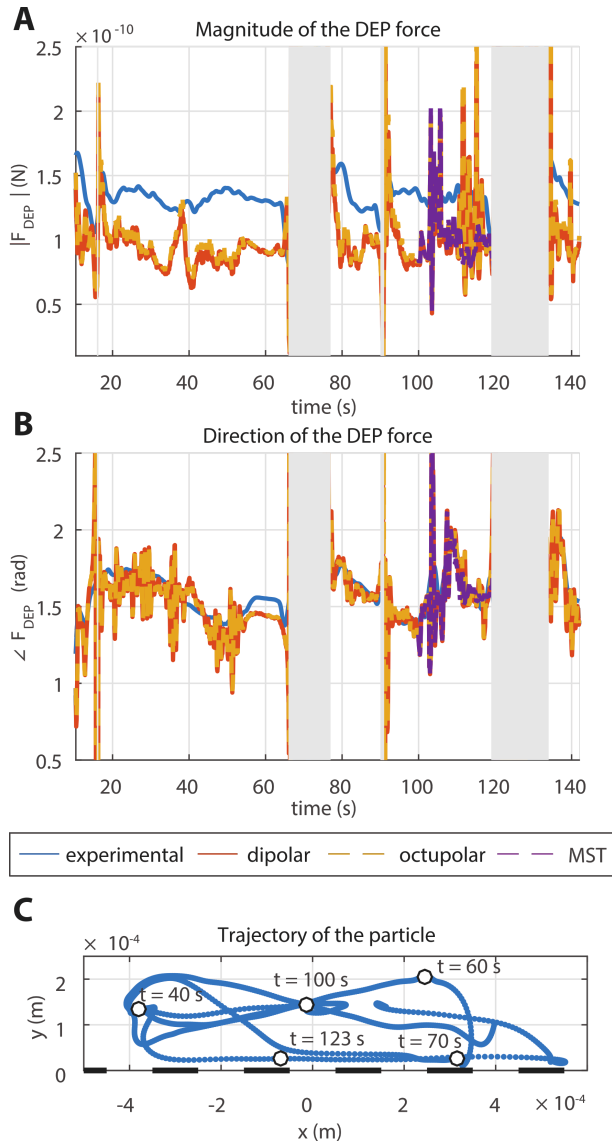


Figure 2.7: Comparisons of the model predictions against the experimental measurement. Shown are an absolute error in A) magnitude and B) direction of the DEP force and C) the overall bead trajectory.

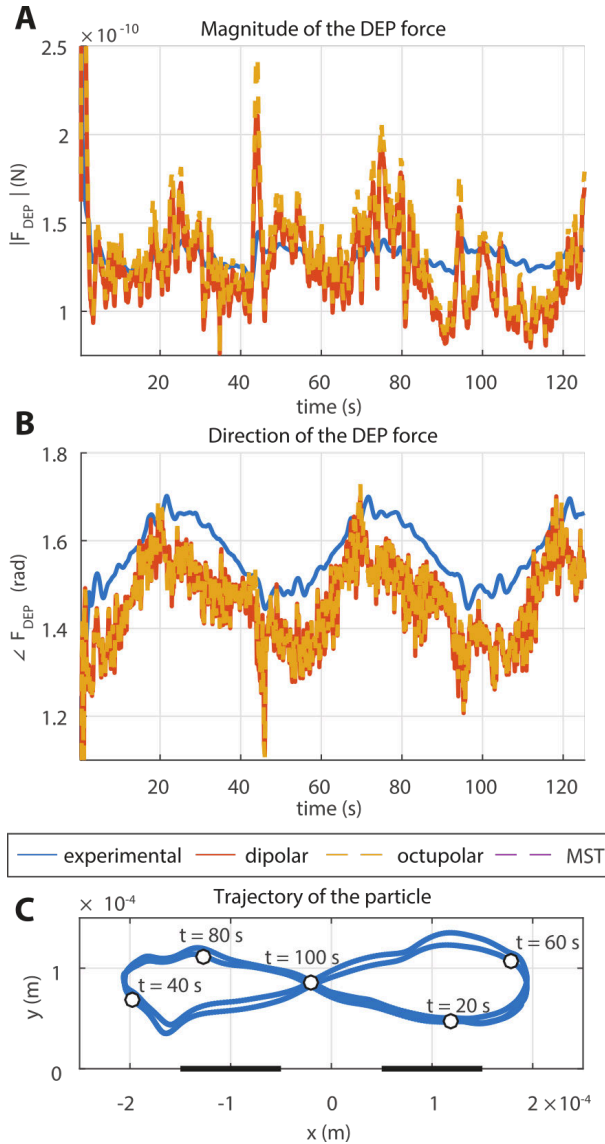


Figure 2.8: Comparisons of the model predictions against the experimental measurement. Shown are an absolute error in A) magnitude and B) direction of the DEP force and C) the overall bead trajectory.

figure-eight curve shown in Fig. 2.8C. All of these models were evaluated for the measured position of the particle and while the potentials from the experiment were applied to the electrodes. The material parameters entering the model were either known (found in the literature) or obtained by system identification techniques as follows: $f = 300$ kHz, $r = 25$ μm , $\epsilon_m = 78.4$, $\sigma_m = 5.49$ $\mu\text{S m}^{-1}$, $\epsilon_p = 2.5$, $\sigma_p = 2$ $\mu\text{S m}^{-1}$, $\rho_m = 997.1$ kg m^{-3} , $\rho_p = 1.2 \times 10^3$ kg m^{-3} and $\mu = 0.89$ $\mu\text{N s m}^{-2}$. The shaded areas correspond to the time intervals where the particle interacted directly with the bottom surface of the manipulation area. Since this is not encountered in either of our simplified models, we removed it from our comparison.

Although the differences between the simulations and the experimental measurements are evident, they are not caused by a low order approximation of the DEP. This is apparent, for instance, in Fig. 2.7A, where even the MST underestimates the resulting DEP force in the same way that multipolar models do. In the first experiment, the mean value of the relative error is 42.2% in the magnitude and 7.8% in the direction. For the second experiment, the average value of the relative error is 13.5% in the magnitude and 3.6% in the direction. A video demonstrating an agreement of the dipolar model with experiments is available as ‘‘Supporting Information’’.

2.3.3 Analysis of computational and memory requirements

As mentioned above, the models also differ in computational time and memory required for their evaluation. These are greater for more accurate models. In Table 2.1, we show specific values measured for our particular implementations. A conventional PC (Intel Core i5, 3.30 GHz, 8 GB RAM, 64-bit, Win 7) was used to evaluate the models.

Table 2.1: Time and memory requirements for evaluation of different models.

Method	MST	Dipole	Quadrupole	Octupole
Time*	20 min	0.42 ms (+5.9 h once)**	0.88 ms (+11 h once)**	1.8 ms (+16.7 h once)**
Memory	5 GB	130 MB	240 MB	370 MB

* Average solution time for one point

** Time needed for computation of the solution basis. Performed only once for each electrode array.

2.4 Concluding remarks

We analyzed the behavior of the three existing approximate mathematical models of DEP (dipolar, quadrupolar, and octupolar) in the case where the particle is of comparable size to the electrodes (which is directly related to inhomogeneity of the field). The model based on Maxwell stress tensor (MST) provided the reference value of the force. All the simulations and experiments considered a spherical particle above a parallel electrode array.

As expected, the simulations revealed that the largest error of the dipolar model appears at places of high field inhomogeneity, typically close to the electrodes. Nevertheless, the relative error for a $75\ \mu\text{m}$ sphere located $90\ \mu\text{m}$ above the electrodes is 12%, and only 5% for a $50\ \mu\text{m}$ sphere. While the improvement caused by including the quadrupolar contribution was significant (it halved the error), the octupolar model yielded almost no further improvement over the quadrupolar one.

Furthermore, we showed that not only the so-called field nulls but also the nulls in higher-order derivatives are places where the relative error is significant (approaches 100%). Nevertheless, the absolute error is not critical—its significance decreases with the order of the null. These null points do not arise only as a consequence of the carefully designed DEP traps, they appear quite commonly. Moreover, some higher-order null points depend on the boundary conditions—they disappear for approximate boundary conditions. This improves the agreement between the dipolar and the octupolar model, but introduces greater error compared to the MST. Furthermore, the null points move when the voltage on the electrodes changes.

We also investigated the accuracy of the mathematical models experimentally. A control system steered and followed a polystyrene sphere above the parallel electrode array. DEP force was then derived using the Stokes' law. The errors in the force magnitude for the two experiments were 42.2% and 13.5%, respectively. For the direction, these were 7.8% and 3.6%, respectively. All tested models performed similarly, even the model based on MST, which shows that the source of the error lies in some non-modelled phenomena, rather than in the models themselves.

In conclusion, mathematical models based on the approximation of the induced field proved to be sufficiently accurate for some applications. For instance, when the processing time has to be kept short, as in the case of a model-based control system. Force calculation took from 0.42 ms (for the dipolar model) to 1.8 ms (for the octupolar model). In contrast, the

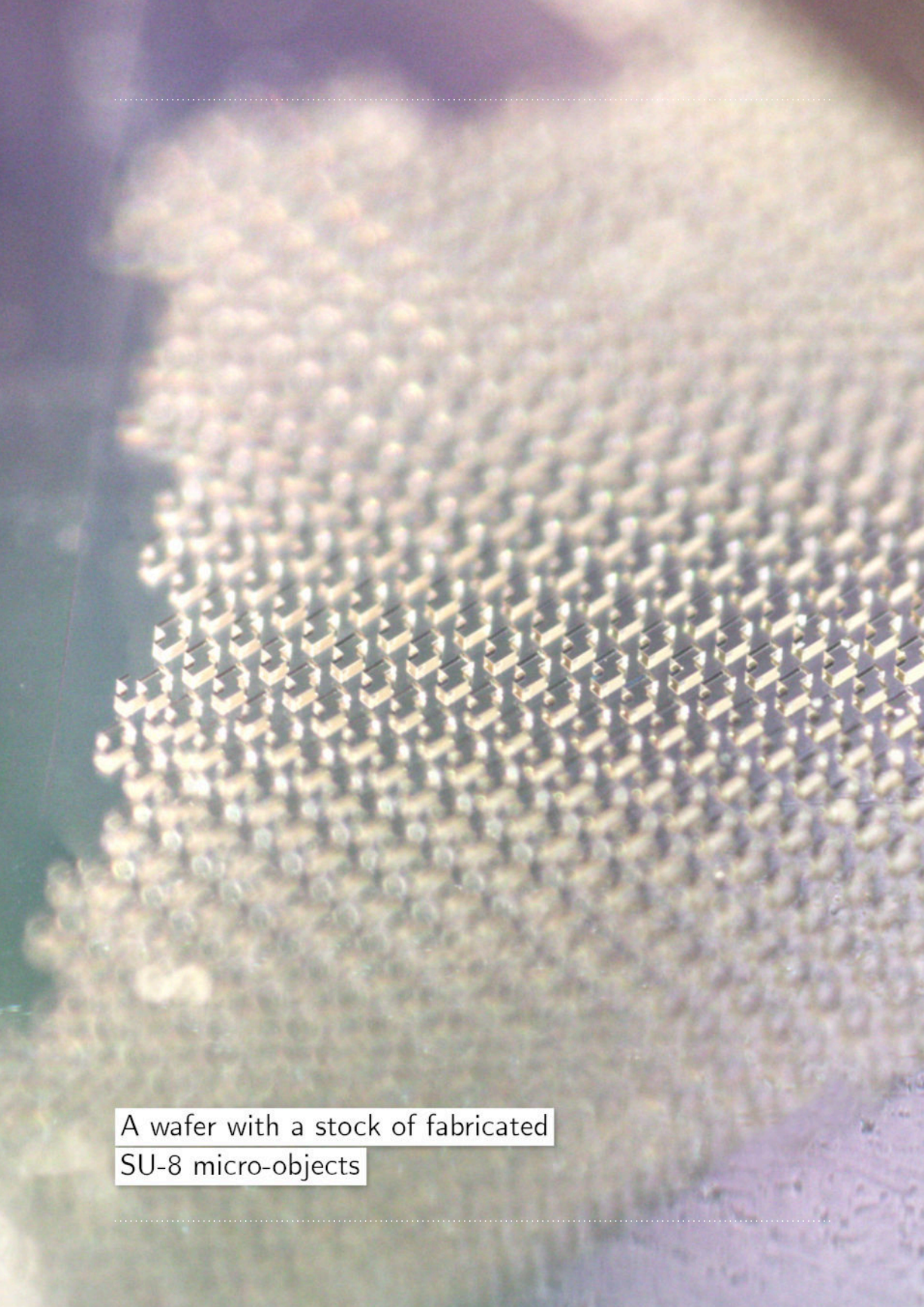
computation of the MST model for the same situation takes 20 min and does not add any significant improvement.

2.5 Bibliography

- [1] Tomáš Michálek and Jiří Zemánek. Dipole and multipole models of dielectrophoresis for a non-negligible particle size: Simulations and experiments. *ELECTROPHORESIS*, 38(11):1419–1426, June 2017. ISSN 1522-2683. doi: 10.1002/elps.201600466.
- [2] Herbert A. Pohl. The Motion and Precipitation of Suspensoids in Divergent Electric Fields. *Journal of Applied Physics*, 22(7):869–871, July 1951. ISSN 0021-8979. doi: 10.1063/1.1700065.
- [3] Tao Sun, Hywel Morgan, and Nicolas G. Green. Analytical solutions of ac electrokinetics in interdigitated electrode arrays: Electric field, dielectrophoretic and traveling-wave dielectrophoretic forces. *Physical Review E*, 76(4):046610, October 2007. doi: 10.1103/PhysRevE.76.046610.
- [4] Xujing Wang, Xiao-Bo Wang, F. F. Becker, and Peter R. C. Gascoyne. A theoretical method of electrical field analysis for dielectrophoretic electrode arrays using Green’s theorem. *Journal of Physics D: Applied Physics*, 29(6):1649–1660, June 1996. ISSN 0022-3727. doi: 10.1088/0022-3727/29/6/035.
- [5] Dong Eui Chang, Sophie Loire, and Igor Mezić. Closed-form solutions in the electrical field analysis for dielectrophoretic and travelling wave inter-digitated electrode arrays. *Journal of Physics D: Applied Physics*, 36(23):3073–3078, December 2003. ISSN 0022-3727, 1361-6463. doi: 10.1088/0022-3727/36/23/032.
- [6] Chin Hock Kua, Yee Cheong Lam, Chun Yang, Kamal Youcef-Toumi, and Isabel Rodriguez. Modeling of dielectrophoretic force for moving dielectrophoresis electrodes. *Journal of Electrostatics*, 66(9):514–525, September 2008. ISSN 0304-3886. doi: 10.1016/j.elstat.2008.05.001.
- [7] Hywel Morgan, Alberto García Izquierdo, David Bakewell, Nicolas G. Green, and Antonio Ramos. The dielectrophoretic and travelling wave

- forces generated by interdigitated electrode arrays: analytical solution using Fourier series. *Journal of Physics D: Applied Physics*, 34(10):1553–1561, May 2001. ISSN 0022-3727. doi: 10.1088/0022-3727/34/10/316.
- [8] D. F. Chen, H. Du, W. H. Li, and C. Shu. Numerical modeling of dielectrophoresis using a meshless approach. *Journal of Micromechanics and Microengineering*, 15(5):1040–1048, April 2005. ISSN 0960-1317. doi: 10.1088/0960-1317/15/5/021.
- [9] N. G. Green, A. Ramos, and H. Morgan. Numerical solution of the dielectrophoretic and travelling wave forces for interdigitated electrode arrays using the finite element method. *Journal of Electrostatics*, 56(2):235–254, September 2002. ISSN 0304-3886. doi: 10.1016/S0304-3886(02)00069-4.
- [10] Mohamed Kharboutly, Michaël Gauthier, and Nicolas Chaillet. Modeling the trajectory of a microparticle in a dielectrophoresis device. *Journal of Applied Physics*, 106(11):114312, December 2009. ISSN 0021-8979. doi: 10.1063/1.3257167.
- [11] Dalir Hamid, Yanagida Yasuko, and Hatsuzawa Takeshi. Quadrupolar analysis of an interdigitated micro-electrode array for dielectrophoretic particle transport. In *Proceedings of JSPE Semestrial Meeting 2008 JSPE Autumn Conference*, volume 2008A, pages 547–548. The Japan Society for Precision Engineering, 2008. doi: 10.11522/pscjspe.2008A.0.547.0.
- [12] AM Benselama, P Pham, and E Canot. Modeling of the dielectrophoretic forces acting upon biological cells: A numerical comparison between finite element/boundary element maxwell stress tensor methods and point–dipole approach. In *Technical Proceedings of the NSTI Nanotechnology Conference and Trade Show 2004*, volume 1, pages 7–11, 2004. ISBN 0-9728422-7-6.
- [13] Carlos Rosales and Kian Meng Lim. Numerical comparison between Maxwell stress method and equivalent multipole approach for calculation of the dielectrophoretic force in single-cell traps. *ELECTROPHORESIS*, 26(11):2057–2065, June 2005. ISSN 1522-2683. doi: 10.1002/elps.200410298.

-
- [14] Jiří Zemánek, Tomáš Michálek, and Zdeněk Hurák. Feedback control for noise-aided parallel micromanipulation of several particles using dielectrophoresis. *ELECTROPHORESIS*, 36(13):1451–1458, July 2015. ISSN 1522-2683. doi: 10.1002/elps.201400521.
- [15] Xujing Wang, Xiao-Bo Wang, and Peter R. C. Gascoyne. General expressions for dielectrophoretic force and electrorotational torque derived using the Maxwell stress tensor method. *Journal of Electrostatics*, 39(4):277–295, August 1997. ISSN 0304-3886. doi: 10.1016/S0304-3886(97)00126-5.
- [16] T.B. Jones. Basic theory of dielectrophoresis and electrorotation. *IEEE Engineering in Medicine and Biology Magazine*, 22(6):33–42, November 2003. ISSN 1937-4186. doi: 10.1109/MEMB.2003.1304999.
- [17] Martin Gurtner, Kristian Hengster-Movric, and Zdeněk Hurák. Green’s function-based control-oriented modeling of electric field for dielectrophoresis. *Journal of Applied Physics*, 122(5):054903, August 2017. ISSN 0021-8979. doi: 10.1063/1.4997725.
- [18] Martin Gurtner and Jiří Zemánek. Twin-beam real-time position estimation of micro-objects in 3D. *Measurement Science and Technology*, 27(12):127003, November 2016. ISSN 0957-0233. doi: 10.1088/0957-0233/27/12/127003.
- [19] John Happel and Howard Brenner. *Low Reynolds number hydrodynamics: with special applications to particulate media*. Prentice-Hall, 1965.

A high-magnification scanning electron micrograph (SEM) showing a dense array of small, rectangular, three-dimensional micro-objects. The objects are arranged in a regular, grid-like pattern on a substrate. The objects have a distinct 3D structure, appearing as small rectangular blocks with slightly rounded edges. The background is a smooth, light-colored surface, likely the wafer substrate. The overall appearance is that of a highly ordered micro-fabricated structure.

A wafer with a stock of fabricated
SU-8 micro-objects

CHAPTER 3

Dielectrophoretic model of arbitrarily-shaped object

The most popular modeling approach for dielectrophoresis (DEP) is the effective multipole (EM) method. It approximates the polarization induced charge distribution in an object of interest by a set of multipolar moments. The Coulombic interaction of these moments with the external polarizing electric field then gives the DEP force and torque acting on the object. The multipolar moments for objects placed in arbitrary harmonic electric fields are, however, known only for spherical objects. This shape restriction significantly limits the use of the EM method. We present an approach for online (in real time) computation of multipolar moments for objects of arbitrary shapes having even arbitrary internal composition (inhomogeneous objects, more different materials, etc.). We exploit orthonormality of spherical harmonics to extract the multipolar moments from a numerical simulation of the polarized object. This can be done in advance (offline) for a set of external electric fields forming a basis so that the superposition principle can then be used for online operation. DEP force and torque can thus be computed in fractions of a second, which is needed, for example, in model-based control applications. We validate the proposed model against reference numerical solutions obtained using Maxwell stress tensor. We also analyze the importance of the higher-order multipolar moments using a sample case of a Tetris-shaped micro-object placed inside a quadrupolar micro-electrode array and exposed to electrorotation. The implementation of the model in MATLAB and COMSOL is offered for free download.

Reprinted with permission from:

Tomáš Michálek, Aude Bolopion, Zdeněk Hurák, and Michaël Gauthier. Control-oriented model of dielectrophoresis and electrorotation for arbitrarily shaped objects. *Physical Review E*, 99(5):053307, May 2019. doi: 10.1103/PhysRevE.99.053307 © 2019 by the American Physical Society.

3.1 Introduction

Electrokinetic effects, when exploited at micro-scale, constitute a fundamental principle of numerous non-contact micro-manipulation devices. They use the electric field to impart forces and torques either directly on the objects of interest or indirectly on the liquid medium surrounding them, which then induces a fluid flow carrying the objects to the desired locations.

A widespread representative of the former is the *dielectrophoresis* (DEP). First described by Pohl [2], it is a physical phenomenon enabling actuation of electrically neutral objects. By placing them in an external electric field, they polarize, and the newly emerged charge distribution inside them interacts via Coulomb forces with the source field. In case of an inhomogeneous field, this results in a net force making the object to move. Alternating electric fields are commonly used to eliminate the (unwanted) phenomena of *electrolysis* and *electrophoresis* (interaction between the external field and an intrinsic charge potentially present inside the object). Two significant modes of dielectrophoresis are distinguished: *conventional DEP* (cDEP) and *traveling-wave DEP* (twDEP). The former arises from a spatially varying *magnitude* of the field while the latter is due to its spatially varying *phase*. The closely related concepts of *electro-orientation* and *electrorotation*, both causing a torque acting on the object, are usually treated separately in the literature. A shared name—*generalized DEP* (gDEP), coined in [3], can be used to jointly describe all the above mentioned polarization-related phenomena. The review of gDEP may be found, for example, in [4], where the authors consider not only the quasi-static but also arbitrary time-varying fields. The latter is denoted as the *transient gDEP* or the *polarization history* (or *crossing trajectory*) effect. However, since the period of the AC electric field is usually much higher than the time scale related to the object’s movement, the quasi-static theory and related mathematical models are typically sufficient. Other useful resources concerning DEP are for example [5–8].

A mathematical model of DEP enables us not only to perform various simulations and analyses helping us to understand the described physics, but it is also necessary when it comes to applying DEP to a precise position and orientation control of the micro-objects. In such cases, apart from the model accuracy, also its computational time becomes essential as it is detailed in [9], where we described a device for independent position control of several micro-spheres. Following this motivation, we aim at developing a

real-time evaluable model for DEP force and torque computation applicable not only to spherical but to arbitrarily-shaped objects.

State-of-the-art

There are two basic approaches for modeling DEP: *Maxwell stress tensor* (MST) method [10] and *effective moments* (EM) method [3, 11–14]. The former is considered as the most accurate one, but since it is based on finite element method (FEM) computations, it imposes huge time and memory requirements. The latter method is, on the other hand, just an approximation of the actual DEP force and torque, but it leads to analytical formulas for force and torque computations, and thus it is fast to evaluate. The key idea here is that the electric field of a polarized object is represented by a set of electric multipoles of an increasing order (the higher the order of the multipole, the higher the accuracy of the approximation) and the total DEP force and torque is then the sum of the forces and torques acting on these individual multipoles. The accuracy of the EM method under various scenarios and using various orders of approximation was investigated for example in [15–17] and in [18] by authors. Generally, the higher order multipolar moments are necessary for situations when the external polarizing electric field is highly inhomogeneous or when the object is of some complicated shaped. In practice, however, the use of this method is so far essentially limited to spherical objects only. That is because only for them a multipolar description for general harmonic electric fields can be obtained. Partial results exist for ellipsoidal objects [19, 20], for which analytical formulas for induced dipole are known, and also for any other cylindrically symmetrical objects [21, 22], for which multipolar moments up to the 9th order can be obtained from numerical simulations. In both of these cases, the symmetry requirement stems from the fact that only the linear multipoles (all the charges are constrained to a single line) are used for the description of the polarized object. Moreover, this also means that these methods are only valid if the external electric field is rotationally symmetric along the symmetry axis of the object.

Contribution

We propose a method for online (in real time) computation of multipolar moments describing the electric field of an arbitrarily-shaped polarized

object that does not pose any limitations regarding the shape, material properties or even inhomogeneity of the object. Its orientation in space or the external polarizing electric field itself can also be arbitrary. The obtained multipoles can then be used in the EM method, which significantly extends its practical applicability. The resulting real-time evaluable model can serve as a solid foundation for a future design of control algorithms achieving simultaneous DEP based position and orientation control of arbitrarily shaped micro-objects in fluidic media.

In this paper, we consider that the object of interest is located in a quiescent fluid sufficiently far from any other objects or obstacles. Modeling of the interaction between more non-spherical objects is a subject of future research, similarly as is the modeling of the hydrodynamic effects influencing the object's motion in a fluid.

3.2 Proposed modeling scheme

The proposed method extends the use of the EM method and deals with its essential elements—the multipolar moments, hence we will start by summarizing basic existing concepts.

3.2.1 Multipolar moments and EM method

In the EM method, multipolar moments (or multipoles) are used to describe a potential due to a charge distribution inside a polarized object. As will be shown below, such description is, however, only approximate.

3.2.1.1 Multipolar moments

Consider an arbitrary external electrostatic source field in an empty space described by an associated electric potential Φ_{empty} . If we place an electrically neutral (uncharged) object of interest into this field, the object polarizes and the potential field changes to Φ_{filled} . It holds that $\Phi_{\text{filled}} = \Phi_{\text{empty}} + \Phi_{\text{object}}$, where Φ_{object} is the potential corresponding to the newly emerged charge distribution inside the object due to its polarization. We will denote the mentioned charge distribution by $\rho(\mathbf{r})$. The object and thus also the whole charge distribution is, without the loss of generality, confined to an interior of a virtual sphere S of radius R located at the origin of the coordinate system. Outside this sphere the potential there can be written

as the volumetric integral

$$\Phi_{\text{object}}(\mathbf{r}) = \frac{1}{4\pi\epsilon_0\epsilon_m} \int_{S(R)} \frac{\rho(\mathbf{r}')}{|\mathbf{r} - \mathbf{r}'|} d^3r', \quad \mathbf{r} \geq R, \quad (3.1)$$

where ϵ_0 is the permittivity of a vacuum, ϵ_m is the relative permittivity of surrounding medium and \mathbf{r} is a vector representing a position in space. By expanding the term $\frac{1}{|\mathbf{r} - \mathbf{r}'|}$ in Eq. (3.1) in a Taylor series about the origin, we get an infinite sum describing the potential using multipolar moments. Depending on whether we perform the expansion in Cartesian or spherical coordinates, we get *Cartesian multipolar moments* or *spherical multipolar moments*, both of which will be, due to their unique properties, useful in the following development. For the Cartesian case, we get

$$\begin{aligned} \Phi_{\text{object}}(\mathbf{r}) &= \frac{1}{4\pi\epsilon_0\epsilon_m} \\ &\times \left(\frac{\mathbf{p}^{(0)}}{r} + \frac{\mathbf{p}^{(1)} \cdot \mathbf{r}}{r^3} + \frac{1}{2} \sum_{i,j=1}^3 \frac{r_i r_j}{r^5} p_{ij}^{(2)} + \dots \right), \quad (3.2) \\ &\mathbf{r} \geq R, \end{aligned}$$

where $r = \|\mathbf{r}\|_2$, r_i is the i th element of vector \mathbf{r} , $\mathbf{p}^{(n)}$ are the multipolar moments. For $n = 1$ we call the corresponding moment dipole, for $n = 2$ we call it quadrupole followed by octopole, hexadecapole and 2^n -poles for even higher values of n . These are tensor quantities of the corresponding order, and the subscripts of p then refer to the individual elements of these tensors. Notice that the higher the order of multipole, the faster the decay of the corresponding term to zero with the increasing distance r from the origin. Depending on the required accuracy of the electric potential representation, we can trim the series in the brackets and use just the first few terms.

Similarly, when we perform the Taylor series expansion in the case of spherical coordinates we get

$$\Phi_{\text{object}}(\mathbf{r}) = \frac{1}{\epsilon_0\epsilon_m} \sum_{l=0}^{\infty} \sum_{m=-l}^l \frac{q_{l,m}^*}{2l+1} \frac{Y_{l,m}(\theta, \phi)}{r^{l+1}}, \quad (3.3)$$

where $q_{l,m}$ are the components of the multipolar moments in their spherical form. The subscript l determines the order of the moment, and $m = -l, \dots, l$ denote its individual elements (but now the moment itself does

not have a form of a tensor). The symbol $(\cdot)^*$ denotes a complex conjugate, $Y_{l,m}(\theta, \phi) = \sqrt{\frac{(2l+1)(l-m)!}{4\pi(l+m)!}} P_{l,m}(\cos \theta) e^{im\phi}$ are so-called spherical harmonics defined using Legendre polynomials $P_{l,m}(\cos \theta)$ and finally $i = \sqrt{-1}$ is the imaginary unit.

Although the spherical form of multipolar moments clearly varies from the Cartesian one, they both represent the same quantity. By comparing the two expansions Eqs. (3.2) and (3.3), it is possible to find expressions for mutual conversion between the two formulations (as it was done for example in [23]). We will exploit the possibility to switch back and forth between these two descriptions in the paper.

3.2.1.2 EM method

Now we will show how to use the multipolar moments together with EM method for computation of the DEP force and torque acting on any polarized object placed in an inhomogeneous external electric field. Since, as was already stated in the introduction, harmonic fields of a sufficiently high frequency are used to avoid other unwanted electrokinetic effects, a time-averaged (over one period of a harmonic external electric field) force, $\langle \mathbf{F} \rangle$, and torque, $\langle \mathbf{T} \rangle$, are necessary to consider. They are given by the following formulas derived by Jones and Washizu in [13]

$$\langle \mathbf{F} \rangle = \sum_{n=1}^N \langle \mathbf{F}^{(n)} \rangle = \sum_{n=1}^N \frac{1}{2} \text{Re} \left[\frac{\tilde{\mathbf{p}}^{(n)} [\cdot]^n \nabla^n \tilde{\mathbf{E}}^*}{n!} \right], \quad (3.4)$$

$$\begin{aligned} \langle \mathbf{T} \rangle &= \sum_{n=1}^N \langle \mathbf{T}^{(n)} \rangle \\ &= \sum_{n=1}^N \frac{1}{2} \text{Re} \left[\frac{1}{(n-1)!} \left(\tilde{\mathbf{p}}^{(n)} [\cdot]^{n-1} \nabla^{n-1} \right) \times \tilde{\mathbf{E}}^* \right], \end{aligned} \quad (3.5)$$

where N is the order of approximation, $\mathbf{F}^{(n)}$ and $\mathbf{T}^{(n)}$ are the force and torque contributions, respectively, caused by a multipole of order n , $\langle \cdot \rangle$ denotes the time average, $\text{Re}[\cdot]$ is the real part of the expression, ∇ is the gradient operator, the dyadic operation $[\cdot]^n$ stands for n dot multiplications and $(\tilde{\cdot})$ is used to represent a phasor/complex quantity. Since only harmonic driving signals (electric fields or, actually, voltages) are considered, we can

compactly represent the related quantities using a phasor notation encoding both their amplitude and phase.

Notice that the only quantities we need to know in order to compute the force and torque are the external harmonic electric field $\tilde{\mathbf{E}}$ and the multipolar moments of the polarized object in their Cartesian form $\tilde{\mathbf{p}}^{(n)}$. While computation of the electric field is tractable even online (in real time, see section 3.2.6), the computation of general multipolar moments even in the offline regime is so far only available for spherical objects. In the following section we will at first show how these moments can be obtained offline using numerical FEM simulations, and then we will explain how to use the same approach in a computational scheme achieving real-time performance. This will enable us to compute the DEP force and torque Eqs. (3.4) and (3.5) acting on an arbitrarily shaped and oriented object in an arbitrary external electric field in real time.

3.2.2 Numerical computation of multipolar moments for arbitrarily-shaped objects

In the development, we will use the spherical form of multipoles here, because we will advantageously use their orthogonality property. The result can then be always translated to the Cartesian form as explained in the previous section. We will start with Eq. (3.3) for potential, which we will invert and express the individual multipolar moments $q_{l,m}$ as functions of the potential Φ_{object} (obtained through numerical simulation). This potential field can be obtained by subtracting two numerical simulations $\Phi_{\text{filled}} - \Phi_{\text{empty}}$.

For further development the following property of spherical harmonics

$$\oint_{S(R)} Y_{l,m}(\theta, \phi) Y_{l',m'}^*(\theta, \phi) d\Omega = R^2 \delta_{ll'} \delta_{mm'}, \quad (3.6)$$

which stems from their orthonormality, is of particular importance. In the expression above, δ_{ij} is the Kronecker delta and $d\Omega = \sin\theta d\theta d\phi$, since the integration is over a unit sphere. Other two useful properties are the following conjugation rules for spherical harmonics and spherical multipolar moments

$$q_{l,m}^* = (-1)^m q_{l,-m} \quad \text{and} \quad Y_{l,-m} = (-1)^m Y_{l,m}^*. \quad (3.7)$$

At first, let's apply the first conjugation rule from Eq. (3.7) to the potential expression in Eq. (3.3). We get

$$\Phi_{\text{object}}(\mathbf{r}) = \frac{1}{\epsilon_0 \epsilon_m} \sum_{l=0}^{\infty} \sum_{m=-l}^l \frac{(-1)^m q_{l,-m} Y_{l,m}(\theta, \phi)}{2l+1} \frac{1}{r^{l+1}}. \quad (3.8)$$

Next, we change the order of summation and apply the second conjugation rule from Eq. (3.7). We then multiply both sides of the equation by $Y_{l',m'}(\theta, \phi)$ and perform the integration over a sphere $S(R)$ (recall that $S(R)$ is a virtual sphere encapsulating the object of interest). Here l' and m' are just auxiliary indices used to represent some specific spherical harmonic function. We obtain

$$\begin{aligned} & \oint_{S(R)} \Phi_{\text{object}}(\mathbf{r}) Y_{l',m'}(\theta, \phi) dS \\ &= \oint_{S(R)} \frac{1}{\epsilon_0 \epsilon_m} \sum_{l=0}^{\infty} \sum_{m=-l}^l \frac{q_{l,m} Y_{l,m}^*(\theta, \phi)}{2l+1} \frac{1}{r^{l+1}} Y_{l',m'}(\theta, \phi) dS. \end{aligned} \quad (3.9)$$

Most of the terms on the right-hand side are independent on the integration variable, and thus they can be factored out in front of the integral. Thanks to Eq. (3.6), almost all of the summands vanish. The only one remaining is the one for $l = l'$, $m = m'$, which enables us to express the associated multipolar moment as

$$\begin{aligned} q_{l',m'} &= \frac{(2l'+1)\epsilon_0 \epsilon_m}{R^{1-l'}} \\ &\quad \times \oint_{S(R)} \Phi_{\text{object}}(\mathbf{r}) Y_{l',m'}(\theta, \phi) dS \end{aligned} \quad (3.10)$$

just based on the potential $\Phi(\mathbf{r})$ of the polarized object. Indices l' and m' can now be switched back to l and m , respectively, to match the original notation

$$q_{l,m} = \frac{(2l+1)\epsilon_0 \epsilon_m}{R^{1-l}} \oint_{S(R)} \Phi_{\text{object}}(\mathbf{r}) Y_{l,m}(\theta, \phi) dS. \quad (3.11)$$

All we need to know to evaluate Eq. (3.11) and thus to compute the multipolar representation of the object is a potential Φ_{object} on a surface of a virtual sphere $S(R)$ encapsulating it. It is interesting to note here, that

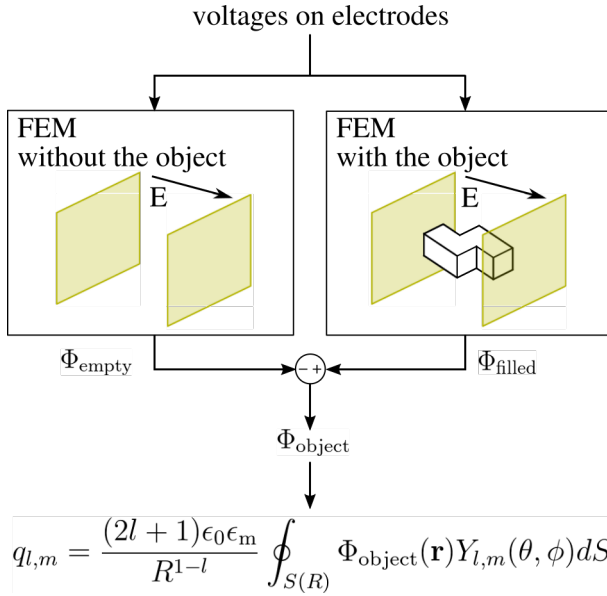


Figure 3.1: Illustration of the procedure for extracting the spherical multipolar moments $q_{l,m}$ of arbitrary order for objects having an arbitrary shape. Here a Tetris “S/Z”-shaped object placed in between two planar electrodes generating the external electric field is used as an example.

since we perform the integration over the surface of $S(R)$, Eq. (3.11) is kind of independent of the particular object’s shape and it may seem that we are describing the polarization of the whole sphere instead of the polarization of the object itself. Indeed, the resulting multipolar moments describe the entire polarization-induced charge structure contained in $S(R)$, which may even go slightly beyond the boundaries of the object itself, but this is precisely the quantity of interest for the DEP force and torque computation.

Figure 3.1 summarizes the procedure for obtaining multipolar representation of an arbitrarily shaped and oriented object located in an arbitrary electric field including the calculation of Φ_{object} using the two FEM numerical simulations. As already noted above, the size of the sphere $S(R)$ is chosen to incorporate just the very charge structure resulting from the polarization of the object of interest. In our implementation, we make R around 1% bigger than is the half of the longest dimension of the object. This ensures that we capture the majority of the polarization induced charge

and also, depending on the particular implementation details, it can facilitate the meshing of the FEM model. In the following sections, we will show how to make this process real-time.

3.2.3 Superposition as the key principle

The problem of the previously described method is that every time the Φ_{object} changes, two time-consuming FEM simulations have to be carried out. This happens when either the voltages on electrodes, the position of the object or its orientation changes, because then also the external electric field with respect to the object of interest changes (in fact, this is the only thing that matters).

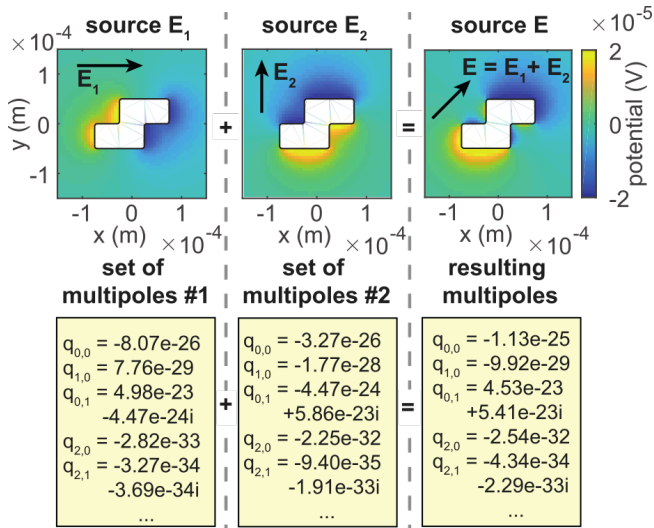


Figure 3.2: Illustration of the superposition principle. Here the three uniform fields are $\mathbf{E}_1 = [1, 0, 0]^T$ V/m, $\mathbf{E}_2 = [0, 1, 0]^T$ V/m and $\mathbf{E} = [1, 1, 0]^T$ V/m. We provide a complete list of all computed spherical multipoles together with their Cartesian equivalents in the supplemental material [24].

A solution to this problem is to utilize the principle of superposition holding for an electric potential and as a consequence also for the multipolar moments (it can be seen for example from Eq. (3.11)). As Fig. 3.2 illustrates, we can obtain a multipolar representation of the object polarized by a sum $\mathbf{E}_1 + \mathbf{E}_2$ of two different electric fields as a sum of multipolar moments

generated by each of these fields separately. In this example a sum of two homogeneous electric fields is used for simplicity, but in general the same principle holds also for any linear combination of any number of even inhomogeneous electric fields and the corresponding multipolar descriptions they generate.

If we, in advance, compute and store the multipolar representation for a set of external fields forming a basis of all the possible source fields (instead just for \mathbf{E}_1 and \mathbf{E}_2), we can then get the multipoles associated to an arbitrary external field just in time necessary for computation of a linear combination.

The basic idea is therefore at first to run a set of offline computations to construct a *basis table of solutions* containing couples of *external electric field basis elements* and the *multipolar representations* of the object polarized by such field. Afterward, the principle of superposition could be used for online (real-time) computation, in which just the rows of the precomputed table are combined. The technicalities of this key idea will be further detailed below starting with the choice of the basis elements for the source electric field.

3.2.4 Basis of the source electric field

In this section, we will introduce two distinct but equivalent methods, in which the source electric field polarizing the object of interest can be described. Similarly to the case of multipolar moments, each of these formulations will be advantageous in different situations. We will also show how to convert back and forth between them.

One way to derive a basis, through which we can describe the source electric field polarizing the object of interest, is to start off with a Taylor series expansion of the electric field around the center position of the object. The values of spatial derivatives of the field constituting the individual terms of the series can then be used as coordinates with respect to a basis composed of all the available unit spatial derivatives. The similarity to the multipolar description of potential is of course not coincidental here. If the field had to be described accurately, an infinite basis would be needed. In practice, however, its approximation using a finite basis will be sufficient. Anyway, we have to choose and use some order n of approximation for force and torque computations using the EM method, and therefore it gives no sense to consider electric fields with nonzero spatial derivatives of the order

higher than $n - 1$ here—the polarization caused by such an electric field could not be represented by multipolar moments of orders only up to n anyway.

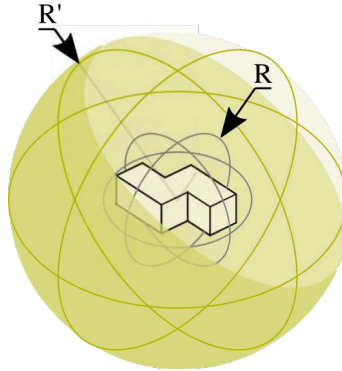


Figure 3.3: Geometry used in the FEM solver. The larger sphere S' with a radius R' is used for setting the potential boundary conditions determining the source polarizing electric field. The smaller sphere S with a radius R defines a virtual surface over which we integrate in Eq. (3.11).

This representation is, however, not particularly well suited for defining the external electric field in numerical FEM simulations. Here, the field has to be represented purely just by boundary potential conditions. Therefore we encapsulate the object of interest in a sphere S' with a radius $R' > R$ (see Fig. 3.3), whose surface will carry these boundary conditions defying the polarizing electric field in its interior. The greater the R' is, the more accurate results of numerical FEM simulation will be (because of the mitigation of boundary effects), but also the more time and memory demanding will the computation be. In our implementation we used $R' \approx 10R$. Using the above-specified construction, the description of an arbitrary source electric field translates into a description of an arbitrary potential on the surface of $S'(R')$, to which purpose we can use the expression Eq. (3.3) evaluated on the given spherical surface. Thanks to the orthogonality of spherical harmonics, each of the addends represent one of the mutually orthogonal basis elements with elements $q_{l,m}$ serving as the corresponding coordinates. Mutual orthogonality of potentials means also a mutual orthogonality of the corresponding source electric fields. Similarly to the first case, it is sufficient to use only the first n multipolar moments to represent the source

electric field, since representing it more accurately would not give us any further benefit. To distinguish that these spherical multipolar moments do not represent the potential of a polarized object, but rather describe the external source electric field, we will use the superscript “E”— $q_{l,m}^E$ s.

To derive the expression converting the first mentioned representation into the second one, we will do a thought experiment. Consider that the sphere, whose surface is used to define our potential boundary conditions, is filled by an ideally polarizable material. Under such condition, the external electric field should vanish inside the sphere, and the resulting potential on its surface should be therefore exactly opposite to the external source potential field—the one we want to describe. Obtaining the multipolar description of this hypothetical ideally polarized sphere (and switching the signs) would therefore give us the result. Since for a sphere, there exist an analytical expression for multipoles, we can easily obtain moments describing the desired potential. We utilize a formula

$$\mathbf{p}^{(n)} = \frac{4\pi\epsilon_0\epsilon_m R^{(2n+1)} n K^{(n)}}{(2n-1)!!} \nabla^{(n-1)} \mathbf{E}, \quad (3.12)$$

from [13] and evaluate it for such a hypothetical case of ideal polarization. Polarizability of the sphere is determined by its material properties (electric permittivity and conductivity) contained in $K^{(n)}$, the so-called generalized Clausius-Mossotti factor defined for example in [14]. For the considered case of ideally polarizable sphere $K^{(n)} \rightarrow \frac{1}{n}$. We can therefore represent the potential on the sphere of interest using the multipolar moments

$$\mathbf{p}^{E,(n)} = -\frac{4\pi\epsilon_0\epsilon_m R^{(2n+1)}}{(2n-1)!!} \nabla^{(n-1)} \mathbf{E}. \quad (3.13)$$

The minus sign is there to take into account the fact that the potential due to such polarization would be opposite to the original one as already noted above. The resulting Cartesian multipole can then be just converted to its spherical form giving us the final q^E s. Conversion in the opposite direction can be done analogously.

3.2.5 Offline computation—constructing the basis table

In this section we will cover all the details and technicalities encountered during the basis table construction.

Table 3.1: Inputs to the offline computation

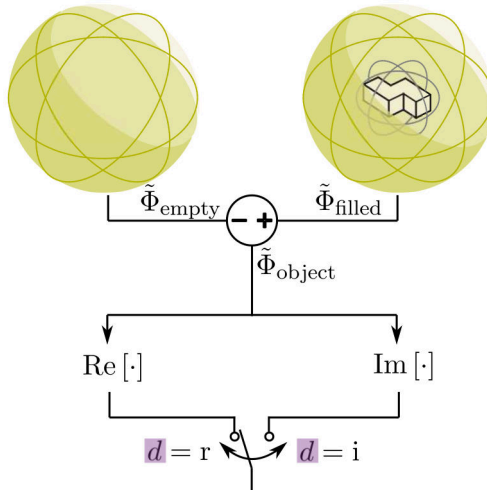
sim No.	multipolar moments						
	$q_{0,0}^B$	$q_{1,0}^B$	$q_{1,1}^B$	$q_{2,0}^B$	$q_{2,1}^B$	$q_{2,2}^B$	\dots
1	0	1	0	0	0	0	\dots
2	0	0	1	0	0	0	\dots
3	0	0	i	0	0	0	\dots
4	0	0	0	1	0	0	\dots
5	0	0	0	0	1	0	\dots
6	0	0	0	0	i	0	\dots
7	0	0	0	0	0	1	\dots
8	0	0	0	0	0	i	\dots
\vdots	\vdots	\vdots	\vdots	\vdots	\vdots	\vdots	\ddots

To generate the basis we have to compute the multipolar moments of the object when polarized by each individual basis element of the source electric field. In practice, we do this by taking individual rows of Table 3.1 defying the basis elements, fitting the corresponding q^B s into Eq. (3.3) (for qs) and applying the resulting potential as the boundary condition on the surface of $S'(R')$ of the FEM simulations. The superscript “B” denotes that q^B s are used here to define the *external* or source electric field. Note that the monopole term $q_{0,0}^B$ is always equal to zero since we assume that the object is electrically neutral. Further note that there are no negative indices related to q^B s. The reason is to save both computational time and storage space, as these can be determined by the above-stated conjugation rules (Eq. (3.7)). Since spherical multipolar moments are in general complex quantities, we have to also take into account their imaginary parts as can be seen for example in the 3rd-, 6th- or 8th-row of Table 3.1. An exception here are the elements $q_{a,0}^B$, $a \in \mathbb{Z}$, which have the imaginary part always equal to zero (this can be seen again from the conjugation rules in Eq. (3.7)). Having the boundary potential conditions set, we then always perform two simulations—one without the object and the other with it. Subtracting these two (according to Fig. 3.1) we get the potential $\tilde{\Phi}_{\text{object}}$ of the polarized object serving as an input for computation of the multipoles.

So far, we silently considered only electrostatic source fields and the corresponding real potential fields in sections 3.2.1 and 3.2.3. Also the expression Eq. (3.11) accepts only real potentials. But as the tilde in $\tilde{\Phi}_{\text{object}}$

$$q_{l,m} = \begin{cases} 1 & \text{if } l = \mathbf{a} \wedge m = \mathbf{b} \wedge \mathbf{c} = \mathbf{r} \\ i & \text{if } l = \mathbf{a} \wedge m = \mathbf{b} \wedge \mathbf{c} = \mathbf{i} \\ 0 & \text{otherwise} \end{cases}$$

used in (3) to get boundary potential conditions for FEM simulations



used in (11) to compute multipolar moments

$$\begin{matrix} q_{10} & q_{20} \\ q_{11} & q_{21} & \dots \\ & q_{22} \end{matrix}$$

we mark each of the computed moments with 4 superscripts encoding the settings used for its computation

$$q_{l,m}^{abcd}, \quad l = 0 \dots n, \quad m = 0 \dots l$$

Figure 3.4: Generating and denoting the basis elements.

Table 3.2: Outputs from the offline computation

sim No.	stored data table					
1	$q_{1,0}^{10rr}$	$q_{1,1}^{10rr}$	$q_{2,0}^{10rr}$	$q_{2,1}^{10rr}$	$q_{2,2}^{10rr}$	\dots
	$q_{1,0}^{10ri}$	$q_{1,1}^{10ri}$	$q_{2,0}^{10ri}$	$q_{2,1}^{10ri}$	$q_{2,2}^{10ri}$	\dots
2	$q_{1,0}^{11rr}$	$q_{1,1}^{11rr}$	$q_{2,0}^{11rr}$	$q_{2,1}^{11rr}$	$q_{2,2}^{11rr}$	\dots
	$q_{1,0}^{11ri}$	$q_{1,1}^{11ri}$	$q_{2,0}^{11ri}$	$q_{2,1}^{11ri}$	$q_{2,2}^{11ri}$	\dots
3	$q_{1,0}^{11ir}$	$q_{1,1}^{11ir}$	$q_{2,0}^{11ir}$	$q_{2,1}^{11ir}$	$q_{2,2}^{11ir}$	\dots
	$q_{1,0}^{11ii}$	$q_{1,1}^{11ii}$	$q_{2,0}^{11ii}$	$q_{2,1}^{11ii}$	$q_{2,2}^{11ii}$	\dots
4	$q_{1,0}^{20rr}$	$q_{1,1}^{20rr}$	$q_{2,0}^{20rr}$	$q_{2,1}^{20rr}$	$q_{2,2}^{20rr}$	\dots
	$q_{1,0}^{20ri}$	$q_{1,1}^{20ri}$	$q_{2,0}^{20ri}$	$q_{2,1}^{20ri}$	$q_{2,2}^{20ri}$	\dots
\vdots	\vdots	\vdots	\vdots	\vdots	\vdots	\ddots

indicates, the potential of the polarized object is generally complex. Even if the potential boundary conditions applied to the sphere surface are purely real, the differences in the material properties of the object and its surrounding medium (specifically their electric conductivities and permittivities) can cause the shift in the field's phase. We have to therefore treat separately the real and imaginary parts of the potential— $\text{Re} \left[\tilde{\Phi}_{\text{object}} \right]$ and $\text{Im} \left[\tilde{\Phi}_{\text{object}} \right]$, respectively. The two corresponding sets of multipolar moments have to be kept separately during storage as well as during subsequent calculations. Four superscripts will be used to denote the specific elements $q_{l,m}^{abcd}$ of the precomputed basis table. The first three superscripts encode the external source electric field used in the simulation. A field that is given by $q_{l,m}^B = 0$ except for a case when $l = a$ and $m = b$. In such situation the corresponding element of multipolar moment, $q_{a,b}^B$, is equal to either real or imaginary unit based on whether the third superscript $c = r$ or $c = i$, respectively. The last superscript d then determines whether it is the real ($d = r$) or the imaginary ($d = i$) part of $\tilde{\Phi}_{\text{object}}$, which is considered. Following this notation, $q_{2,1}^{10ir}$ is for example the second element of the second order spherical multipolar moment extracted from a simulation, in which the external source potential on $S'(R')$ was given by real part of Eq. (3.3) evaluated with $q_{1,0} = i$ and all the other $q_{l,m} = 0$ for $l \neq 1 \wedge m \neq 0$. The above is summarized in Fig. 3.4.

From each simulation, we will therefore obtain $2 \cdot (1 + 2 + \dots + n) = n(n + 1)$ complex values—the elements of our basis table of solutions. We store them in a table alongside with the corresponding q^E s describing the source

electric field. For illustration, please see Table 3.2, where the reference to the source electric field is made through the specific simulation number.

3.2.6 Computing the electric field

We generate the field typically by applying voltages on the set of micro-electrodes (see for example our DEP systems [9, 25]). Knowing the voltage signals applied to the electrodes, we can compute the electric field and its spatial derivatives (encoding also the field’s inhomogeneity) at the object’s location. In some specific cases of electrode designs an analytical solution may be known (for example for the interdigitated electrode arrays [26, 27]), in others one has to settle for the numerical solution [25] or combined approaches [28, 29].

Here we used an approximate method based on Green’s functions similar to the one described in [28]. Its advantage is that it results in an analytical expression of potential, though only approximate and very complicated. Still, we can differentiate it and thus obtain higher spatial derivatives of the electric field than what could be possible with a FEM-based numerical solution. In contrast to the referred solution, we used a slightly different discretization scheme. Instead of using semi-infinite rectangles suitable for the electrode array, we divided the electrode plane into small enough square bins enabling us to approximate arbitrary shapes of the electrodes. The same approach as in [9, 25]) using the lookup table for electric field and its derivatives was used to obtain the field in real time. These are then (using Eq. (3.13) and subsequent conversion to spherical form of multipoles) represented by $q_{l,m}^E$ s for further use in the online computation.

3.2.7 Online computation—doing the linear combination

Knowing the precomputed basis table of multipolar moments and the external electric field expressed using q^E s, we can obtain the resulting multipolar moments by a linear combination as mentioned in section 3.2.3.

At first, let’s for simplicity assume that the source electric field is just real. Even in this simplified case, we have to, when doing the linear combination, make sure that we combine always just the mutually corresponding elements of the source field and the basis.

$$q_{l,m}^{cr} = \sum_{l'=1}^n \sum_{m'=0}^{l'} \operatorname{Re} [q_{l',m'}^E] q_{l,m}^{l'm'cr}, \text{ where } c \in \{r, i\}, \quad (3.14)$$

$$q_{l,m}^{ci} = \sum_{l'=1}^n \sum_{m'=0}^{l'} \text{Im} [q_{l',m'}^E] q_{l,m}^{l'm'ci}, \text{ where } c \in \{r, i\}. \quad (3.15)$$

This way we get for every l and m (denoting the specific l th element of the resulting multipolar moment of order m) four quantities: $q_{l,m}^{rr}$, $q_{l,m}^{ri}$, $q_{l,m}^{ir}$ and $q_{l,m}^{ii}$. Each of these spherical moments are then converted back to their Cartesian form ($q_{n,0}^{cd}, q_{n,1}^{cd}, \dots, q_{n,n}^{cd} \rightarrow \mathbf{p}^{(n),cd}$ where $c, d \in \{r, i\}$) and assembled the following way to just one final complex Cartesian moment

$$\mathbf{p}^{(n)} = (\mathbf{p}^{(n),rr} + \mathbf{p}^{(n),ri}) + i(\mathbf{p}^{(n),ir} + \mathbf{p}^{(n),ii}). \quad (3.16)$$

In this form, they can be finally used to compute the dielectrophoretic force and torque.

In a case when the source potential itself can be complex (e.g. when there are phase-shifted signals applied to the electrodes), we will have instead of just one set of linear combination coefficients $q_{a0}^E, q_{a1}^E, \dots, q_{aa}^E$, two such sets: $q_{a0}^{E,r}, q_{a1}^{E,r}, \dots, q_{aa}^{E,r}$ and $q_{a0}^{E,i}, q_{a1}^{E,i}, \dots, q_{aa}^{E,i}$ representing the real and the imaginary part of the external electric field, respectively. The linear combination of the basis elements then reads

$$q_{l,m}^{cdr} = \sum_{l'=1}^n \sum_{m'=0}^{l'} \text{Re} [q_{l',m'}^{E,c}] q_{l,m}^{l'm'dr}, \quad c, d \in \{r, i\}, \quad (3.17)$$

$$q_{l,m}^{cdi} = \sum_{l'=1}^n \sum_{m'=0}^{l'} \text{Im} [q_{l',m'}^{E,c}] q_{l,m}^{l'm'di}, \quad c, d \in \{r, i\}, \quad (3.18)$$

giving us for every l and m eight quantities: $q_{l,m}^{rrr}$, $q_{l,m}^{rri}$, $q_{l,m}^{rir}$, $q_{l,m}^{rii}$, $q_{l,m}^{irr}$, $q_{l,m}^{iri}$, $q_{l,m}^{iir}$ and $q_{l,m}^{iii}$. These are then again converted to their Cartesian form and combined together the following way

$$\begin{aligned} \mathbf{p}^{(n)} = & \left((\mathbf{p}^{(n),rrr} + \mathbf{p}^{(n),rri}) + i(\mathbf{p}^{(n),rir} + \mathbf{p}^{(n),rii}) \right) \\ & + i \left((\mathbf{p}^{(n),irr} + \mathbf{p}^{(n),iri}) + i(\mathbf{p}^{(n),iir} + \mathbf{p}^{(n),iii}) \right) \end{aligned} \quad (3.19)$$

to get one resulting Cartesian moment suitable for DEP force and torque computations using Eq. (3.4) and Eq. (3.5).

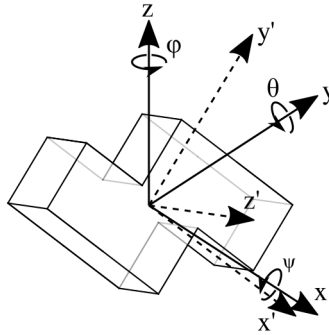


Figure 3.5: Since the basis in Table 3.2 was precomputed for an object having certain fixed orientation,

3.2.8 Considering orientation of the object

So far, we considered the orientation of the object to be fixed. In practice, however, the manipulated object can freely revolve in space and thus change its orientation as it moves through the medium. From the force and torque computation point of view, it is just the *relative* orientation of the object with respect to the field, which is important. Instead of rotating the object (leading to recomputation of the basis table), it is therefore better to express the electric field and its necessary spatial derivatives in a new rotated frame of reference, which is always attached to it as shown in Fig. 3.5. After performing the force and torque computation, the results have to be again translated back into the original global coordinate system. We do so by merely multiplying the resulting column vectors of forces and torques from left by a corresponding rotational matrix

$$\begin{aligned}
 \mathbf{R} = & \begin{bmatrix} \cos(\phi) & -\sin(\phi) & 0 \\ \sin(\phi) & \cos(\phi) & 0 \\ 0 & 0 & 1 \end{bmatrix} \cdot \begin{bmatrix} \cos(\theta) & 0 & \sin(\theta) \\ 0 & 1 & 0 \\ -\sin(\theta) & 0 & \cos(\theta) \end{bmatrix} \\
 & \cdot \begin{bmatrix} 1 & 0 & 0 \\ 0 & \cos(\psi) & -\sin(\psi) \\ 0 & \sin(\psi) & \cos(\psi) \end{bmatrix}
 \end{aligned} \tag{3.20}$$

3.2.9 Summary

The above-described control-oriented model may be summarized using the pseudocodes in Algorithm 1 for the preprocessing procedure and in Algorithm 2 for the part of the model evaluated in real time.

Algorithm 1 Preprocessing steps (offline)

- 1: **for all** sets of multipolar moments given by rows of Table 3.1 **do**
 - 2: load a FEM simulation model for an empty spherical domain
 - 3: set the boundary potential condition on a surface of the sphere according to Eq. (3.3)
 - 4: solve for the potential Φ_{empty} inside a sphere
 - 5: load a FEM simulation model for a spherical domain with an object of interest being placed inside it
 - 6: set the boundary potential condition on a surface of the sphere according to Eq. (3.3)
 - 7: solve for the potential Φ_{filled} inside a sphere
 - 8: compute $\Phi_{\text{object}} = \Phi_{\text{filled}} - \Phi_{\text{empty}}$
 - 9: extract the values of spherical multipolar moments using Eq. (3.11)
 - 10: store the extracted moments alongside with the corresponding row of Table 3.1 (description of the source field) as for example shown in Table 3.2
 - 11: **end for**
-
- 12: define a dense enough grid of points in space in which we would like to compute DEP force and torque Afterward
 - 13: **for all** of the electrodes **do**
 - 14: **for all** points in the grid **do**
 - 15: compute the electric field and its various spatial derivatives using the Green's function approach for a situation when a potential of 1 V is set to the specific electrode and the rest of them is kept grounded
 - 16: **end for**
 - 17: **end for**
 - 18: store the results as a lookup table
-

Algorithm 2 Real-time evaluation steps (online)

- 1: compute the electric field derivatives at the point in space where the object is located (using interpolation in the precomputed lookup table and the principle of superposition)
 - 2: get the Cartesian multipoles describing the potential on a virtual ideally polarizable sphere centered at the object's location (using expression Eq. (3.13))
 - 3: convert them to spherical form of multipolar moments
 - 4: use the results as the coefficients of the linear combination of the precomputed basis elements (see step 10 of Algorithm 1)
 - 5: convert the resulting multipolar moments back into the Cartesian formulation
 - 6: use the EM method to compute the DEP force and torque (Eq. (3.5))
-

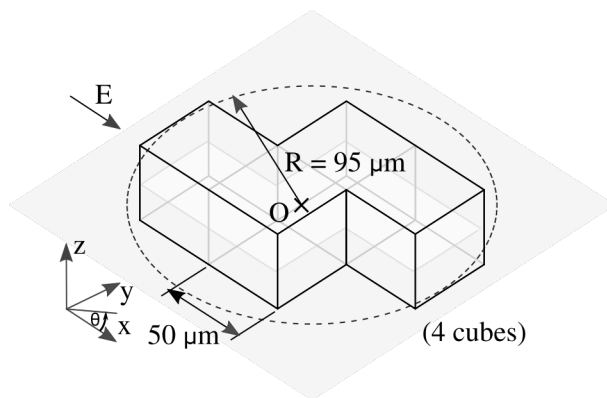


Figure 3.6: Dimensions of the Tetris-shaped micro-object used in the example and validation simulations.

3.3 Results and discussion

A Tetris “S/Z” piece depicted in Fig. 3.6 was used as an example of an object, for which the real-time force and torque computations were so far unavailable. The dimensions of the object are included in the picture.

At first, we will demonstrate the validity of the derived Eq. (3.11). Consider an object polarized by an uniform external electric field with an in-

tensity of 1 V/m pointing along the x -axis.

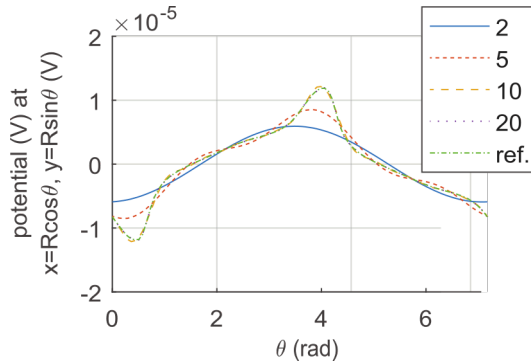


Figure 3.7: Comparison of potentials along the circle laying in the xy -plane and enclosing the object as depicted in Fig. 3.6 for various orders of approximation.

We use Eq. (3.11) to compute the multipolar representation of the object, and then we put the results back into Eq. (3.3) and compare the reconstructed potential against the solution obtained numerically using COMSOL MULTIPHYSICS 5.1. Figure 3.7 shows the results for various orders of approximation. The higher the order of multipoles, the more accurate the representation of the potential.

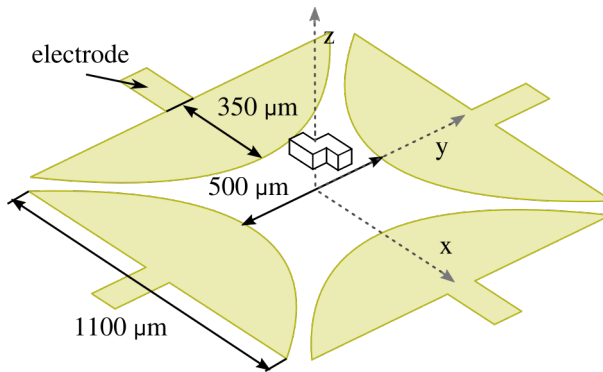


Figure 3.8: Dimensions of the electrode array and Tetris-shaped micro-object used in the validation simulations.

To prove the validity of the model as a whole, we compared its outcomes against the reference solutions obtained from COMSOL MULTIPHYSICS 5.1,

where we performed time-independent computations of DEP forces and torques using MST method. As a test scenario, we used the so-called quadrupolar electrode array, which is usually used for torque generation in electrorotation experiments, but it can equally easily generate a DEP force. It is shown together with all the relevant dimensions in Fig. 3.8. As the driving signals, we used four sinusoidal waveforms having amplitudes 10, 10, 50 and 50 V, respectively, and phase shifts 0° , 90° , 180° and 270° , respectively. The object's orientation was set such that from its initial orientation (as depicted in Fig. 3.8) it was rotated by 45° and 25° subsequently about the x - and y -axis. Its geometric center was placed on the z -axis. DEP forces and torques were then computed for values of z ranging from from $60\ \mu\text{m}$ to $150\ \mu\text{m}$. To keep the errors negligible, we used moments up to the 5th order (32-poles). Note that to accurately represent polarization of non-spherical objects the higher order multipolar moments will be necessary even when the external electric field is uniform as could be already seen in the potential comparison shown in Fig. 3.7.

The results plotted in Figs. 3.9 and 3.10 show that our model resembles well the reference solution when high enough order of multipoles is used. At lower z -coordinates, when the object is close to the edges of the electrodes, the electric field around the object becomes more inhomogeneous. Consequently, the accuracy of the solution gets worse. Surprisingly, the higher-order multipoles do not improve the accuracy of solution in this region. This is in contrast with the cases of higher z -coordinates, where the accuracy does improve with increasing order of the multipole. We suspect that the reason for this is a not accurate enough computation of the electric field and especially its higher order spatial derivatives near the electrodes. Since the method of Green's function, which we use for computation of the external electric field, uses just an approximation of the potential boundary conditions on the electrodes, it can not provide accurate enough results in their vicinity.

During the simulations made above, we measured the times required for computation of DEP forces and torques by both the MST method and our proposed model. A conventional PC (Intel Core i5, 3.30 GHz, 8 GB RAM, 64-bit, Win 7) was used. The results for different orders of approximation are stated in Table 3.3. The evaluation of our model is much faster than performing the numerical simulation for the MST method. Nevertheless, with the increasing number of multipoles, the computational time t (in seconds) rises exponentially approximately according to $t = (9.768 \times 10^{-6}) e^{1.37n}$,

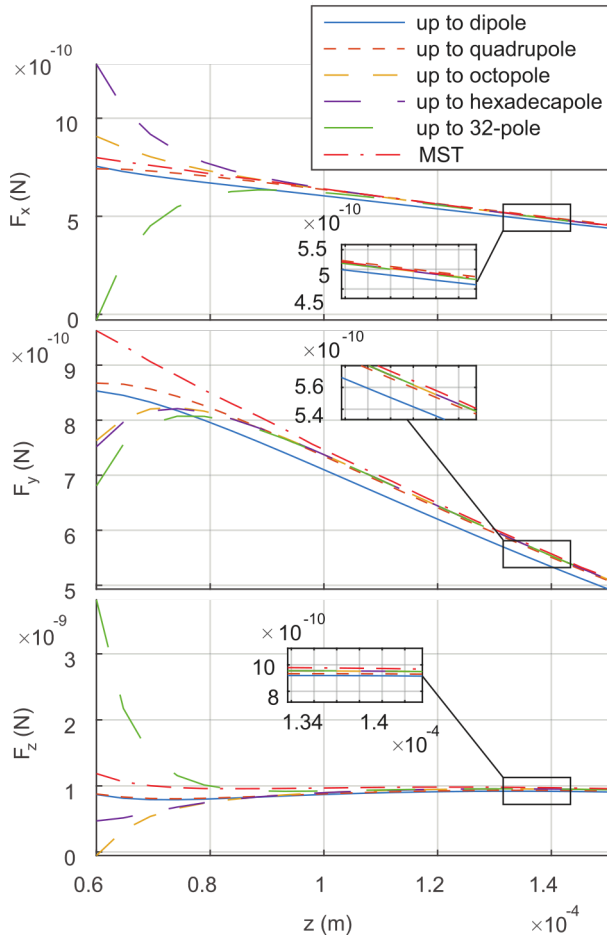


Figure 3.9: Comparison of the force prediction obtained by the described model and the reference MST model.

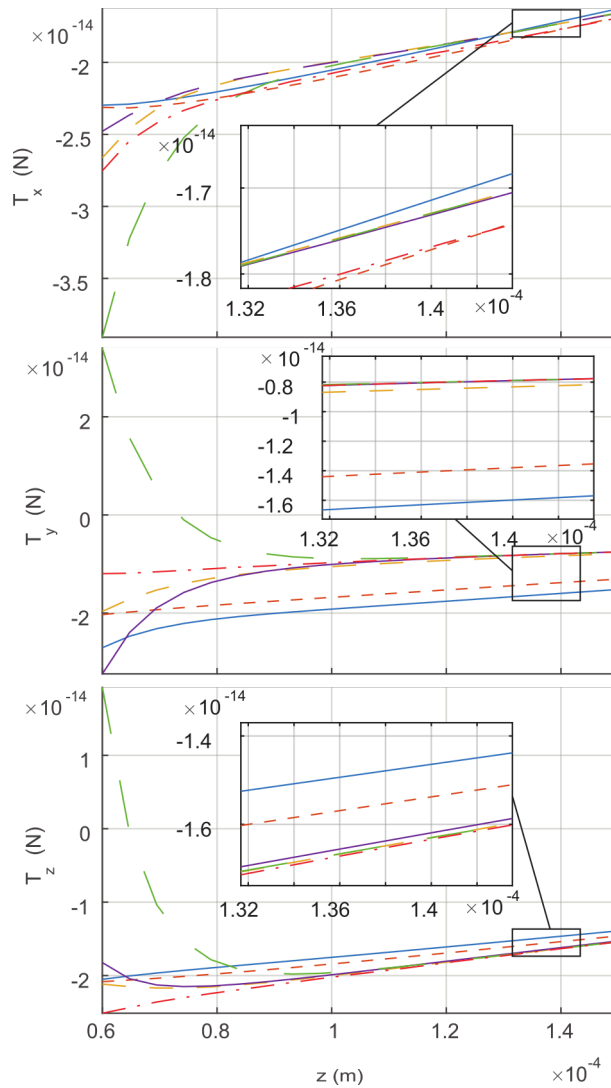


Figure 3.10: Comparison of the torque prediction obtained by the described model and the reference MST model.

Table 3.3: Comparison of the computational times of different models

	Model	Computational time
EM method	$n = 1$ (dipole)	0.1 ms
	$n = 2$ (quadrupole)	0.2 ms
	$n = 3$ (octopole)	0.6 ms
	$n = 4$ (hexadecapole)	2.1 ms
	$n = 5$ (32-pole)	9.3 ms
	Maxwell stress tensor method	1 h 40 m 57 s

which means that the highest possible multipole computable under the time limit of 1 s would in the current implementation be the 256-pole ($n = 8$).

Since all the necessary numerical simulations can be done in advance (and just once for every new shape of the object), the real-time evaluation of the model takes only fractions of a second in comparison with hours of MST computation. Our MATLAB implementation of the described mathematical model can be found at <https://goo.gl/eGZY7P>.

3.4 Conclusion

We introduced a simulation scheme based on EM method capable of real-time computation of the DEP forces and torque acting on objects of arbitrary shapes under arbitrary orientations and located in arbitrary electric fields. The enabling ingredient is the use of numerical solutions of the Laplace equation for getting the multipolar description of objects under such general scenarios. A specific way of how to construct a solution basis (from precomputed solutions) is then described so that all further computations can be done in real time. As such, the described control-oriented model could be used in future for simultaneous control of position and orientation of non-spherical objects with the envisioned biology and micro-assembly applications.

3.5 Bibliography

- [1] Tomáš Michálek, Aude Bolopion, Zdeněk Hurák, and Michaël Gauthier. Control-oriented model of dielectrophoresis and electrorotation

-
- for arbitrarily shaped objects. *Physical Review E*, 99(5):053307, May 2019. doi: 10.1103/PhysRevE.99.053307.
- [2] Herbert A. Pohl. *Dielectrophoresis: The Behavior of Neutral Matter in Nonuniform Electric Fields*. Cambridge University Press, Cambridge ; New York, December 1978. ISBN 978-0-521-21657-9.
- [3] X.-B. Wang, Y. Huang, F. F. Becker, and P. R. C. Gascoyne. A unified theory of dielectrophoresis and travelling wave dielectrophoresis. *Journal of Physics D: Applied Physics*, 27(7):1571–1574, July 1994. ISSN 0022-3727. doi: 10.1088/0022-3727/27/7/036.
- [4] U. Lei and Y. J. Lo. Review of the theory of generalised dielectrophoresis. *IET Nanobiotechnology*, 5(3):86–106, September 2011. ISSN 1751-875X. doi: 10.1049/iet-nbt.2011.0001.
- [5] Thomas B. Jones and Thomas Byron Jones. *Electromechanics of Particles*. Cambridge University Press, September 2005. ISBN 978-0-521-01910-1. doi: 10.1017/cbo9780511574498.
- [6] Hywel Morgan and Nicolas G. Green. *AC Electrokinetic: Colloids and Nanoparticles*. Research Studies Pr, Philadelphia, PA, 1st edition edition, June 2002. ISBN 978-0-86380-255-3.
- [7] Michael Pycraft Hughes. *Nanoelectromechanics in Engineering and Biology*. CRC Press, October 2002. ISBN 978-0-8493-1183-3.
- [8] Ronald R. Pethig. *Dielectrophoresis: Theory, Methodology and Biological Applications*. Wiley, Hoboken, NJ, 1 edition edition, May 2017. ISBN 978-1-118-67145-0.
- [9] Jiří Zemánek, Tomáš Michálek, and Zdeněk Hurák. Feedback control for noise-aided parallel micromanipulation of several particles using dielectrophoresis. *ELECTROPHORESIS*, 36(13):1451–1458, July 2015. ISSN 1522-2683. doi: 10.1002/elps.201400521.
- [10] Xujing Wang, Xiao-Bo Wang, and Peter R. C. Gascoyne. General expressions for dielectrophoretic force and electrorotational torque derived using the Maxwell stress tensor method. *Journal of Electrostatics*, 39(4):277–295, August 1997. ISSN 0304-3886. doi: 10.1016/S0304-3886(97)00126-5.
-

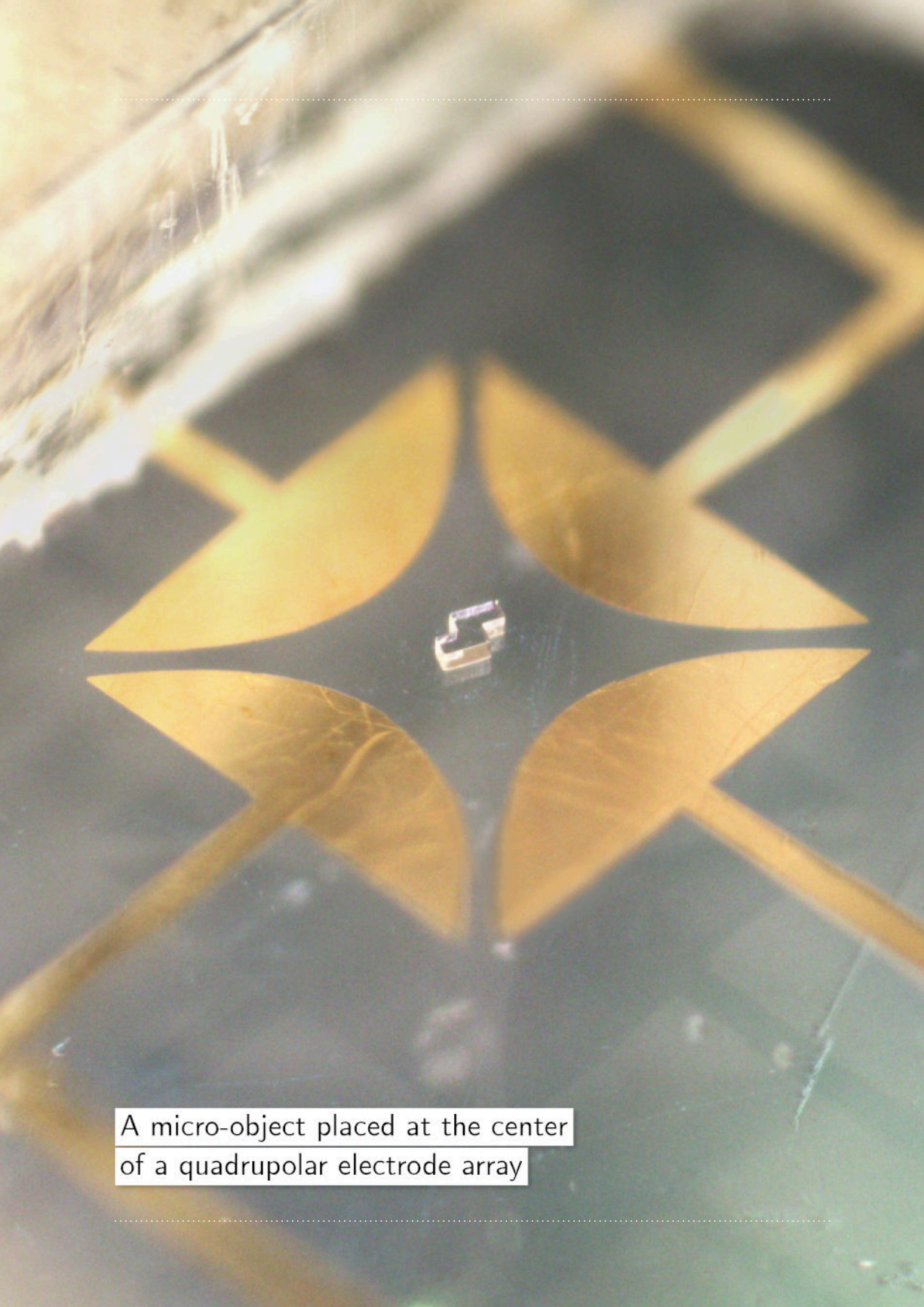
- [11] T. B. Jones. Dielectrophoretic force calculation. *Journal of Electrostatics*, 6(1):69–82, February 1979. ISSN 0304-3886. doi: 10.1016/0304-3886(79)90025-1.
- [12] Masao Washizu and T. B. Jones. Multipolar dielectrophoretic force calculation. *Journal of Electrostatics*, 33(2):187–198, September 1994. ISSN 0304-3886. doi: 10.1016/0304-3886(94)90053-1.
- [13] T. B. Jones and Masao Washizu. Multipolar dielectrophoretic and electrorotation theory. *Journal of Electrostatics*, 37(1):121–134, May 1996. ISSN 0304-3886. doi: 10.1016/0304-3886(96)00006-x.
- [14] T.B. Jones. Basic theory of dielectrophoresis and electrorotation. *IEEE Engineering in Medicine and Biology Magazine*, 22(6):33–42, November 2003. ISSN 1937-4186. doi: 10.1109/MEMB.2003.1304999.
- [15] AM Benselama, P Pham, and E Canot. Modeling of the dielectrophoretic forces acting upon biological cells: A numerical comparison between finite element/boundary element maxwell stress tensor methods and point–dipole approach. In *Technical Proceedings of the NSTI Nanotechnology Conference and Trade Show 2004*, volume 1, pages 7–11, 2004. ISBN 0-9728422-7-6.
- [16] Carlos Rosales and Kian Meng Lim. Numerical comparison between Maxwell stress method and equivalent multipole approach for calculation of the dielectrophoretic force in single-cell traps. *ELECTROPHORESIS*, 26(11):2057–2065, June 2005. ISSN 1522-2683. doi: 10.1002/elps.200410298.
- [17] Hossein Nili and Nicolas G. Green. Higher-order dielectrophoresis of nonspherical particles. *Physical Review E*, 89(6):063302, June 2014. doi: 10.1103/physreve.89.063302.
- [18] Tomáš Michálek and Jiří Zemánek. Dipole and multipole models of dielectrophoresis for a non-negligible particle size: Simulations and experiments. *ELECTROPHORESIS*, 38(11):1419–1426, June 2017. ISSN 1522-2683. doi: 10.1002/elps.201600466.
- [19] Julius Adams Stratton. *Electromagnetic Theory*. John Wiley & Sons, January 2007. ISBN 978-0-470-13153-4.

-
- [20] C. Y. Yang and U. Lei. Dielectrophoretic force and torque on an ellipsoid in an arbitrary time varying electric field. *Applied Physics Letters*, 90(15):153901, April 2007. ISSN 0003-6951, 1077-3118. doi: 10.1063/1.2721398.
- [21] Nicolas G. Green and Thomas B. Jones. Numerical determination of the effective moments of non-spherical particles. *Journal of Physics D: Applied Physics*, 40(1):78, 2007. ISSN 0022-3727. doi: 10.1088/0022-3727/40/1/S12.
- [22] A. Ogbi, L. Nicolas, R. Perrussel, S. J. Salon, and D. Voyer. Numerical Identification of Effective Multipole Moments of Polarizable Particles. *IEEE Transactions on Magnetics*, 48(2):675–678, February 2012. ISSN 0018-9464. doi: 10.1109/tmag.2011.2173166.
- [23] Susan Lea. Spherical multipole moments, 2017.
- [24] See Supplemental Material at <http://link.aps.org/supplemental/10.1103/PhysRevE.99.053307> for a complete list of multipolar moments related to example in Fig. 2.
- [25] Jiří Zemánek, Tomáš Michálek, and Zdeněk Hurák. Phase-shift feedback control for dielectrophoretic micromanipulation. *Lab on a Chip*, 18(12):1793–1801, 2018. ISSN 1473-0197. doi: 10.1039/c8lc00113h.
- [26] Tao Sun, Hywel Morgan, and Nicolas G. Green. Analytical solutions of ac electrokinetics in interdigitated electrode arrays: Electric field, dielectrophoretic and traveling-wave dielectrophoretic forces. *Physical Review E*, 76(4):046610, October 2007. doi: 10.1103/PhysRevE.76.046610.
- [27] Dong Eui Chang, Sophie Loire, and Igor Mezić. Closed-form solutions in the electrical field analysis for dielectrophoretic and travelling wave inter-digitated electrode arrays. *Journal of Physics D: Applied Physics*, 36(23):3073–3078, December 2003. ISSN 0022-3727, 1361-6463. doi: 10.1088/0022-3727/36/23/032.
- [28] Martin Gurtner, Kristian Hengster-Movric, and Zdeněk Hurák. Green’s function-based control-oriented modeling of electric field for dielectrophoresis. *Journal of Applied Physics*, 122(5):054903, August 2017. ISSN 0021-8979. doi: 10.1063/1.4997725.
-

- [29] Vladimir Gauthier, Aude Bolopion, and Michaël Gauthier. Analytical Formulation of the Electric Field Induced by Electrode Arrays: Towards Automated Dielectrophoretic Cell Sorting. *Micromachines*, 8 (8):253, August 2017. ISSN 2072-666X. doi: 10.3390/mi8080253.

.....

.....



A micro-object placed at the center
of a quadrupolar electrode array

CHAPTER 4

Hydrodynamic model of arbitrarily-shaped object

In this paper, we study the electrorotational behavior of non-spherical micro-objects. We extend a control-oriented model of general dielectrophoresis to incorporate also the hydrodynamics so that we can predict the motion of non-spherical micro-objects in fluidic environments. Such mathematical (computational) model enables model-based feedback control of a position and orientation of particles by real-time (online) computation of voltages applied to the electrodes. We use the measured data from experiments with electrorotation of an artificial micro-object having a Tetris-like shape, to evaluate the performance of the proposed model. We also demonstrate the qualitative difference in behavior from the commonly performed electrorotation of a sphere advocating the necessity for model-based control. Further analysis of the simulation results for other than the experimentally explored scenarios provides additional useful insight into the electrorotational behavior of non-spherical objects.

Reprinted, with permission, from:

Tomáš Michálek, Aude Bolopion, Zdeněk Hurák, and Michaël Gauthier. Electrorotation of arbitrarily shaped micro-objects: modeling and experiments. *IEEE/ASME Transactions on Mechatronics*, pages 1–1, 2019. ISSN 1941-014X. doi: 10.1109/TMECH.2019.2959828 © 2019 IEEE

4.1 Introduction

Electrorotation (ROT), as one of the AC electrokinetic effects, provides a way to induce a rotational motion of micro-objects by an external electric field in a non-contact fashion. The background mechanism of ROT is closely related to the mechanisms of electro-orientation (EO) or dielectrophoresis (DEP) forming a family of phenomena also called as *generalized dielectrophoresis* (gDEP). First description of these phenomena were provided by Pohl in [2] and a subsequent detailed theoretical background of all the mentioned gDEP effects can be found for example in [3–6], short summary in [7] and a review of gDEP applications in [8].

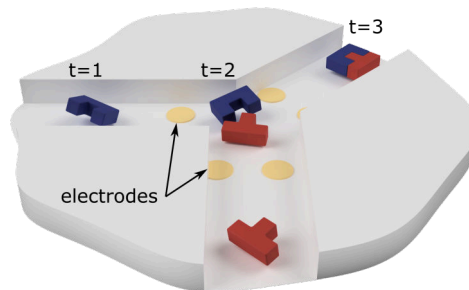


Figure 4.1: Foreseen application of gDEP—micro-electrodes at the junction of two microfluidic channels generate controlled electric field for non-contact assembly of micro-objects into the desired products.

Mostly, ROT was used in an open-loop regime for characterization of micro-objects (often biological cells) through measurements of their so-called electrorotational spectra [9–11]. In [12], a feedback system was proposed for a stochastic estimation of dielectric properties of spherical particles.

ROT can be, however, used also for a closed-loop feedback orientation control of micro-objects, similarly as the DEP was already used for their position control [13–15]. Non-contact manipulation, including both positioning and orientation, is a sought skill for example in biology or micro-assembly application domains. In [16], Jiang et al. demonstrated the feedback orientation control on a case of spherical yeast cells. Most of the objects of interest in the mentioned application domains are, however, often non-spherical (e.g., red blood cells or virus bodies in biology or completely

artificial shapes in micro-assembly). An example task solved in the field of micro-assembly is shown in Fig. 4.1. Consider a device formed by two microfluidic channels merging in a junction. Through each of these two channels, objects of two distinct shapes are conveyed to the junction where a set of microelectrodes can dielectrophoretically actuate them. Here, ROT could be used to orient suitably both of the objects, one w.r.t. the other, and DEP would simultaneously bring them near to each other so that they assemble. The finished product would then continue along the flow through the output channel.

Although the use of spheres, as the manipulated objects, is quite common in DEP and ROT experiments, when it comes to non-spherical objects the results are mostly limited to less or more prolate ellipsoids. Miller and Jones [17] used EO to characterize the electrical properties (internal conductance and permittivity) of human and llama erythrocytes. In [18], EO was used for characterization of microtubules. Both ROT and EO were used in [19] for characterization of surface conductance and permittivity of artificial SU-8 micro-rods with variously functionalized surfaces. In all of these works, the objects were approximated for analysis purposes as (possibly layered) ellipsoids. In [20], Egger, et al. derived a model for ROT of dumb-bell shaped objects (two connected spheres) and applied it in their experiments with single erythrocytes and pollen. Arcenegui et al. presented in [21] a theory for EO and ROT of slender cylindrical objects and validated it in experiments with metal nanowires. Both positive and negative DEP manipulation of rod-shaped viruses were demonstrated in [22]. A quantitative agreement with an expression for DEP force acting on a homogeneous dielectric cylinder was obtained. Apart from the experimental results, there exist several purely numerical simulation studies [23, 24].

Except for the missing theory and experiments involving objects of shapes other than spheres, ellipsoids or cylinders (often modeled as ellipsoids), it is also the hydrodynamics governing the interaction of these objects with the surrounding fluidic medium, which is usually left without discussion in gDEP experiments. Mathai et al., in their work [25] on position and orientation control using electroosmotic flows, dealt with modeling of hydrodynamic forces and torques influencing the motion of ellipsoidal objects. A complete and exhaustive treatment of hydrodynamics at low Reynolds number are given by Happel and Brenner in [26].

Contribution

In this paper, we couple our recently published control-oriented model of DEP for arbitrarily-shaped objects [27] with control-oriented model of hydrodynamics working again with arbitrarily-shaped objects based on [26]. The resulting model then allows us to predict both the translational and rotational velocities of the micro-object of interest and thus simulate its motion in a fluidic environment. Such model, evaluable in real-time (in fractions of a second), is motivated by and can be used for design and implementation of model-based control algorithms (e.g., for micro-assembly applications).

We demonstrate the performance of the model by comparing its outcomes against experimental observations. We perform an electrorotation with Tetris-shaped micro-object as a task in which both gDEP and hydrodynamics play a crucial role.

4.2 Mathematical model

The purpose of the mathematical model is to predict the motion of an arbitrarily shaped micro-object in a fluidic medium under the influence of an external electric field generated by a set of microelectrodes. Our ultimate goal is to make the model a part of a control algorithm that sets the voltages applied to the electrodes so that an object follows a planned trajectory. To this purpose, we require that the model be evaluable in real-time (in fractions of a second) similarly as in [27]. Despite its simplicity, which is necessary for its fast evaluation, such a model should still take into account all the relevant physical phenomena for accurate enough results. In our case, the electrokinetics and hydrodynamics represent the dominant effects, and we will further deal with them in the following subsections.

We will neglect the other, unobserved or not so influential, effects to keep the model fast to evaluate. A feedback controller will then compensate for the discrepancies between the model and the reality. These neglected effects include, for example, the thermally induced fluid flows or friction forces between the object and other solid parts of the experimental chamber.

4.2.1 AC electrokinetics

For actuation, we drive the micro-electrodes with harmonic signals having a frequency of 25 kHz, which is high enough to allow us to consider just the gDEP forces and torques and to neglect all the other effects like electrolysis, electroosmosis, etc [28]. We further decided to ignore any electrical interaction of the object with the walls or the bottom floor of the experimental chamber, since a sufficiently large distance separates them during the experiments.

The critical enabling principle used in gDEP is the electric polarization of the object of interest, which takes place when it is exposed to an external electric field. From the various polarization mechanisms (electronic, atomic, orientational, etc.), it is the interfacial polarization caused by a long-range charge transport in dielectrics, whose effect prevails in the AC electrokinetics applications (micro-objects located in fluidic mediums). The polarization is not instantaneous, but the charge rather gradually builds up at the outer as well as the inner interfaces of the object with speed characterized by a *relaxation time* τ (a period, in which the maximum polarization takes place).

Thus the polarization depends on the frequency of the external AC electric field. With frequencies sufficiently below $f_{co} = 1/(2\pi\tau)$, the charges manage to follow the changing field whereas with frequencies sufficiently above this threshold, they will not be able to ‘catch up’ the field at all and no polarization will take place. The frequency response is strongly influenced by the material properties of the object and the medium. At lower frequencies, these are the conductivities, which have the major influence over the polarizability. At higher frequencies, the impact of permittivity takes over. All of the above characteristics are captured in the so-called Clausius-Mossotti factor [7].

The resulting charge structure emerging at the interface of the object then interacts through Coulomb forces with the original electric field exerting forces and torques on the object itself. Based on whether the object is more polarizable than the medium (at the given frequency) or vice versa, it will be attracted to (so-called positive DEP) or repelled from (so-called negative DEP), respectively, the places of high electric field intensity. A non-spherical object will tend to orient along the electric field lines. In case of a rotating electric field that continuously changes its orientation, the object will keep rotating as the charge distribution on its interface attempts to

‘catch up’ with the field (so-called cofield rotation) or keeps being pushed ahead of the field (so-called antifield rotation) as repelled by the charges on the electrodes. These phenomena are, in the given order, the already mentioned DEP, EO, and ROT.

To compute the gDEP forces and torques, we use our recently published model described in [27], which, unlike others, can also deal with non-spherical and heterogeneous objects. It solves the following equation

$$-\nabla \cdot ((\sigma + j\omega\epsilon) \nabla V) = 0, \quad (4.1)$$

where σ represents electric conductivity, ω is the angular frequency of the harmonic electric field, ϵ is the permittivity, and $j = \sqrt{-1}$ is the imaginary unit. The following interface conditions are applied at the boundary between two different materials

$$\mathbf{n}_2 \times (\mathbf{E}_1 - \mathbf{E}_2) = 0, \quad (4.2)$$

$$\mathbf{n}_2 \cdot (\mathbf{D}_1 - \mathbf{D}_2) = \rho_s, \quad (4.3)$$

where the numerical indices denote the two interfacing media, \mathbf{n}_2 is an outward normal vector from the second medium and ρ_s is a surface charge density, \mathbf{E} is the intensity of the electric field, and \mathbf{D} is the displacement field. Equation (4.1) results from combining the equation for conservation of currents ($\nabla \cdot \mathbf{J} + \frac{\partial \rho}{\partial t} = 0$), the Gauss’s law ($\nabla \cdot \mathbf{D} = \rho$) and the equation for electric potential ($-\nabla V = \mathbf{E}$) together with the constitutive relations ($\mathbf{D} = \epsilon \mathbf{E}$), and Ohm’s law ($\mathbf{J} = \sigma \mathbf{E}$), simplified using an assumption of a harmonic electric field and as such it accounts for both the ohmic and displacement currents. Usually, time- and memory-demanding finite element method (FEM) has to be deployed.

However, by precomputing a “basis table” for the given specific object determined by its shape and constituting materials, it then provides a way for calculation of its multipolar representation in real time (in fractions of a second). As a consequence, also the gDEP force and torque can be computed this fast. An implementation of the described model is freely available at <https://goo.gl/eGZY7P>.

4.2.2 Hydrodynamics

Except for the electrokinetic forces, the other significant forces and torques that act on the object are the ones caused by hydrodynamics. As the object moves through and revolves inside the fluidic medium, it will experience

hydrodynamic drag force and torque. They not only oppose the object’s motion slowing down its translation or rotation but in case of a non-orthotropic object (it does not have three perpendicular planes of symmetry), they also couple the translational and rotational motion. From a merely translational movement at the beginning, a hydrodynamic drag torque can emerge forcing the object to rotate or vice versa—a rotational motion can propel the object throughout the fluid. This effect is the basic locomotion principle of the robotic microswimmers [29, 30].

The nonlinear partial differential Navier-Stokes equations governing the fluid flow are generally hard to solve requiring again the use of FEM. Since we aim at constructing a control-oriented model evaluable in real time, we pose a few simplifying assumptions valid for microfluidic systems. For low Reynolds numbers (small dimensions and low velocities typical for microfluidic systems) and incompressible fluids of constant viscosity μ , the governing Navier-Stokes equations simplify to the so-called Stokes flow (or creeping flow) equations [26]

$$\begin{aligned}\nabla^2 \mathbf{v} &= \frac{1}{\mu} \nabla p, \\ \nabla \cdot \mathbf{v} &= 0.\end{aligned}\tag{4.4}$$

Here, \mathbf{v} is the vector field representing fluid velocity, p is the scalar pressure field, and ∇ is the vector differential operator. Furthermore, to simplify the explanation, we first consider the fluid to be unbounded. This is reasonable if the object does not take place in close vicinity of the bottom of the chamber or its walls. We will revisit this assumption at the end of this section.

Although the Stokes flow equations are generally solvable just by using FEM, they are at least linear. Omitting the details discussed in [26], this allows us to formulate the model for hydrodynamic drag force, \mathbf{F}_{drag} , and torque \mathbf{T}_{drag} around a point O inside the object as

$$\begin{aligned}\mathbf{F}_{\text{drag}} &= -\mu \mathbf{K} \mathbf{v} - \mu \mathbf{C}_O^T \boldsymbol{\omega}, \\ \mathbf{T}_{\text{drag}} &= -\mu \mathbf{C}_O \mathbf{v} - \mu \boldsymbol{\Omega}_O \boldsymbol{\omega}.\end{aligned}\tag{4.5}$$

Here, \mathbf{v} is the translational velocity of the object, $\boldsymbol{\omega}$ is its angular speed and \mathbf{K} , \mathbf{C}_O , and $\boldsymbol{\Omega}_O$ are *translational*, *coupling* and *rotational* tensors, respectively. The choice of O is arbitrary, but if it is the center of the hydrodynamic reaction, Eq. (4.5) poses the most symmetric form (\mathbf{C}_O is then symmetric). We chose O to be at the geometric center of the object.

These tensors contain all the shape-specific information and can be computed beforehand using FEM just once for each specific shape of the object. We do so by solving Eq. (4.4) for six different sets of boundary conditions. The first three of them are

$$\mathbf{v} = v_i \text{ on } \mathcal{S}_p, \quad i = 1, 2, 3, \quad (4.6)$$

where \mathcal{S}_p denotes the surface of the object and $\mathbf{v} \rightarrow 0$ as $\mathbf{r}_O \rightarrow \infty$ with \mathbf{r}_O representing a position vector having an origin at O . We set $\mathbf{v}_1 = [1, 0, 0]^T$, $\mathbf{v}_2 = [0, 1, 0]^T$ and $\mathbf{v}_3 = [0, 0, 1]^T$ so that they correspond to translational movements of the object in a quiescent fluid along the three coordinate axes. The remaining three boundary conditions are then

$$\mathbf{v} = \boldsymbol{\omega}_i \times \mathbf{r}_O \text{ on } \mathcal{S}_p, \quad i = 1, 2, 3, \quad (4.7)$$

with $\mathbf{v} \rightarrow 0$ as $\mathbf{r}_O \rightarrow \infty$, and vector of angular velocities set as $\boldsymbol{\omega}_1 = [1, 0, 0]^T$, $\boldsymbol{\omega}_2 = [0, 1, 0]^T$ and $\boldsymbol{\omega}_3 = [0, 0, 1]^T$ corresponding to rotation of the object in a quiescent fluid about the three coordinate axes. The total computation time was under 30 min using a regular PC. We denote the individual solutions in the order in which the distinct boundary conditions were given as velocity and pressure fields \mathbf{v}^i and p^i , $i = 1, 2, \dots, 6$, respectively. Based on these, we then compute the position dependent quantities

$$\begin{aligned} \mathbf{P}_1^i &= \begin{bmatrix} -\frac{p^i}{\mu} + 2\frac{\partial v_x^i}{\partial x} \\ \frac{\partial v_y^i}{\partial x} + \frac{\partial v_x^i}{\partial y} \\ \frac{\partial v_z^i}{\partial x} + \frac{\partial v_x^i}{\partial z} \end{bmatrix}, \quad \mathbf{P}_2^i = \begin{bmatrix} \frac{\partial v_x^i}{\partial y} + \frac{\partial v_y^i}{\partial x} \\ -\frac{p^i}{\mu} + 2\frac{\partial v_y^i}{\partial y} \\ \frac{\partial v_z^i}{\partial y} + \frac{\partial v_y^i}{\partial z} \end{bmatrix}, \\ \mathbf{P}_3^i &= \begin{bmatrix} \frac{\partial v_x^i}{\partial z} + \frac{\partial v_z^i}{\partial x} \\ \frac{\partial v_y^i}{\partial z} + \frac{\partial v_z^i}{\partial y} \\ -\frac{p^i}{\mu} + 2\frac{\partial v_z^i}{\partial z} \end{bmatrix}. \end{aligned} \quad (4.8)$$

The desired tensors \mathbf{K} , \mathbf{C}_O , and $\boldsymbol{\Omega}_O$ are then obtained as

$$\begin{aligned}
\mathbf{K} &= [\mathbf{K}_1, \mathbf{K}_2, \mathbf{K}_3], \\
&\text{with } \mathbf{K}_i = - \iint_{S_p} [\mathbf{P}_1^i, \mathbf{P}_2^i, \mathbf{P}_3^i] \, dS, \\
\mathbf{C}_O &= [\mathbf{C}_1, \mathbf{C}_2, \mathbf{C}_3], \\
&\text{with } \mathbf{C}_i = - \iint_{S_p} [\mathbf{r}_O \times \mathbf{P}_1^i, \mathbf{r}_O \times \mathbf{P}_2^i, \mathbf{r}_O \times \mathbf{P}_3^i] \, dS, \\
\boldsymbol{\Omega}_O &= [\boldsymbol{\Omega}_4, \boldsymbol{\Omega}_5, \boldsymbol{\Omega}_6], \\
&\text{with } \boldsymbol{\Omega}_i = - \iint_{S_p} [\mathbf{r}_O \times \mathbf{P}_1^i, \mathbf{r}_O \times \mathbf{P}_2^i, \mathbf{r}_O \times \mathbf{P}_3^i] \, dS.
\end{aligned}$$

Please notice that although the expressions for \mathbf{C}_i and $\boldsymbol{\Omega}_i$ are the same, the tensors \mathbf{C}_O and $\boldsymbol{\Omega}_O$ will differ, because different values of indices i (and thus data from differing simulations) are used for their computation.

For cases when the object moves in the vicinity of solid obstacles (e.g., walls or bottom of the experimental chamber), we can not consider the fluid to be unbounded. In such situations, tensors \mathbf{K} , \mathbf{C}_O , and $\boldsymbol{\Omega}_O$ need to be computed repeatedly for various positions of the object w.r.t. the walls and stored in a lookup table from where they can be accessed and interpolated in real time.

Our numerical simulations for the Tetris shape revealed that below $\sim 130 \mu\text{m}$ the error in drag torque if we use the unbounded fluid assumption, is larger than 1%. Therefore we utilized the described approach to take into account the proximity of the bottom floor of the chamber when comparing the simulations to experimental behavior in section 4.5.

4.2.3 Resulting model

Now, that we know both the propulsion and frictional forces and torques caused by the electrokinetics and hydrodynamics, respectively, we can state the general model describing the motion of the object

$$\begin{aligned}
\dot{\mathbf{x}} &= \mathbf{v} \\
\dot{\mathbf{v}} &= \frac{1}{m} \mathbf{F}_{\text{DEP}} + \frac{1}{m} \mathbf{F}_{\text{sed}} - \frac{1}{m} \mathbf{F}_{\text{drag}} \\
\dot{\boldsymbol{\theta}} &= \boldsymbol{\omega} \\
\dot{\boldsymbol{\omega}} &= \mathbf{I}^{-1} \mathbf{T}_{\text{DEP}} - \mathbf{I}^{-1} \mathbf{T}_{\text{drag}},
\end{aligned} \tag{4.9}$$

where $\mathbf{x} = [x, y, z]^T$ is a vector representing the position of the center of the object, $\mathbf{v} = [v_x, v_y, v_z]^T$ is its translational velocity, $\mathbf{F}_{\text{DEP}} = [F_{\text{DEP},x}, F_{\text{DEP},y}, F_{\text{DEP},z}]^T$ is the DEP force, $\mathbf{F}_{\text{sed}} = [0, 0, (\rho_{\text{medium}} - \rho_{\text{object}}) Vg]^T$ is the sedimentation force (buoyancy and gravity effect) and $\mathbf{F}_{\text{drag}} = [F_{\text{drag},x}, F_{\text{drag},y}, F_{\text{drag},z}]^T$ is the hydrodynamic drag force. Similarly, $\boldsymbol{\theta} = [\psi, \theta, \phi]^T$ is a vector comprised of Euler angles representing the orientation of the object in space (successive rotations about the x-,y- and z-axes of the coordinate frame), $\boldsymbol{\omega} = [\omega_x, \omega_y, \omega_z]^T$ is then the rotational velocity and \mathbf{T}_{DEP} and \mathbf{T}_{drag} are the DEP and hydrodynamic drag torques, respectively. The mass of the object is $m = V\rho_{\text{object}}$, with V being the object's volume and ρ_{object} its density. Finally, ρ_{medium} is the density of the fluidic medium, g is the acceleration due to the gravity and \mathbf{I} is the object's moment of inertia.

In practice, however, the inertia of the object is negligible due to its low weight, and the object achieves its final translational and rotational velocity immediately without any noticeable transients. Analogously, the object immediately stops moving or rotating due to the DEP when the voltage applied to the electrodes is suddenly switched off. The general model represented by Eq. (4.9) can therefore be simplified using

$$\begin{aligned}\dot{\mathbf{v}} &= 0 \\ \dot{\boldsymbol{\omega}} &= 0,\end{aligned}\tag{4.10}$$

from which the steady state values of velocities follow and the new motion equations are

$$\begin{aligned}\dot{\mathbf{x}} &= \mathbf{v}_{\text{final}} \\ \dot{\boldsymbol{\theta}} &= \boldsymbol{\omega}_{\text{final}},\end{aligned}\tag{4.11}$$

where $\mathbf{v}_{\text{final}}$ and $\boldsymbol{\omega}_{\text{final}}$ are the mentioned final translational and rotational velocities occurring when all the forces and torques are balanced. This amounts to solving the following linear system of equations based on Eq. (4.5)

$$-\mu \begin{bmatrix} \mathbf{K} & \mathbf{C}_O^T \\ \mathbf{C}_O & \boldsymbol{\Omega}_O \end{bmatrix} \begin{bmatrix} \mathbf{v}_{\text{final}} \\ \boldsymbol{\omega}_{\text{final}} \end{bmatrix} = \begin{bmatrix} \mathbf{F}_{\text{drag}} \\ \mathbf{T}_{\text{drag}} \end{bmatrix} = - \begin{bmatrix} \mathbf{F}_{\text{DEP}} + \mathbf{F}_{\text{sed}} \\ \mathbf{T}_{\text{DEP}} \end{bmatrix},$$

which leads us to

$$\begin{bmatrix} \dot{\mathbf{x}} \\ \dot{\boldsymbol{\theta}} \end{bmatrix} = \frac{1}{\mu} \begin{bmatrix} \mathbf{K} & \mathbf{C}_O^T \\ \mathbf{C}_O & \boldsymbol{\Omega}_O \end{bmatrix}^{-1} \begin{bmatrix} \mathbf{F}_{\text{DEP}} + \mathbf{F}_{\text{sed}} \\ \mathbf{T}_{\text{DEP}} \end{bmatrix}.\tag{4.12}$$

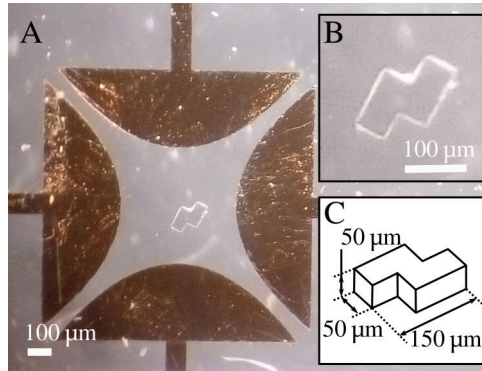


Figure 4.2: Electrode array and the micro-object having a shape of one of the Tetris pieces.

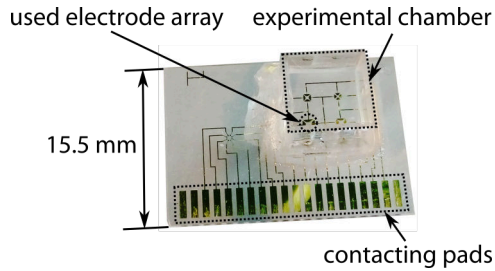


Figure 4.3: Experimental glass chip with an electrode array and a plastic basin.

4.3 Description of the used experimental setup

4.3.1 Micromanipulation workplace

To induce DEP motion, we used a quadrupolar electrode array shown in Fig. 4.2A, which is commonly used for electrorotation. It consists of four identical electrodes that are mutually rotated by 90° . They are made of gold (500 nm gold coating deposited on top of a 20 nm underlying chromium layer) on a glass substrate using a photolithography technology. The object of interest is placed in the area between the four electrodes. Around this workplace, there is a plastic basin of a square shape attached by epoxy glue. Figure 4.3 depicts the whole chip including the connection pads.

The basin is filled with ethanol and enclosed from above by a glass cov-

erslip to prevent its rapid evaporation and onset of the related fluid flows. This fluidic environment has a density just slightly lower than the density of the micro-object. This enables us to keep the micro-object levitating during the experiments in an equilibrium formed by the balance of the downwards directed sedimentation force and the upwards oriented DEP force. Therefore we do not have any friction between the micro-object and the floor of the basin, which would otherwise complicate the modeling task. Furthermore, the low conductivity of ethanol prevents the onset of electrolysis—usually unwanted phenomena occurring during DEP micromanipulation.

As the manipulated micro-object we used a Tetris-shaped piece also shown in Fig. 4.2A and magnified in Fig. 4.2B. It is made from SU-8 photoresist and have the dimensions stated in Fig. 4.2C. We use conical cotton sticks intended for cleanroom applications to manually arrange the object in place before the experiment starts.

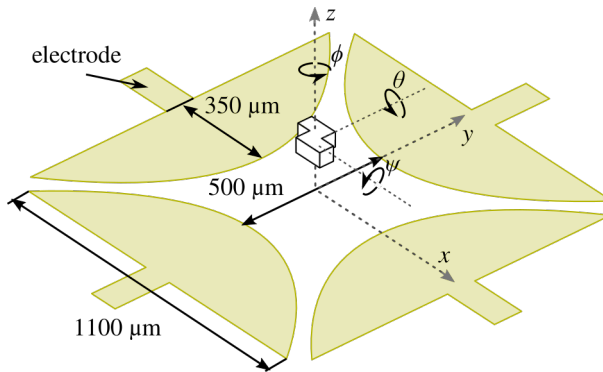


Figure 4.4: Dimensions of the electrode array and Tetris-shaped micro-object used in the validation simulations.

Figure 4.4 depicts the electrode array including its dimensions and defines the coordinate system used for the description of the micro-objects position and orientation in subsequent sections.

We summarized all the relevant physical properties of the used materials in Table 4.1.

4.3.2 Instrumentation

The glass chip with the electrode array is plugged into a spring connector, and it is placed under an optical tube with an objective (10 \times) attached to

Table 4.1: Properties of the Used Materials

Property	Value	Source
density of ethanol	785.22 kg m^{-3}	[31]
viscosity of ethanol	1.040 mPa s at 25°C	[32]
relative permittivity of ethanol	24.3 at 25°C	[33]
electrical conductivity of ethanol	$\sim 4 \mu\text{S cm}^{-1}$	measured*
density of SU-8	1190 kg m^{-3}	[34]
relative permittivity of SU-8	3.2	[35]
electrical conductivity of SU-8	$5.556 \times 10^{-11} \mu\text{S cm}^{-1}$	[35]

* using multiparameter analyzer Consort C3010

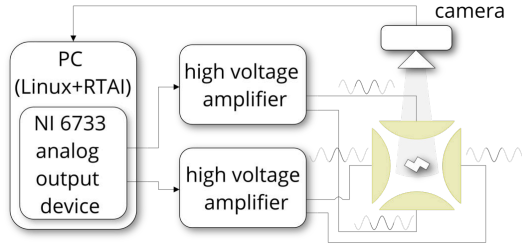


Figure 4.5: Scheme of the whole experimental setup.

its bottom and a camera to its top. The captured video is sent to a regular Linux PC and processed in real-time (we use a custom C++ application taking advantage of the real-time application interface (RTAI) and OpenCV libraries). Although the real-time requirement on image processing is not necessary for analytical purposes, it will come handy when implementing any control algorithm. Since, in the described experimental settings, the object located in the space between the electrodes rotates approximately just around the z -axis, we aim at measuring the x and y position of its center and the orientation angle ϕ with respect to time. To this purpose, we threshold the captured image, crop it and compute its centroid and the second order central moments. The centroid gives us the planar position and eigenvector associated with the largest eigenvalue of the covariance matrix

constructed from these image moments gives us the direction of greatest intensity. For a known shape this can be mapped to its orientation. For symmetrical objects, like the Tetris shape we use, special care has to be taken to solve unambiguity issues. We do so by imposing a constraint that the orientation of the object can not change abruptly.

We generate the harmonic voltage signals using NI 6733 analog output card, then amplify them by a couple of Krohn-Hite 7600M high-voltage amplifiers and finally apply them to the electrodes. In the described experiments, we used signals with a frequency $f = 25$ kHz well below the ROT peak (around $f_{\text{peak}} = 278$ kHz for the given material properties), corresponding to moderate rotational velocity of around 1.5 rad s^{-1} . At such speed, the motion of the object is still easy to analyze using a 125 fps camera. The whole setup is schematically shown in Fig. 4.5 including an indication of the voltage signals applied to the electrodes in typical ROT experiments (90° mutually shifted harmonic signals). To validate our theoretical model against the experimental observations, we will also use other values of phase-shifts, and we will also vary the amplitudes between the neighboring electrodes. Note, however, that the signals on opposite electrodes are necessarily always mutually inverted (we use normal and inverted outputs of the amplifiers) and therefore we can set neither the amplitude nor the phase-shift between individual signals independently on all the four electrodes.

4.4 Experimental observations

In the very first experiment, we placed the Tetris-shaped micro-object close to the center of the electrode array (i.e., the origin of the coordinate system) and applied four harmonic signals shifted in phase by exactly 90° to the four electrodes it consists from. As a consequence, the Tetris-shaped micro-object positions itself in the center of the electrodes and simultaneously moves upwards to a stable equilibrium where it levitates and starts rotating.

The upwards and centering motion is caused by the negative DEP force, which repels the object from high-intensity electric field regions along the edges of the electrodes. With the increasing distance from the electrodes, this force becomes weaker and at some point it is balanced by the sedimentation force. We denote this equilibrium as its levitation height. The described variation of phase on the electrodes creates a rotating electric field

inducing the ROT motion of the micro-object.

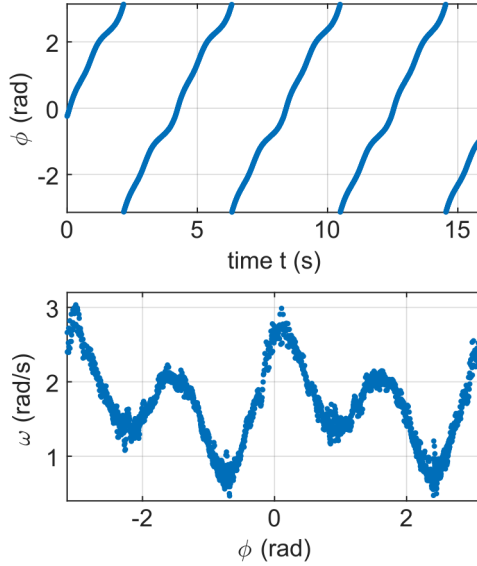


Figure 4.6: Experimentally measured rotational behavior of a Tetris-shaped micro-object using a standard electrorotational laboratory settings (four electrodes supplied with 90° -shifted harmonic voltages).

The experiment revealed that the object rotates around its vertical axis with a nonconstant rotational speed. Figure 4.6 shows the measurement of the angle ϕ and the corresponding angular velocity $\omega = d\phi/dt$ obtained by numerical differentiation. Note that we utilized the apparent periodicity of the motion and plotted ω with respect to ϕ rather than time, which will be more suitable for subsequent comparisons against the simulation outcomes. Measurements of the x and y positions of the center of the object presented in Fig. 4.7 show that apart from rotation, the object is also subjected to a slight, almost periodic, oscillatory motion in the xy -plane. Note also that the rotation did not take place precisely at the center of the electrode array (at the origin of the coordinate system). The reason for this might be a non-symmetry in the design of the experimental chamber or of the paths contacting the individual electrodes.

Nonetheless, even if the object's center point laid on the z -axis, its rotational speed would not be constant as in the case of a sphere. Although

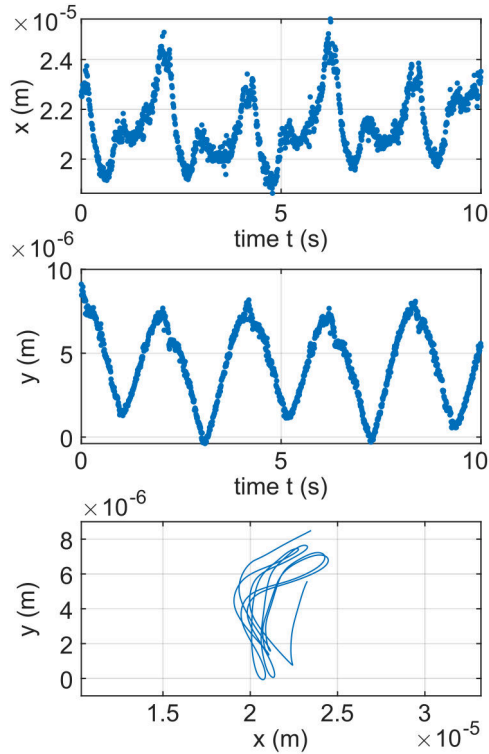


Figure 4.7: Experimentally measured x and y positions of the center of a Tetris-shaped micro-object.

the electric field is ideally rotating along the z -axis, anywhere outside this centerline the rotating character of the field deteriorates. This is apparent from Fig. 4.8, where an eccentricity of the polarizing electric field is plotted at a typical levitation height. Since the field is not precisely rotating in any neighborhood of z -axis, let alone in an area that is spanned by the micro-object of interest, the polarization of the object depends on its orientation ϕ . Therefore also the ROT torque and subsequently the angular velocity ω varies with ϕ . This is in sharp contrast with the ROT behavior of a sphere, which achieves due to its geometric symmetry always constant angular velocity. This demonstrates that even in such simple setting the resulting behavior of the micro-object might be non-trivial and every attempt for a precise and accurate control of its motion will necessarily require a suitable

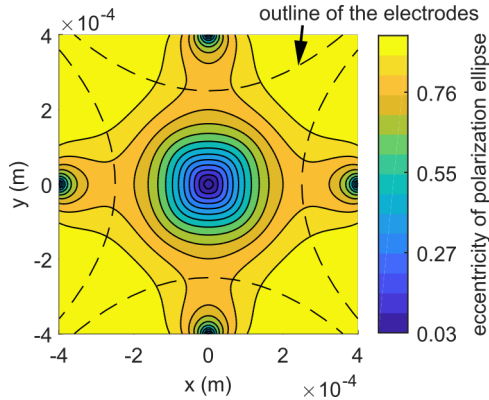


Figure 4.8: Eccentricity of the polarizing electric field at $z = 136 \mu\text{m}$. Ideally rotating electric field has eccentricity value of zero.

control-oriented model.

4.5 Comparison of model and experiments

In this section, we compare the ROT experimental measurements with the proposed control-oriented model of gDEP and hydrodynamics.

To evaluate the model and get the rotational speed of the micro-object, we need to know its position and orientation. As it was already mentioned in section 4.3.2 and presented in Figs. 4.6 and 4.7, all we can measure is just its x and y coordinates and its orientation ϕ around the z -axis. From the captured video, we also see that the orientations of the micro-object around the remaining two axes (i.e., angles ψ and θ) are zero. The z -coordinate of the micro-object (its levitation height) can not be, however, directly measured and has to be at least experimentally estimated. We did so by bringing the object to focus for two situations: while rotating and levitating, and while lying in rest at the bottom floor of the experimental chamber. Subtracting the corresponding readings on the focusing micrometer-screw and adding half of the object's thickness (since it is the position of the center of the object which we are interested in), the levitation height was determined to be around $z = 136 \mu\text{m}$. Although for this levitation height, the model outcomes agree with the experimental observations sufficiently well, it is—due to the not enough shallow depth of field of the used objective—still only

a crude estimate of the true levitation height (with deviation $\sim 10 \mu\text{m}$). A more accurate value could be obtained by applying a correction of the light refraction at the interface between the air and fluidic medium according to [36].

Since the measured x and y planar coordinates also evince a periodic behavior as it was demonstrated in the previous section, we used their averaged value for each specific orientation of the micro-object.

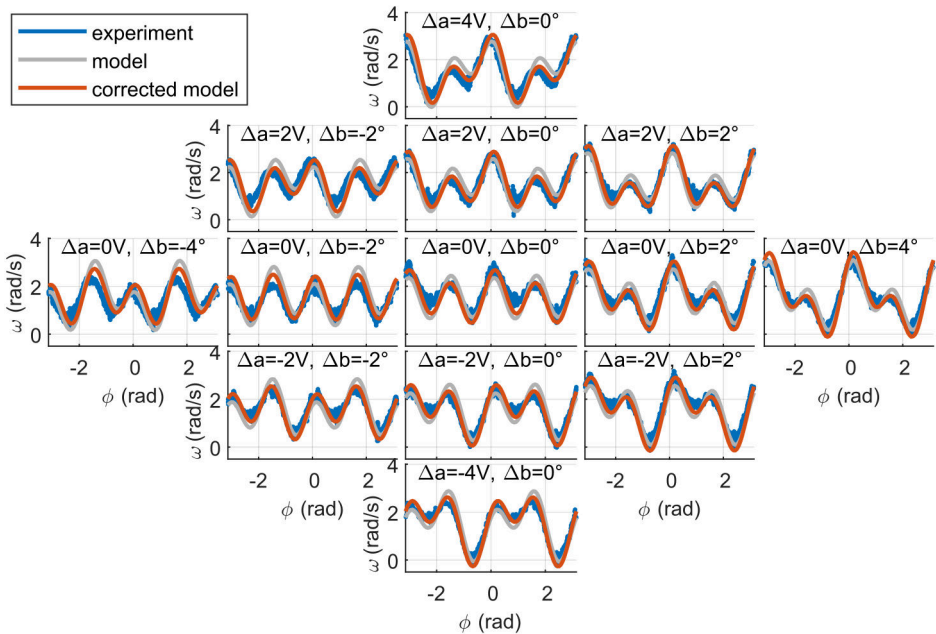


Figure 4.9: Dependence of an angular velocity of the micro-object on its orientation for a set of 13 experimental measurements and their comparison with simulation results.

The comparison is made using a set of experiments. In each of them we slightly adjust the voltage signals applied to the electrodes, which results in a different rotational behavior. The voltage waveforms were, starting from the top electrode in Fig. 4.2 and continuing in a clockwise direction, given by $(A - \frac{\Delta a}{2}) \cos(2\pi ft)$, $(A + \frac{\Delta a}{2}) \cos(2\pi ft - \frac{\pi}{2} + \Delta b \frac{\pi}{180})$, $(A - \frac{\Delta a}{2}) \cos(2\pi ft - \pi)$ and $(A + \frac{\Delta a}{2}) \cos(2\pi ft - \frac{3}{2}\pi + \Delta b \frac{\pi}{180})$, where $A = 35 \text{ V}$ is the base ampli-

tude, t represents the time and Δa and Δb are the parameters differing for each individual experiment. Δa basically introduces a difference in the amplitudes of the waveforms between the neighboring electrodes and similarly Δb changes their mutual phase-shift from the default 90° . This particular choice of the set of experiments was motivated by the need to stay close enough to the standard ROT settings and prevent the object from escaping from the center of the manipulation area. The resulting rotational behavior is shown in Fig. 4.9 always with the corresponding Δa and Δb . The individual plots are arranged such that Δa increases from the bottom to the top rows and Δb increases from the left to the right columns.

Note that for $\Delta a = \Delta b = 0$ (all the voltage signals have equal amplitude and successive 90° phase shift) the rotational velocity should be, because of the symmetry of the field and micro-object, exactly $\frac{\pi}{2}$ periodic. This holds for simulation, but not for the experiment. The model outcomes for such situation better fit the measurements made for $\Delta a = 0$ and $\Delta b = 2^\circ$ and generally also the other model outcomes better suit the measurements made for Δb increased by around 2° . We denote such better fitting model as “corrected model”. This indicates that the system is quite sensitive even to small changes of the input parameters. As a consequence, another source of the modeling discrepancies might arise also from any asymmetries in the arrangement of the electrodes (due to asymmetric design of the connection paths or fabrication imprecisions).

4.6 Simulation analysis of other scenarios

Now when we saw that the proposed model can explain the particular observed experimental behavior, we will use a simulation outcomes to analyze different possible scenarios.

Specifically, we explore how the rotational behavior of the micro-object would change with its varying levitation height. As mentioned above, the levitation height is quite sensitive to even slight variations in the properties of the used materials, mainly their densities. In Fig. 4.10 we demonstrate this for three different settings of Δb and Δa . Note that with the increasing levitation height the speed of rotation decreases since also the electric field intensity gets weaker. Depending on the particular settings, there is an interesting transitional zone at lower levitation heights (below $50\ \mu\text{m}$). If the object is levitating near the electrodes, it might not revolve, but it will

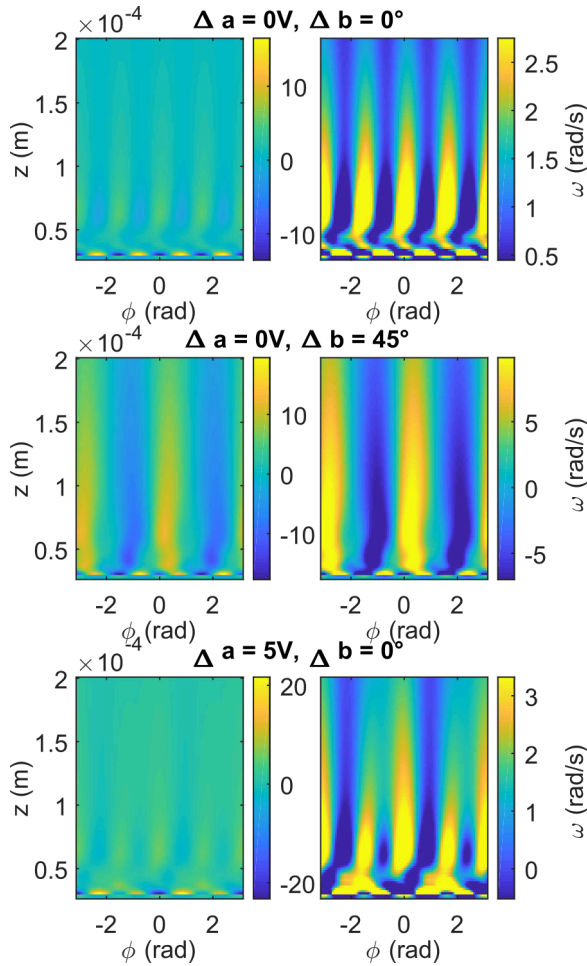


Figure 4.10: ROT torque acting on the Tetris-shaped object located on the z -axis for varying values of the z -coordinate and angle ϕ . Each row of graphs was generated using different voltages on the electrodes encoded by Δa and Δb in the respective titles. Two different color scales (unsaturated and saturated) are used for each data set to capture the behavior for lower as well as higher values of z .

rather just orient itself with respect to the electrodes by means of EO. The reason for this behavior is that here the electric field is not so nicely rotating as it is in higher levitation heights where it is weaker but smoothed out.

Experimenting with other various shapes of objects and of the electrodes, we further observed, that the spatial (w.r.t. orientation ϕ) period of angular velocity ω observed in Figs. 4.6 and 4.9 depends on both the spatial periodicity of the source electric field and on the rotational periodicity of the object's shape. Namely, it is equal to their greatest common divisor.

4.7 Conclusion

In this paper, we extended the previously developed control-oriented model of gDEP [27] for arbitrarily-shaped objects to include also the hydrodynamics. The resulting model can compute the translational and angular velocities of micro-objects under gDEP in fractions of a second.

The comparison of the simulation predictions with experimental measurements showed that the model reflects the complex ROT behavior of the Tetris-shaped micro-object.

Since the presented experimental system is very sensitive to even slight changes in the input voltage signals, any control task might be challenging. As a first step towards the simultaneous position and orientation control of micro-objects motivated by the micro-assembly and biology applications, we would like to use the presented model in a controller achieving a steady angular velocity of the arbitrarily-shaped objects.

4.8 Bibliography

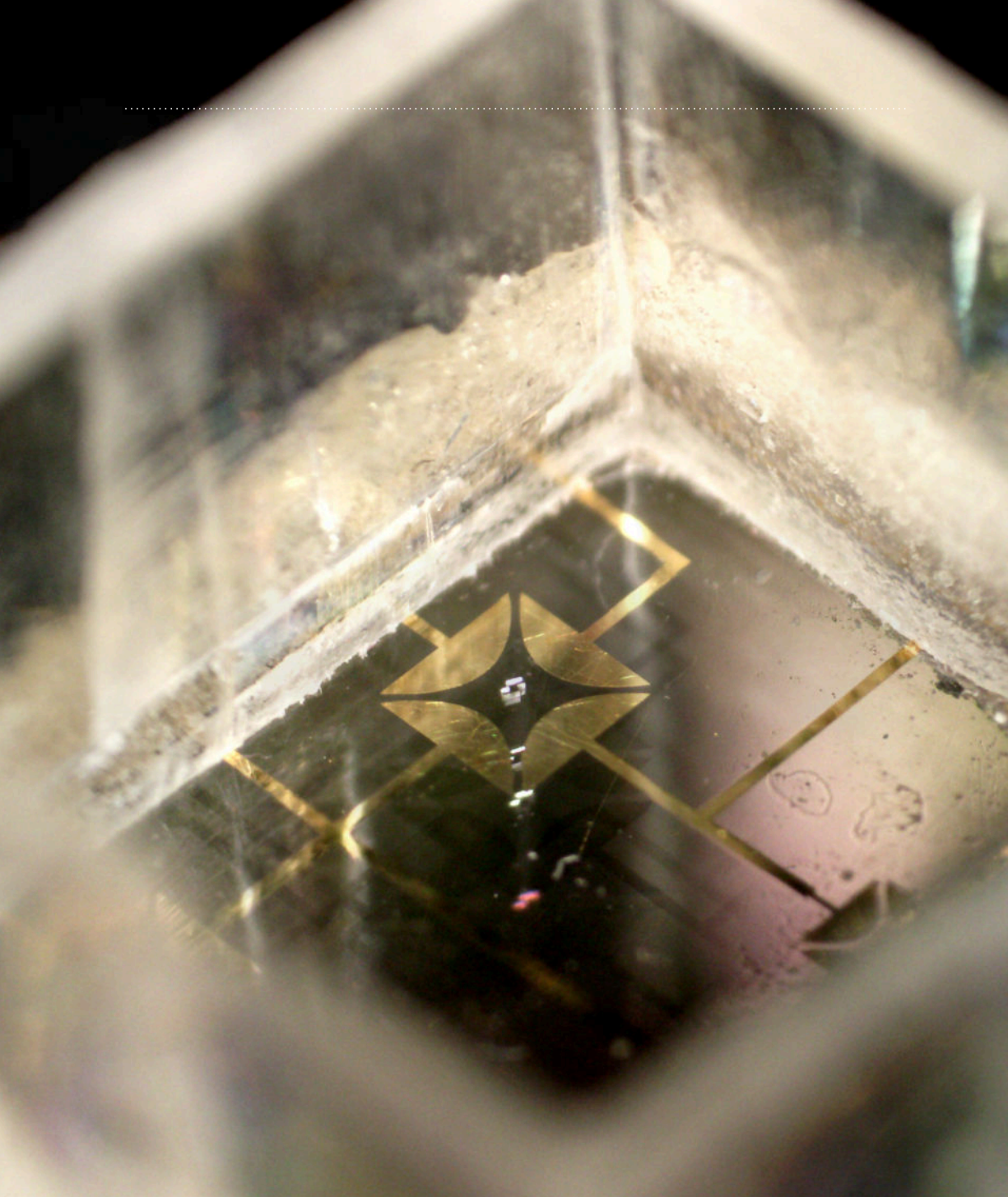
- [1] Tomáš Michálek, Aude Bolopion, Zdeněk Hurák, and Michaël Gauthier. Electrorotation of arbitrarily shaped micro-objects: modeling and experiments. *IEEE/ASME Transactions on Mechatronics*, pages 1–1, 2019. ISSN 1941-014X. doi: 10.1109/TMECH.2019.2959828.
- [2] Herbert A. Pohl. *Dielectrophoresis: The Behavior of Neutral Matter in Nonuniform Electric Fields*. Cambridge University Press, Cambridge ; New York, December 1978. ISBN 978-0-521-21657-9.

-
- [3] Hywel Morgan and Nicolas G. Green. *AC Electrokinetic: Colloids and Nanoparticles*. Research Studies Pr, Philadelphia, PA, 1st edition edition, June 2002. ISBN 978-0-86380-255-3.
- [4] Michael Pycraft Hughes. *Nanoelectromechanics in Engineering and Biology*. CRC Press, October 2002. ISBN 978-0-8493-1183-3.
- [5] Thomas B. Jones and Thomas Byron Jones. *Electromechanics of Particles*. Cambridge University Press, September 2005. ISBN 978-0-521-01910-1. doi: 10.1017/cbo9780511574498.
- [6] Ronald R. Pethig. *Dielectrophoresis: Theory, Methodology and Biological Applications*. Wiley, Hoboken, NJ, 1 edition edition, May 2017. ISBN 978-1-118-67145-0.
- [7] T.B. Jones. Basic theory of dielectrophoresis and electrorotation. *IEEE Engineering in Medicine and Biology Magazine*, 22(6):33–42, November 2003. ISSN 1937-4186. doi: 10.1109/MEMB.2003.1304999.
- [8] Ronald Pethig. Review Article—Dielectrophoresis: Status of the theory, technology, and applications. *Biomicrofluidics*, 4(2):022811, June 2010. ISSN 1932-1058. doi: 10.1063/1.3456626.
- [9] Song-I Han, Young-Don Joo, and Ki-Ho Han. An electrorotation technique for measuring the dielectric properties of cells with simultaneous use of negative quadrupolar dielectrophoresis and electrorotation. *The Analyst*, 138(5):1529, 2013. ISSN 0003-2654. doi: 10.1039/c3an36261b.
- [10] Liang Huang, Peng Zhao, Fei Liang, and Wenhui Wang. *Single-cell 3D electro-rotation*, volume 148 of *Methods in Cell Biology*, chapter Single-cell 3D electro-rotation, pages 97–116. Elsevier, Amsterdam, Netherlands, 2018. ISBN 9780128142844. doi: 10.1016/bs.mcb.2018.06.013.
- [11] Giovanni De Gasperis, XiaoBo Wang, Jun Yang, Frederick F Becker, and Peter R C Gascoyne. Automated electrorotation: dielectric characterization of living cells by real-time motion estimation. *Measurement Science and Technology*, 9(3):518–529, Mar 1998. ISSN 0957-0233. doi: 10.1088/0957-0233/9/3/029.
- [12] Prateek Benhal and J.G. Chase. System identification and stochastic estimation of dielectric properties of a spherical particle using AC-induced electro-rotation. In *2015 20th International Conference on*
-

-
- Process Control (PC)*, pages 332–337. IEEE, Jun 2015. ISBN 978-1-4673-6627-4. doi: 10.1109/pc.2015.7169985.
- [13] Jiří Zemánek, Tomáš Michálek, and Zdeněk Hurák. Phase-shift feedback control for dielectrophoretic micromanipulation. *Lab on a Chip*, 18(12):1793–1801, 2018. ISSN 1473-0197. doi: 10.1039/c8lc00113h.
- [14] Jiří Zemánek, Tomáš Michálek, and Zdeněk Hurák. Feedback control for noise-aided parallel micromanipulation of several particles using dielectrophoresis. *ELECTROPHORESIS*, 36(13):1451–1458, July 2015. ISSN 1522-2683. doi: 10.1002/elps.201400521.
- [15] M. Kharboutly, A. Melis, M. Gauthier, and N. Chaillet. 2d open loop trajectory control of a micro-object in a dielectrophoresis-based device. In *2012 IEEE International Conference on Automation Science and Engineering (CASE)*, pages 950–955, August 2012. doi: 10.1109/coase.2012.6386427.
- [16] Chuan Jiang and James K. Mills. Planar cell orientation control system using a rotating electric field. *IEEE/ASME Transactions on Mechatronics*, 20(5):2350–2358, Oct 2015. ISSN 1083-4435. doi: 10.1109/tmech.2014.2377116.
- [17] R. D. Miller and T. B. Jones. Electro-orientation of ellipsoidal erythrocytes. theory and experiment. *Biophysical Journal*, 64(5):1588–1595, May 1993. ISSN 0006-3495. doi: 10.1016/S0006-3495(93)81529-7.
- [18] Itsushi Minoura and Etsuko Muto. Dielectric measurement of individual microtubules using the electroorientation method. *Biophysical Journal*, 90(10):3739–3748, May 2006. ISSN 0006-3495. doi: 10.1529/biophysj.105.071324.
- [19] Diego Morganti and Hywel Morgan. Characterization of non-spherical polymer particles by combined electrorotation and electroorientation. *Colloids and Surfaces A Physicochemical and Engineering Aspects*, 376(1-3):67–71, Feb 2011. ISSN 0927-7757. doi: 10.1016/j.colsurfa.2010.09.031.
- [20] M. Egger, E. Donath, P. I. Kuzmin, and V. Ph. Pastushenko. Electro-rotation of dumb-bell shaped particles. *Bioelectrochemistry and Bioen-*
-

- ergetics*, 26(3):383–393, Dec 1991. ISSN 0302-4598. doi: 10.1016/0302-4598(91)85001-I.
- [21] Juan J. Arcenegui, Pablo García-Sánchez, Hywel Morgan, and Antonio Ramos. Electro-orientation and electrorotation of metal nanowires. *Physical Review E*, 88(6), Dec 2013. ISSN 1539-3755. doi: 10.1103/physreve.88.063018.
- [22] Hywel Morgan and Nicolas G. Green. Dielectrophoretic manipulation of rod-shaped viral particles. *Journal of Electrostatics*, 42(3):279–293, Dec 1997. ISSN 0304-3886. doi: 10.1016/S0304-3886(97)00159-9.
- [23] Yaling Liu, Wing Kam Liu, Ted Belytschko, Neelesh Patankar, Albert C. To, Adrian Kopacz, and Jae-Hyun Chung. Immersed electrokinetic finite element method. *International Journal for Numerical Methods in Engineering*, 71(4):379–405, Jul 2007. ISSN 0029-5981. doi: 10.1002/nme.1941.
- [24] Antonio di Biasio, Luigi Ambrosone, and Cesare Cametti. Numerical simulation of dielectric spectra of aqueous suspensions of non-spheroidal differently shaped biological cells. *Journal of Physics D Applied Physics*, 42(2):025401, Jan 2009. ISSN 0022-3727. doi: 10.1088/0022-3727/42/2/025401.
- [25] Pramod P Mathai, Andrew J Berglund, J Alexander Liddle, and Benjamin A Shapiro. Simultaneous positioning and orientation of a single nano-object by flow control: theory and simulations. *New Journal of Physics*, 13(1):013027, Jan 2011. ISSN 1367-2630. doi: 10.1088/1367-2630/13/1/013027.
- [26] John Happel and Howard Brenner. *Low Reynolds number hydrodynamics: with special applications to particulate media*. Prentice-Hall, 1965.
- [27] Tomáš Michálek, Aude Bolopion, Zdeněk Hurák, and Michaël Gauthier. Control-oriented model of dielectrophoresis and electrorotation for arbitrarily shaped objects. *Physical Review E*, 99(5):053307, May 2019. doi: 10.1103/PhysRevE.99.053307.

-
- [28] P.K. Wong, T.-H. Wang, J.H. Deval, and C.-M. Ho. Electrokinetics in micro devices for biotechnology applications. *IEEE/ASME Transactions on Mechatronics*, 9(2):366–376, Jun 2004. ISSN 1083-4435. doi: 10.1109/tmech.2004.828659.
- [29] Jake J. Abbott, Kathrin E. Peyer, Marco Cosentino Lagomarsino, Li Zhang, Lixin Dong, Ioannis K. Kaliakatsos, and Bradley J. Nelson. How should microrobots swim? *The International Journal of Robotics Research*, 28(11-12):1434–1447, Nov 2009. ISSN 0278-3649. doi: 10.1177/0278364909341658.
- [30] Stefan Klumpp, Christopher T. Lefèvre, Mathieu Bennet, and Damien Faivre. Swimming with magnets: From biological organisms to synthetic devices. *Physics Reports*, 789:1–54, Jan 2019. ISSN 0370-1573. doi: 10.1016/j.physrep.2018.10.007.
- [31] John A. Dean. *Lange’s Handbook of Chemistry*. McGraw-Hill Education, New York, US, 15 edition edition, 1998. ISBN 978-0-07-016384-3.
- [32] Database of pure component properties, . URL <https://www.thermo.com/research/kdb/hcprop/cmprch.php>.
- [33] Online database of dielectric constants of common liquids, . URL https://www.engineeringtoolbox.com/liquid-dielectric-constants-d_1263.html.
- [34] Material properties database: SU-8 photoresist, . <http://www.mit.edu/~6.777/matprops/su-8.htm>, (accessed November 2019).
- [35] Datasheet of MicroChem’s SU-8 permanent photoresists, . URL <http://microchem.com/pdf/SU-8-table-of-properties.pdf>.
- [36] T. D Visser, J. L. OUD, and G. J. BRAKENHOFF. Refractive index and axial distance measurements in 3-D microscopy. *Optik*, 90(1):17–19, 1992. ISSN 0030-4026.
-



Manipulation chamber from a
greater distance

CHAPTER 5

Manipulation of arbitrarily-shaped micro-objects

The electrokinetic effect of dielectrophoresis is a promising way of inducing forces and torques on a broad class of polarizable objects at micro- and mesoscale. We introduce a non-contact micro-manipulation technique based on this phenomenon, which is capable to simultaneously position and orient a micro-object of various shapes. A visual feedback control based on a real-time optimization-based inversion of a mathematical model from [Michálek *et al.*, *Physical Review E*, 2019, **99**, 053307] is employed. The presented manipulation approach is demonstrated in a series of experiments with Tetris-shaped SU-8 micro-objects performed on a chip with a quadrupolar electrode array. Using more electrodes, the method is readily extensible to simultaneous manipulation with multiple objects in biology and micro-assembly applications.

Manuscript in preparation as:

Tomáš Michálek and Zdeněk Hurák. Position and orientation control at micro- and mesoscales using dielectrophoresis. *arXiv:2002.08764 [cs, eess]*, February 2020. URL <https://arxiv.org/abs/2002.08764>

5.1 Introduction

Micro- and mesoscale manipulation is of a growing interest in various scientific and engineering disciplines. In biology, a precise and accurate control of both position and orientation is used, for example, in systems for single-cell analysis [2–6], single-molecule studies [7, 8], or in micro-robotics for bio-engineering applications [9–11]. It can also be used as a tool for controlled assembly of cell-encapsulating microgel structures for purposes of tissue engineering, where a complex organization of cells may be a vital issue. [12–15] Apart from this usage, the so-called micro-assembly has many envisioned applications in the industry. The emergence of miniaturized components of the so-called *hybrid micro-systems* (distinguished by their superior performance and functionality) calls for effective methods of their mass production replacing the costly manual assembly. [16]

A straightforward approach is to use the known solutions from present automated industrial assembly lines and to miniaturize them. [17–23] Either manually operated or automated, all of the existing robotic micro-grippers have to cope with many challenges, the most prominent one being the adhesion effect. Since at microscale, the surface forces dominate over the volumetric ones, the manipulation principles that are known from the macroscale, when scaled down, do not work the same way. It is generally not so problematic to grasp an object, but it is then rather hard to release it afterward. To tackle this problem, one of the approaches to the assisted release is to take an advantage of the repulsive electrokinetic forces as demonstrated by Gauthier *et al.* [24] Besides the problems with adhesion, the rigidity of the object, its material and surface properties, its specific geometry, or its fragility are the other issues that need to be considered when choosing the suitable manipulation tool. [16] Furthermore, the contact-based approaches to micromanipulation are usually hard to parallelize. All of this speaks in favor of non-contact manipulation.

There exist various physical phenomena suitable for non-contact micromanipulation, including the use of electric or magnetic fields, acoustic, hydrostatic, or optical pressure. Especially the magnetic and optical approaches [25–29] are widely used. In this paper, we focus on a *dielectrophoresis* (DEP). It is an electrokinetic phenomenon that fits nicely to the lab-on-chip paradigm as it enables the whole device to be miniaturized to a hand-held form and complements the referred approaches.

DEP enables us to impart both forces and torques on polarizable objects

through creating and “shaping” the external electric field.[30] This field, usually generated by a set of micro-electrodes driven by harmonic voltage signals, interacts with the charge distribution formed inside the polarized object through the well-known Coulomb forces. Their result is then the DEP force. We distinguish between several different DEP related phenomena: conventional DEP (cDEP), traveling wave DEP (twDEP), electroorientation, and electrorotation. The first two describe the force created by a gradient of the electrostatic pressure, and a gradient of the field’s phase, respectively. The gradient of the phase is also responsible for the last two mentioned effects, which impose a torque acting on the object. All of these phenomena are jointly termed as *general DEP* (gDEP).[31]

Feedback control of position of one or even several spherical objects using DEP, which is not limited to a finite set of cage/trap locations, has already been addressed and also experimentally demonstrated numerous times.[32–35]

Just a few studies, however, deal also with orientation or even simultaneous position and orientation control of, preferably non-spherical, objects, which is necessary for micro-assembly tasks. Jiang and Mills used visual feedback to control an orientation of spherical yeast cells in a plane.[36] Edwards *et al.* performed experiments with feedback control of orientation of gold nanowires.[37, 38] To this purpose, however, they utilize just the effect of electroorientation, which does not allow to control directly the magnitude of torque applied to the object. Our approach builds on our previous work concerning the control-oriented (fast to evaluate) mathematical model coupling both the relevant electrokinetics and hydrodynamics effects observed during electrorotation of non-spherical objects. More specifically, we presented a way for computation of the gDEP force and torque acting on an arbitrarily oriented, shaped, and heterogeneous object in fractions of a second.[39] We then extended this model by a hydrodynamic part (computable in real-time) and showed that its predictions match well the experimental observations.[40]

Contribution

In this paper, we show how such a mathematical model can be used in feedback control of a position and an orientation of arbitrary micro-objects using gDEP. We demonstrate it in experiments with a quadrupolar electrode array (typically used for electrorotation experiments) and various Tetris-

shaped micro-objects, which we steer to a randomly chosen desired locations and orientations or along predefined trajectories. Precision, accuracy, and speed of such controlled gDEP manipulation are analyzed.

Such a manipulation system has a potential to be applied for example in tissue engineering to precisely arrange microgel cell-laden structures or in drug delivery where the objects could have functionalized surfaces.

5.2 Laboratory setup

The experimental setup consists of several components: the dielectrophoretic chip, microscope equipped with a camera, personal computer (PC), and a hardware for a generation of driving voltage signals (FPGA generating square waves with adjustable phase-shift, low-pass filters, and amplifiers). Their interconnection forming a feedback loop is schematically shown in Fig. 5.1. As it is indicated in the figure, the actuation happens by applying four harmonic signals differing in phase. The amplitude, as well as frequency of the voltage signals, remain fixed; all the controller can alter are their mutual phase-shifts.

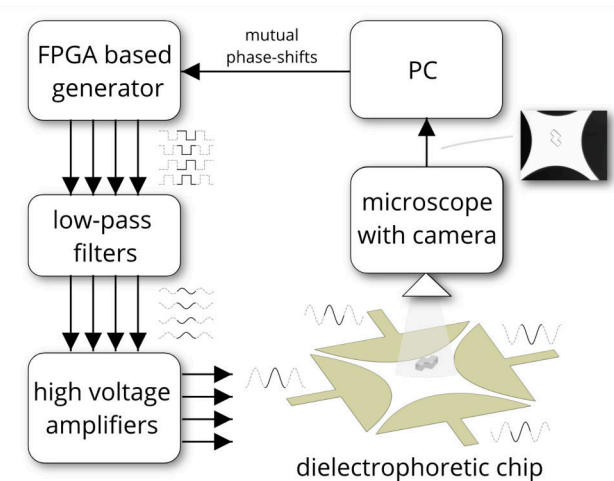


Figure 5.1: Diagram of the experimental setup showing the feedback loop.

The dielectrophoretic chip consists of a glass substrate with quadrupolar micro-electrodes (the arrangement showed in Fig. 5.1, which is typically

used for electrorotation) fabricated on its surface. They are made by a photolithography process from gold (500 nm) deposited on a thin layer of chromium (20 nm). On the top of the chip, there is attached a plastic container holding a liquid medium with a micro-object.

In this paper, we present experiments made with two different shapes of micro-objects depicted with their dimensions in Fig. 5.2. They are made by a photolithography process from a 50 μm thick layer of SU-8 photoresist. All of the microfabrication was done by FEMTO-ST Institute¹.

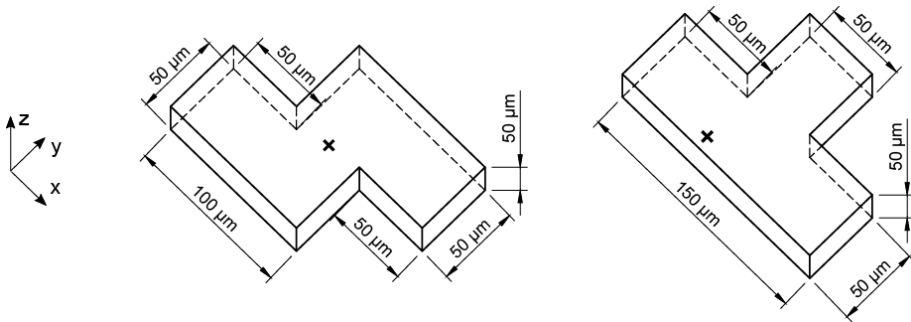


Figure 5.2: SU-8 micro-objects (called herein “S/Z”-shaped, and “T”-shaped, respectively) used in the experiments. The cross marks the point, which is used as base for measuring the object’s position and orientation.

As the medium, we use deionized water (prepared by Water Purification System Direct-Q 3) mixed with a Polysorbate 20 (Tween 20) to reduce the surface tension of water so that we can immerse the micro-objects. The used solution has an electric conductivity of $16 \mu\text{S cm}^{-1}$. The other properties of the used materials relevant for modeling of the used physical phenomena are summarized in Table 5.1.

The electrode array is placed under the microscope (Olympus BXFM) equipped with a long working distance objective $20\times/0.40$ (LMPLFLN20x) and a secondary $5\times/0.10$ (MPLN5x) objective. The first one serves as the principal one for experimental observations, while we use the second one just for calibration of coordinates (due to its greater field of view capable of also capturing the distinctive corners of the electrodes). The manipulation area is illuminated from below by a white LED panel highlighting the edges

¹FEMTO-ST Institute, AS2M department Univ. Bourgogne Franche-Comté, CNRS, 24 rue Savary, F-25000 Besançon, France.

Table 5.1: Properties of the used materials

Property	Value	Source
density of water soln.	998 kg m ⁻³	[41]
viscosity of water soln.	0.9078 mPa s at 25 °C	[41]
relative permittivity of water soln.	80	–
electrical conductivity of water soln.	~16 μS cm ⁻¹	meas.*
density of SU-8	1190 kg m ⁻³	[42]
relative permittivity of SU-8	3.2	[43]
electrical conductivity of SU-8	5.556 × 10 ⁻¹¹ μS cm ⁻¹	[43]

* using conductivity meter Jenway 4510

of the, otherwise transparent, micro-object. A secondary stereo microscope (Arsenal SZ 11-TH) situated right next to the primary one is used to prepare the sample before the experiment begins (see section 5.4.1 below for a description of the experimental procedure).

The video stream is captured by a digital camera (Basler acA1300-200um) and processed on a regular PC (Intel Core i5, 3.30 GHz, 8 GB RAM, 64-bit, Win 7). An automated image processing obtains a current position and orientation of the micro-object. The PC also runs the control algorithm (described later in section 5.3 and sends the actuation commands via USB to a signal generator. Both the image processing and controller are implemented in MATLAB software (by Mathworks) and run with a frequency of 50 Hz.

The phase-shifted voltage signals are generated by a custom programmed Altera DE0-Nano development board² (by Terasic Inc.). The phase resolution is 1°, and the output amplitude is 3.3 V, corresponding to the logic voltage levels used by the board. We use a frequency of 300 kHz, which is higher than the ROT peak of 3.74 kHz for the given combination of medium/object materials. Still, the achievable strength of gDEP forces and torques is sufficient, and yet we avoid the unwanted effects of low-frequency electroosmosis. The generated square waves are then filtered through a pair of RLC filters in series ($R=500\ \Omega$, $L=100\ \mu\text{H}$, $C=1.5\ \text{nF}$) with a cut-off frequency around 411 kHz to remove the higher-order harmonics, whose influence is not modeled for the reasons of simplicity. Another capacitor in series (100 nF) is used to remove the DC offset. The filtered signals

²<https://github.com/aa4cc/fpga-generator/>

are then connected to the inputs of four custom-made high-speed power amplifier modules QA210 (by Quintenz Hybridtechnik). Since the gains of these modules have a fixed value of 50, we adjust the amplitudes of the inputs by simple voltage dividers. The output amplitudes are this way set to be around 38 V.

5.3 Control algorithm

In order to automatically manipulate the objects in the desired way, we need to measure their current position and orientation continuously. As described above, this is done by grabbing the image by the camera mounted on a microscope and sending it to a PC running the image processing and control algorithm. Based on the difference between the actual and the desired position and orientation of the object (decided, for example, by a human operator), a desired object's translational and rotational velocity vectors are computed.

Using the hydrodynamic model, we then compute the corresponding drag forces and torques that we need to overcome, taking into account the specific orientation of the object. Taking their negative and subtracting the sedimentation force arising due to gravity and buoyancy gives us the force and torque we need to exert by gDEP. The hardest (and most computationally intensive) part of the problem is to compute the appropriate phase-shifts of the voltage signals that would accomplish this. Since the model described in our previous work[39] gives force and torque based on voltages, we need to perform the model inversion. Only then we will finally obtain the parameters of voltage signals that are afterward applied to the electrodes. This whole fully automatic process repeats with a frequency of 50 Hz. We will describe the mentioned subproblems in the following subsections in greater detail.

5.3.1 Computer vision

The actual position and orientation of the object are in real time automatically extracted from the image frames acquired by the camera on the microscope.

The captured image is at first down-sampled to 256×205 and subsequently cropped to a size of 80×80 pixels containing just the object of

interest, which is shown in Fig. 5.3(A),(B), respectively. The cropping window is centered at the location where the object was detected last time. Although it still slightly lags behind the actual position of the object, its size is chosen so that the object never leaves it. This considerable reduction of the image size makes its subsequent processing much faster.

The local variance threshold-based edge detector is then used to create a binary image (shown in Fig. 5.3(C)) discriminating, which part of the scene is the object's boundary and which it is not. The largest continuous blob of pixels making the object's boundary is used for further processing, making it robust against the occasional presence of small dust particles. Using the thresholded image also helps the detection algorithm to better cope with possible gradients in scene illumination.

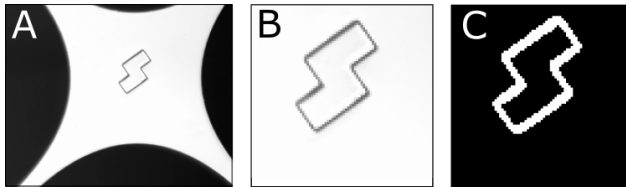


Figure 5.3: (A) Down-sampled image of the whole manipulation area obtained from a camera on a microscope. (B) Cropped segment of the image containing the object of interest. (C) Binary image showing the boundary of the object.

We then use the second-order central moments of the binary image to compute the position and orientation of the object and express them in a coordinate system defined in Fig. 5.4.[44] The average time of processing one frame is 1.2 ms.

5.3.2 Determination of the needed force and torque

As stated above, the first step is to determine the desired vectors of translational and rotational velocities, \mathbf{v} and $\boldsymbol{\omega}$, respectively. We use a proportional regulator, which makes them simply proportional to the actual errors in achieved position and orientation, respectively:

$$\begin{aligned}\mathbf{v} &= k_v (\mathbf{r}_{\text{ref}} - \mathbf{r}), \\ \boldsymbol{\omega} &= k_\omega (\phi_{\text{ref}} - \phi),\end{aligned}\tag{5.1}$$

where \mathbf{r} and ϕ are the actual measured position and orientation, respectively. Analogously, \mathbf{r}_{ref} and ϕ_{ref} are the reference position and orientation,

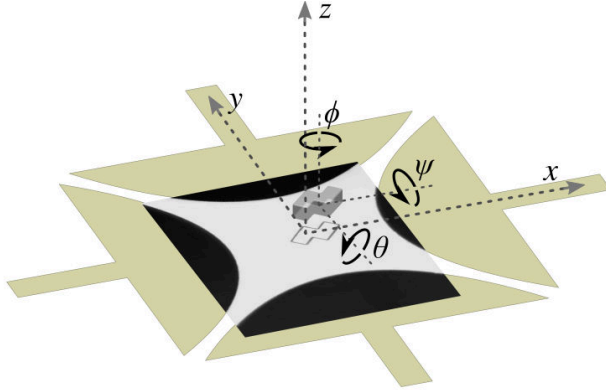


Figure 5.4: Definition of the used system of coordinates and directions of rotations.

respectively. The scalar gains were chosen to be $k_v = 50$ and $k_\omega = 10$, respectively, leading to neither too mild nor too aggressive behavior. Based on (5) from [40] (originally derived in [45]) and the discussion at the beginning of section 5.3, the gDEP forces and torques that should enforce such a motion are

$$\begin{aligned}\mathbf{F}_{\text{ref}} &= \mu\mathbf{K}\mathbf{v} + \mu\mathbf{C}_O^T\boldsymbol{\omega} - \mathbf{F}_{\text{sed}}, \\ \mathbf{T}_{\text{ref}} &= \mu\mathbf{C}_O\mathbf{v} + \mu\boldsymbol{\Omega}_O\boldsymbol{\omega},\end{aligned}\tag{5.2}$$

where μ is the dynamic viscosity of the liquid medium, \mathbf{K} , \mathbf{C}_O , and $\boldsymbol{\Omega}_O$ are *translational*, *coupling* and *rotational* tensors, respectively of the specific micro-object as described in [40]. $\mathbf{F}_{\text{sed}} = [0, 0, (\rho_m - \rho_o) Vg]^T$ is the sedimentation force incorporating both the buoyancy and gravity effect with ρ_o and ρ_m representing the density of the object and of the liquid medium respectively, V being the object's volume, and g denoting the gravitational acceleration.

5.3.3 Model inversion using optimization

The previously developed control-oriented model[39] provides us with a way to compute the gDEP force and torque acting on an object at a specified location and under the effect of particular voltages in fractions of a second. As it was already mentioned above, for control purposes, we need to invert the model so that it gives us the parameters of voltage signals provided the desired force and torque as the inputs.

Unfortunately, there does not exist any simple analytical inversion of the model, and we have to formulate it as a numerical optimization problem. For solving it, we need to repeatedly evaluate the force and torque at a given position many times (in our implementation up to ~ 2500) for various input voltage signals. Since this has to be done in every control period, which is itself merely $T = 20$ ms, the model formulation from [39] can not be directly used for this purpose.

We can, however, utilize the principle of superposition holding for electric potential (and its spatial derivatives) and reformulate the model in the same way as we showed in [32], this time including not only the expression for force but also torque and using higher-order multipolar moments (up to the 5th order). We evaluate all of the spatial derivatives of the electric field as well as all of the multipolar moments appearing in (4-5) from [39] for a set of scenarios. In each of them, an electric potential of 1 V is applied to one of the electrodes (every time a different one), while the rest of them is kept grounded. Using this basis of solutions and expressing (4-5) from [39] component-wise in a computer science convention, where a vector is considered to be an n -tuple of numbers, we get for every spatial component of force and torque a simple quadratic form

$$F_a = \tilde{\mathbf{u}}^T \mathbf{P}_a(x, y, z, \phi, \theta, \psi) \tilde{\mathbf{u}}, \quad a \in \{x, y, z\}, \quad (5.3)$$

$$T_a = \tilde{\mathbf{u}}^T \mathbf{Q}_a(x, y, z, \phi, \theta, \psi) \tilde{\mathbf{u}}, \quad a \in \{x, y, z\}. \quad (5.4)$$

Here, $\tilde{\mathbf{u}}$ is a vector of phasors representing the harmonic voltage signals applied to the individual electrodes and \mathbf{P} and \mathbf{Q} are the position and orientation dependent matrices. Such model formulation enables us to calculate force and torque at a given position for many possible variations of voltage parameters in almost no time.

Some 1.2 ms are needed to compute matrices \mathbf{P} and \mathbf{Q} for our case of four electrodes and multipoles up to the 5th order. Generally, the time t , which is needed, depends linearly on the number of electrodes $n \in \mathcal{Z}$ ($t = 0.29n + 0.083$ ms), linear regression made from measurements on the PC used for control). The biggest computational bottleneck is expressing the source electric field (and its spatial derivatives) in a rotated coordinate frame aligned with the micro-object of interest, which is needed for computation of multipolar moments (for details explaining why this operation is necessary, see [39]). In our implementation, we used a chain rule to derive the specific analytical expressions (and simplified them using a

.....

`matlabFunction`), telling us how to make this transformation. Using just-in-time (JIT) compilation in Matlab, we achieved even higher speeds than with a compiled MEX version of the same. In other cases (outside of MATLAB environment), it may be better to treat the spatial derivatives of the electric field as tensors of ascending order and utilize algorithms for (rotational) transformations of a tensor.

Having the gDEP model in a such (computationally) convenient form, we can formulate its inversion as an optimization problem. Since not all of the forces and torques are feasible to achieve, we came up with the following optimization task formulation trying to minimize various weighted error representations:

$$\begin{aligned}
 & \underset{\tilde{\mathbf{u}}}{\text{minimize}} && \frac{\mathbf{w}^T \mathbf{e}}{\|\mathbf{w}\|}, \\
 & \text{subject to} && |\tilde{u}_i| = U, \quad i = 1, \dots, 4, \\
 & && \angle \tilde{u}_i \in \left\{ 0, \frac{2\pi}{360}, \dots, 359 \frac{2\pi}{360} \right\}, \quad i = 1, \dots, 4,
 \end{aligned} \tag{5.5}$$

where $\mathbf{w} = [10, 1, 10, 1]^T$ is the vector of weights and \mathbf{e} is the vector of considered errors whose individual elements are as follows: e_1 is the percentage error in the torque direction computed as $e_1 = 100/\pi \cdot \arccos \frac{\mathbf{T}^T \mathbf{T}_{\text{ref}}}{\|\mathbf{T}\| \|\mathbf{T}_{\text{ref}}\|}$, e_2 is the percentage error in the torque magnitude computed as $e_2 = 100 \frac{\|\mathbf{T}\| - \|\mathbf{T}_{\text{ref}}\|}{\|\mathbf{T}_{\text{ref}}\|}$, e_3 is the percentage error in the direction of the force projected to xy -plane computed as $e_3 = 100/\pi \cdot \arccos \frac{F_x F_{\text{ref},x} + F_y F_{\text{ref},y}}{\sqrt{(F_x^2 + F_y^2)(F_{\text{ref},x}^2 + F_{\text{ref},y}^2)}}$, and finally e_4 is the percentage error in the z -component of the force computed as $e_4 = 100 \frac{F_z - F_{\text{ref},z}}{\|F_{\text{ref},z}\|}$. Finally, $U = 38$ represents the fixed amplitude of the voltage signals.

To solve this optimization task, we used a *simulated annealing* algorithm implemented according to [46]. It can naturally deal well with the discreteness of the set of plausible inputs, and it was much faster than the other tested global optimization solvers or their combinations (pattern search, Nelder-Mead, and BFGS Quasi-Newton method with a cubic line search procedure). The average solution time of Eq. (5.5) is 2.7 ms.

5.3.4 Achievable forces and torques

Not all of the forces, torques, and especially their specific combinations that we are demanding are feasible. Figure 5.5 show an estimate of the achievable torques rendered for one particular case of “S/Z”-shaped object located at $x = y = 0 \mu\text{m}$, and $z = 100 \mu\text{m}$ oriented with $\phi = \theta = \psi = 0 \text{ rad}$, while the gDEP force counteracts the sedimentation force. The color represents the percentage difference from this desired force. It is apparent that the mere four electrodes of the quadrupolar electrode array limit freedom of motion control severely. Still, we can achieve a lot as will be demonstrated experimentally, later on, in section 5.4. Different electrode arrays with more electrodes should achieve even better results in the future.

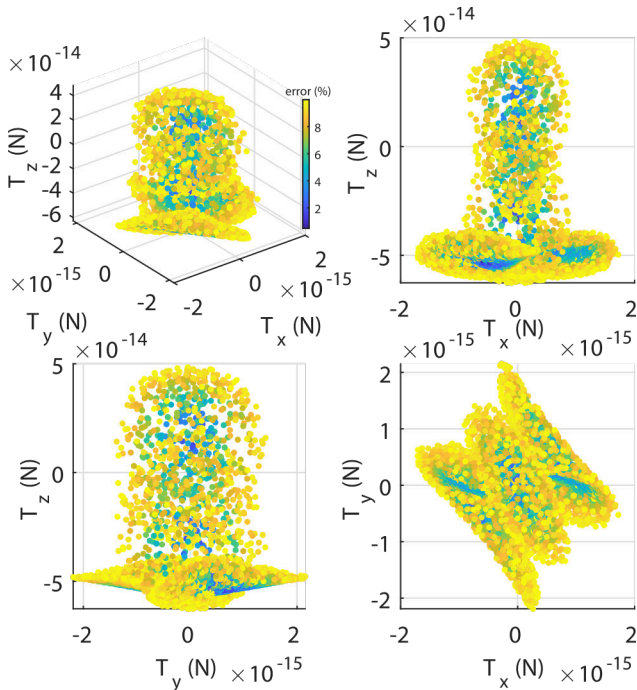


Figure 5.5: Achievable (feasible) torques for object located at $x = 0 \mu\text{m}$, $y = 0 \mu\text{m}$, $z = 100 \mu\text{m}$ with a gDEP force counteracting the sedimentation force.

5.4 Experimental results

In this section, we describe the used experimental procedure and present the measured data from tasks of the simultaneous position and orientation control, and a trajectory following.

5.4.1 Workflow of experiments

Before the beginning of every experiment, we measured the temperature of the prepared liquid medium, based on which the viscosity parameter μ of the model is adjusted.

We take advantage of the long working distance, three-dimensional view, and the zoom lenses to manually position the object in between the electrodes (using a sharpened tip of a pipette), and fill up the container with the medium. We then cover the experimental chamber by a cover glass, so that the surface of the liquid medium is flat and to prevent any further contamination of the experimental chamber by dust from the surrounding.

The electrode array is then carefully transferred below the primary microscope. Since it is not possible to repeatedly achieve exactly the same position (with a micrometer precision) of the array w.r.t. the field-view of the microscope, it is always necessary to calibrate the coordinate system. A semiautomated procedure guides the user to select a few significant and well distinguishable points in the camera image (corners of the electrode array) for computation of the image transformation. For this purpose, we use the $5\times$ magnification since the $20\times$ objective captures mainly just the space between the electrodes where nothing other, but the object is located. For this higher magnification, the obtained transformation has to be therefore adjusted afterward by scaling and by adding some small empirically determined offset in position.

An experiment starts with a short period of pure electrorotation (90° mutually phase-shifted harmonic signals are applied to the electrodes) so that the object lifts off from the ground, centers itself in the space between the electrodes, and achieves its steady levitation height.

Since we are observing the scene from the top, the current experimental arrangement does not allow us to measure the levitation height continuously and use it for control purposes. We can, however, at least get its estimate at the beginning of an experiment and then require our controller to maintain the levitation height constant (at least in an open-loop regime). The same

technique was already successfully deployed in [32]. Using the technique of axial distance measurement [47] developed in the field of 3D microscopy, we estimated the initial z -coordinate of the object to be approximately $100\ \mu\text{m}$.

In the following subsections, we will present some of the obtained experimental data demonstrating the capabilities of the manipulator.

5.4.2 Position and orientation control

In the experiment presented in Fig. 5.6, the “S/Z”-shaped object was steered in between several randomly chosen reference positions and orientations. These were always changed 3 s after the object achieved less than a $20\ \mu\text{m}$ and $\frac{\pi}{16}$ rad error in its position and orientation, respectively. Figure 5.7 shows a phased-motion created by a fusion of several camera frames being all 250 ms apart from each other representing a transition of the object between two reference positions (from approximately 7.54 s to 9.26 s of experimental footage). Figure 5.8 show the same experimental procedure for the “T”-shaped object. From the referred graphs, it is obvious that the farther the goal position of the object is from the center of the manipulation area, the harder (and thus also slower) it is for the manipulator to achieve it.

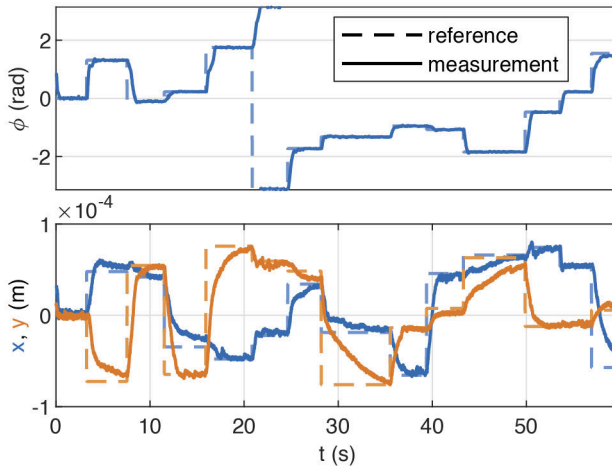


Figure 5.6: Results of the experiment with the “S/Z”-shaped micro-object moving between several randomly chosen locations and orientations.

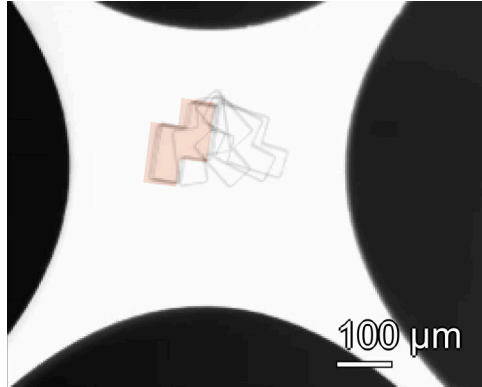


Figure 5.7: Fusion of several camera frames indicating the object’s motion (with a time-step of 250 ms). The red silhouette represents the desired goal position and orientation of the object.

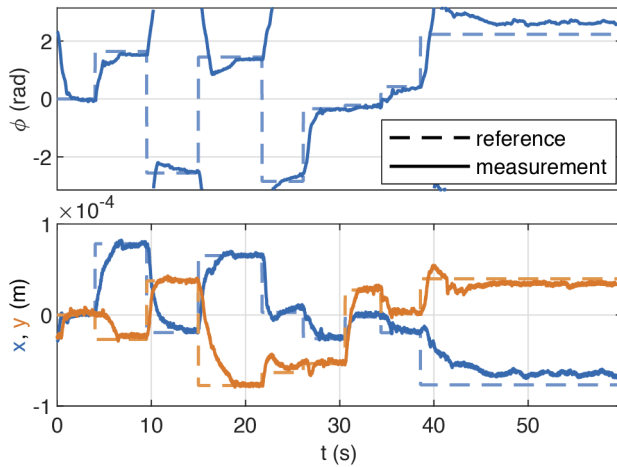


Figure 5.8: Results of the experiment with the “T”-shaped micro-object moving between several randomly chosen locations and orientations.

5.4.3 Trajectory following

By defining a sequence of mutually close reference positions, we can force an object to follow some prescribed trajectory by requiring it to pass through all points consecutively. In the experiment presented in Fig. 5.9, the “S/Z”-shaped object was steered around a circle while orienting itself so that it always remained tangent to the prescribed path.

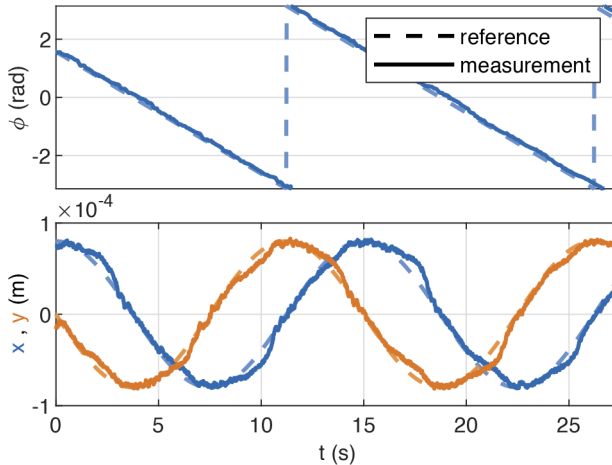


Figure 5.9: Results of the experiment with the “S/Z”-shaped micro-object following a prescribed circular trajectory.

A video from all of the above mentioned experiments is also available on-line ³.

5.4.4 Precision, accuracy and speed

We evaluated the precision and accuracy of the manipulator by a set of experiments, in which we steered the “S/Z”-shaped object to a grid of pre-defined positions and orientations over one quarter of the manipulation area (we utilize the symmetry of the electrode array to reduce the number of experiments to be done). Every experimental run started from a location $x = y = 0 \mu\text{m}$, and $z = 100 \mu\text{m}$ with an orientation $\psi = \theta = \phi = 0 \text{ rad}$. An experiment ended either if the object achieved its goal position with a small

³https://youtu.be/SBepX_Xk1BM

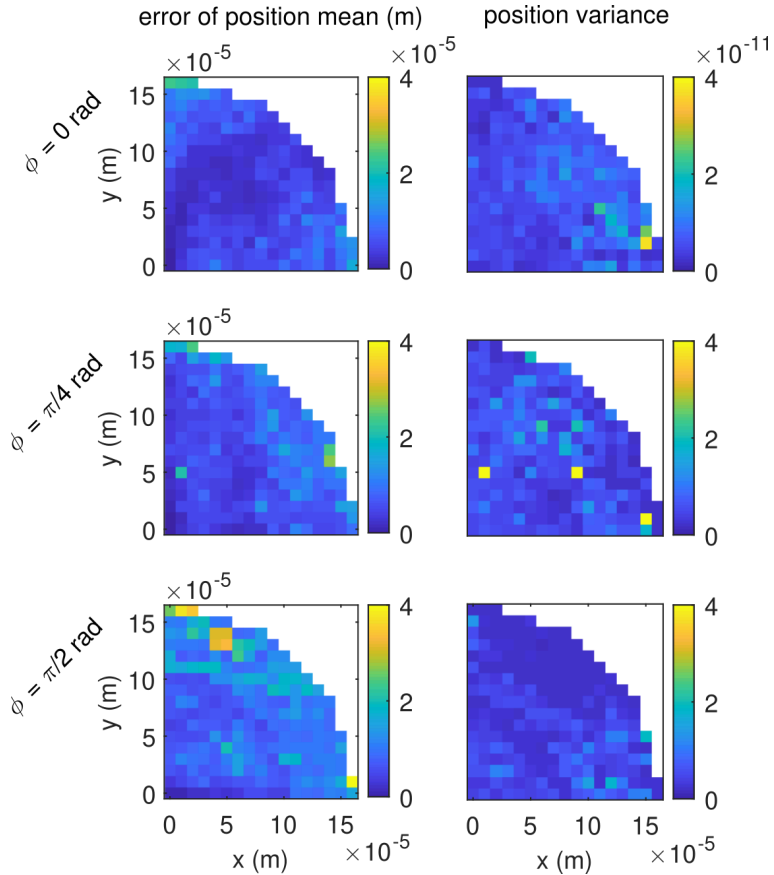


Figure 5.10: A set of measurements evaluating the precision (error of mean) of the presented micro-manipulation. The object was repeatedly steered from an initial central position ($x = y = 0 \mu\text{m}$) to a grid of positions inside a radius of approximately $150 \mu\text{m}$ above one quarter of the manipulation area (the electrode array is symmetric). This was repeated for three different orientations of the object.

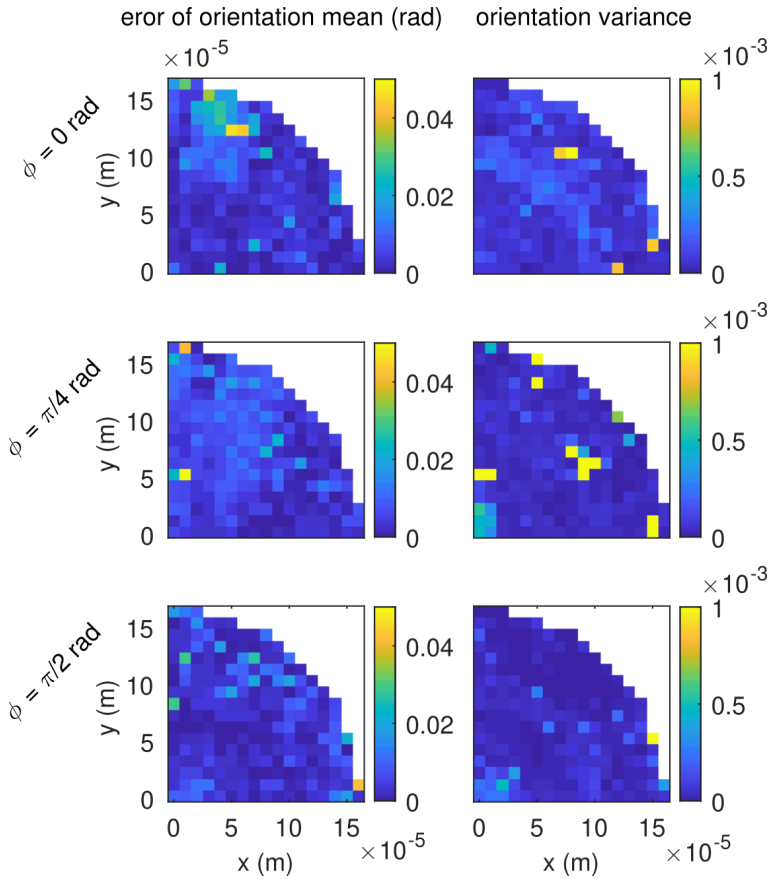


Figure 5.11: A set of measurements evaluating the accuracy (variance) of the presented micro-manipulation. The object was repeatedly steered from an initial central position ($x = y = 0 \mu\text{m}$) to a grid of positions inside a radius of approximately $150 \mu\text{m}$ above one quarter of the manipulation area (the electrode array is symmetric). This was repeated for three different orientations of the object.

enough tolerance (than it was kept there for additional 3 s) or a time limit of 20 s elapsed. The measured positions and orientation from the last 3 s of every experiment were then used to calculate the error of the mean value of position and orientation, which signify the accuracy of the manipulation and the variance of measured positions and orientations, which signify its precision. The results are shown in Fig. 5.10 and Fig. 5.11. The accuracy of positioning was most of the time around $5\ \mu\text{m}$, while the accuracy of orientation was around 0.01 rad. As can be noticed, the orientation of the object influences the accuracy of positioning. In the case of $\phi = 0$ rad, there is a notably smaller error along the y -axis, while for $\phi = \frac{\pi}{2}$ rad an error along the x -axis was smaller. Generally, the closer the boundary of the object approaches the electrodes, the less accurate the manipulation is.

Regarding the manipulation speed, the object achieved its final position (with the tolerance noted above) in 4.6 s on average, which corresponds to a manipulation speed of $\sim 22.1\ \mu\text{m s}^{-1}$.

5.5 Conclusions

We described a non-contact micro-manipulation technique based on dielectrophoresis capable of arbitrary positioning and orienting micro-object of various shapes.

The object is automatically tracked in a video stream, and the controller using real-time optimization-based inversion of the gDEP model finds the most suitable phase-shifts of the voltage signals used for actuation.

Experiments performed on a quadrupolar electrode array demonstrated the micro-manipulation capabilities of the proposed approach. The analysis of manipulation accuracy showed that the mean error in position is around $5\ \mu\text{m}$, while the error in orientation is around 0.01 rad. A video showing some of the experiments is available online at https://youtu.be/SBepX_Xk1BM.

Our solution enables us to manipulate with objects of arbitrary shapes being made from a broad class of polarizable materials and being even inhomogeneous. With a higher number, different sizes, and arrangements of electrodes, the technique is readily extensible to simultaneous manipulation with multiple and even much smaller objects. Since the manipulation is non-contact, it could also be used in closed microfluidic systems for biology or micro-assembly applications. The latter is our current research direction.

5.6 Bibliography

- [1] Tomáš Michálek and Zdeněk Hurák. Position and orientation control at micro- and mesoscales using dielectrophoresis. *arXiv:2002.08764 [cs, eess]*, February 2020. URL <https://arxiv.org/abs/2002.08764>.
- [2] Lukas Valihrach, Peter Androvic, and Mikael Kubista. Platforms for Single-Cell Collection and Analysis. *International Journal of Molecular Sciences*, 19(3):807, March 2018. doi: 10.3390/ijms19030807.
- [3] Dan Gao, Feng Jin, Min Zhou, and Yuyang Jiang. Recent advances in single cell manipulation and biochemical analysis on microfluidics. *Analyst*, 144(3):766–781, 2019. doi: 10.1039/C8AN01186A.
- [4] Tao Luo, Lei Fan, Rong Zhu, and Dong Sun. Microfluidic Single-Cell Manipulation and Analysis: Methods and Applications. *Micro-machines*, 10(2):104, February 2019. doi: 10.3390/mi10020104.
- [5] Sara Lindström and Helene Andersson-Svahn. Overview of single-cell analyses: microdevices and applications. *Lab on a Chip*, 10(24):3363–3372, December 2010. ISSN 1473-0189. doi: 10.1039/C0LC00150C.
- [6] Johan Nilsson, Mikael Evander, Björn Hammarström, and Thomas Laurell. Review of cell and particle trapping in microfluidic systems. *Analytica Chimica Acta*, 649(2):141–157, September 2009. ISSN 0003-2670. doi: 10.1016/j.aca.2009.07.017.
- [7] Yanhui Zhao, Danqi Chen, Hongjun Yue, Jarrod B. French, Joseph Rufo, Stephen J. Benkovic, and Tony Jun Huang. Lab-on-a-chip technologies for single-molecule studies. *Lab on a Chip*, 13(12):2183–2198, 2013. doi: 10.1039/C3LC90042H.
- [8] Linbo Liu, Ke Chen, Nan Xiang, and Zhonghua Ni. Dielectrophoretic manipulation of nanomaterials: A review. *ELECTROPHORESIS*, 40(6):873–889, 2019. ISSN 1522-2683. doi: 10.1002/elps.201800342.
- [9] Hakan Ceylan, Joshua Giltinan, Kristen Kozielski, and Metin Sitti. Mobile microrobots for bioengineering applications. *Lab on a Chip*, 17(10):1705–1724, 2017. doi: 10.1039/C7LC00064B.


-
- [10] Jiafeng Yao, Guiping Zhu, Tong Zhao, and Masahiro Takei. Microfluidic device embedding electrodes for dielectrophoretic manipulation of cells-A review. *ELECTROPHORESIS*, 40(8):1166–1177, 2019. ISSN 1522-2683. doi: 10.1002/elps.201800440.
- [11] Tarun Agarwal and Tapas Kumar Maiti. 20 - Dielectrophoresis-based devices for cell patterning. In Kunal Pal, Heinz-Bernhard Kraatz, Anwesha Khasnobish, Sandip Bag, Indranil Banerjee, and Usha Kuruganti, editors, *Bioelectronics and Medical Devices*, Woodhead Publishing Series in Electronic and Optical Materials, pages 493–511. Woodhead Publishing, January 2019. ISBN 978-0-08-102420-1. doi: 10.1016/B978-0-08-102420-1.00026-1.
- [12] Wenqi Hu, Kelly S. Ishii, Qihui Fan, and Aaron T. Ohta. Hydrogel microrobots actuated by optically generated vapour bubbles. *Lab on a Chip*, 12(19):3821–3826, August 2012. ISSN 1473-0189. doi: 10.1039/C2LC40483D.
- [13] S. Tasoglu, E. Diller, S. Guven, M. Sitti, and U. Demirci. Untethered micro-robotic coding of three-dimensional material composition. *Nature Communications*, 5(1):1–9, January 2014. ISSN 2041-1723. doi: 10.1038/ncomms4124.
- [14] Zeyang Liu, Masaru Takeuchi, Masahiro Nakajima, Chengzhi Hu, Yasuhisa Hasegawa, Qiang Huang, and Toshio Fukuda. Three-dimensional hepatic lobule-like tissue constructs using cell-microcapsule technology. *Acta Biomaterialia*, 50:178–187, March 2017. ISSN 1742-7061. doi: 10.1016/j.actbio.2016.12.020.
- [15] Juan Cui, Huaping Wang, Qing Shi, Tao Sun, Qiang Huang, and Toshio Fukuda. Multicellular Co-Culture in Three-Dimensional Gelatin Methacryloyl Hydrogels for Liver Tissue Engineering. *Molecules*, 24(9):1762, January 2019. doi: 10.3390/molecules24091762.
- [16] S. Ruggeri, G. Fontana, and I. Fassi. Micro-assembly. In I. Fassi and D. Shipley, editors, *Micro-Manufacturing Technologies and Their Applications*, chapter 9, pages 223–259. Springer, Cham, January 2017. ISBN 978-3-319-39651-4. doi: 10.1007/978-3-319-39651-4.
- [17] Eric Diller and Metin Sitti. Three-Dimensional Programmable Assembly by Untethered Magnetic Robotic Micro-Grippers. *Advanced*
-

- Functional Materials*, 24(28):4397–4404, 2014. ISSN 1616-3028. doi: 10.1002/adfm.201400275.
- [18] David Hériban, Michaël Gauthier, David Heriban, and Michael Gauthier. Robotic micro-assembly of microparts using a piezogripper. In *2008 IEEE/RSJ International Conference on Intelligent Robots and Systems*, pages 4042–4047. IEEE, September 2008. doi: 10.1109/IROS.2008.4650932.
- [19] C.-J. Kim, A.P. Pisano, and R.S. Muller. Silicon-processed overhanging microgripper. *Journal of Microelectromechanical Systems*, 1(1):31–36, March 1992. ISSN 1941-0158. doi: 10.1109/84.128053.
- [20] N. Chronis and L.P. Lee. Electrothermally activated SU-8 microgripper for single cell manipulation in solution. *Journal of Microelectromechanical Systems*, 14(4):857–863, August 2005. ISSN 1941-0158. doi: 10.1109/JMEMS.2005.845445.
- [21] N. Dechev, W.L. Cleghorn, and J.K. Mills. Microassembly of 3-D microstructures using a compliant, passive microgripper. *Journal of Microelectromechanical Systems*, 13(2):176–189, April 2004. ISSN 1941-0158. doi: 10.1109/JMEMS.2004.825311.
- [22] B. E. Volland, H. Heerlein, and I. W. Rangelow. Electrostatically driven microgripper. *Microelectronic Engineering*, 61-62:1015–1023, July 2002. ISSN 0167-9317. doi: 10.1016/S0167-9317(02)00461-6.
- [23] M. Kohl, B. Krevet, and E. Just. SMA microgripper system. *Sensors and Actuators A: Physical*, 97-98:646–652, April 2002. ISSN 0924-4247. doi: 10.1016/S0924-4247(01)00803-2.
- [24] M. Gauthier, E. Gibeau, and D. Heriban. Submerged Robotic Micro-manipulation and Dielectrophoretic Micro-object Release. In *Robotics and Vision 2006 9th International Conference on Control, Automation*, pages 1–6, December 2006. doi: 10.1109/icarcv.2006.345273.
- [25] Michael P. Kummer, Jake J. Abbott, Bradley E. Kratochvil, Ruedi Borer, Ali Sengul, and Bradley J. Nelson. OctoMag: An Electromagnetic System for 5-DOF Wireless Micromanipulation. *IEEE Transactions on Robotics*, 26(6):1006–1017, December 2010. ISSN 1941-0468. doi: 10.1109/TRO.2010.2073030.

-
- [26] Reza Haghighi and Chien Chern Cheah. Optical Manipulation of Multiple Groups of Microobjects Using Robotic Tweezers. *IEEE Transactions on Robotics*, 32(2):275–285, April 2016. ISSN 1941-0468. doi: 10.1109/TRO.2015.2513750.
- [27] Hsi-Wen Tung, Massimo Maffioli, Dominic R. Frutiger, Kartik M. Sivaraman, Salvador Pané, and Bradley J. Nelson. Polymer-Based Wireless Resonant Magnetic Microrobots. *IEEE Transactions on Robotics*, 30(1):26–32, February 2014. ISSN 1941-0468. doi: 10.1109/TRO.2013.2288514.
- [28] Chytra Pawashe, Steven Floyd, Eric Diller, and Metin Sitti. Two-Dimensional Autonomous Microparticle Manipulation Strategies for Magnetic Microrobots in Fluidic Environments. *IEEE Transactions on Robotics*, 28(2):467–477, April 2012. ISSN 1941-0468. doi: 10.1109/TRO.2011.2173835.
- [29] Steven Floyd, Chytra Pawashe, and Metin Sitti. Two-Dimensional Contact and Noncontact Micromanipulation in Liquid Using an Untethered Mobile Magnetic Microrobot. *IEEE Transactions on Robotics*, 25(6):1332–1342, December 2009. ISSN 1941-0468. doi: 10.1109/TRO.2009.2028761.
- [30] Herbert A. Pohl. The Motion and Precipitation of Suspensoids in Divergent Electric Fields. *Journal of Applied Physics*, 22(7):869–871, July 1951. ISSN 0021-8979. doi: 10.1063/1.1700065.
- [31] X.-B. Wang, Y. Huang, F. F. Becker, and P. R. C. Gascoyne. A unified theory of dielectrophoresis and travelling wave dielectrophoresis. *Journal of Physics D: Applied Physics*, 27(7):1571–1574, July 1994. ISSN 0022-3727. doi: 10.1088/0022-3727/27/7/036.
- [32] Jiří Zemánek, Tomáš Michálek, and Zdeněk Hurák. Phase-shift feedback control for dielectrophoretic micromanipulation. *Lab on a Chip*, 18(12):1793–1801, 2018. ISSN 1473-0197. doi: 10.1039/c8lc00113h.
- [33] Jiří Zemánek, Tomáš Michálek, and Zdeněk Hurák. Feedback control for noise-aided parallel micromanipulation of several particles using dielectrophoresis. *ELECTROPHORESIS*, 36(13):1451–1458, July 2015. ISSN 1522-2683. doi: 10.1002/elps.201400521.
-

- [34] Mohamed Kharboutly and Michaël Gauthier. High speed closed loop control of a dielectrophoresis-based system. In *2013 IEEE International Conference on Robotics and Automation*, pages 1446–1451. IEEE, May 2013. doi: 10.1109/ICRA.2013.6630761. ISSN: 1050-4729.
- [35] B. Edwards and N. Engheta. Electric tweezers: negative dielectrophoretic multiple particle positioning. *New Journal of Physics*, 14(6):063012, June 2012. ISSN 1367-2630. doi: 10.1088/1367-2630/14/6/063012.
- [36] Chuan Jiang and James K. Mills. Planar cell orientation control system using a rotating electric field. *IEEE/ASME Transactions on Mechatronics*, 20(5):2350–2358, Oct 2015. ISSN 1083-4435. doi: 10.1109/tmech.2014.2377116.
- [37] Brian Edwards, Theresa S. Mayer, and Rustom B. Bhiladvala. Synchronous Electrorotation of Nanowires in Fluid. *Nano Letters*, 6(4): 626–632, April 2006. ISSN 1530-6984. doi: 10.1021/nl0522328.
- [38] Brian Edwards, Nader Engheta, and Stephane Evoy. Electric tweezers: Experimental study of positive dielectrophoresis-based positioning and orientation of a nanorod. *Journal of Applied Physics*, 102(2):024913, July 2007. ISSN 0021-8979. doi: 10.1063/1.2753584.
- [39] Tomáš Michálek, Aude Bolopion, Zdeněk Hurák, and Michaël Gauthier. Control-oriented model of dielectrophoresis and electrorotation for arbitrarily shaped objects. *Physical Review E*, 99(5):053307, May 2019. doi: 10.1103/PhysRevE.99.053307.
- [40] Tomáš Michálek, Aude Bolopion, Zdeněk Hurák, and Michaël Gauthier. Electrorotation of arbitrarily shaped micro-objects: modeling and experiments. *IEEE/ASME Transactions on Mechatronics*, pages 1–1, 2019. ISSN 1941-014X. doi: 10.1109/TMECH.2019.2959828.
- [41] Database of pure component properties, . URL <https://www.thermo.com/research/kdb/hcprop/cmprch.php>.
- [42] Material properties database: SU-8 photoresist, . <http://www.mit.edu/~6.777/matprops/su-8.htm>, (accessed November 2019).

-
- [43] Datasheet of MicroChem's SU-8 permanent photoresists, . URL <http://microchem.com/pdf/SU-8-table-of-properties.pdf>.
- [44] Bernd Jahne. *Practical handbook on image processing for scientific and technical applications*. CRC Press, 2004. ISBN 9780849319006.
- [45] John Happel and Howard Brenner. *Low Reynolds number hydrodynamics: with special applications to particulate media*. Prentice-Hall, 1965.
- [46] S. Kirkpatrick, C. D. Gelatt, and M. P. Vecchi. Optimization by Simulated Annealing. *Science*, 220(4598):671–680, May 1983. ISSN 0036-8075, 1095-9203. doi: 10.1126/science.220.4598.671.
- [47] T. D Visser, J. L. OUD, and G. J. BRAKENHOFF. Refractive index and axial distance measurements in 3-D microscopy. *Optik*, 90(1):17–19, 1992. ISSN 0030-4026.

A close-up photograph of two small, grey, metallic-looking micro-objects resting on a surface of parallel wooden slats. The slats are illuminated from the side, creating a strong, warm, golden-brown glow and deep shadows between them. The objects are positioned in the center of the frame, one slightly above and to the left of the other. The overall composition is abstract and emphasizes texture and light.

Micro-objects for future testing of
the micro-assembly task

CHAPTER 6

Conclusion

This chapter provides a further discussion of various aspects of the presented micro-manipulation device, including those related to its possible functional extensions.

We start by presenting our attitude concerning the specific applications of the described micro-manipulator. Then we continue by addressing the specific points and current limitations that yet need to be taken into account and solved to achieve the desired goals. We conclude by summarizing the contributions of this thesis and proposing future research directions.

6.1 Envisioned applications

Although we designed and constructed the described and presented manipulation system for possible biology and engineering use, we did not focus sharply on any specific application. Instead, we developed and presented the device as a proof-of-concept tool, which capabilities were demonstrated on a fabricated task of manipulation with Tetris-shaped micro-objects.

We believe that particularly interesting applications can be found in the domain of micro-assembly. The assembled objects can be miniaturized mechanical parts for various electromechanical devices, but, for example, also the hydrogel structures containing cultivated cells for tissue engineering. However, as a lab hosted at the Faculty of electrical engineering, we have neither all the necessary conveniences nor the domain-specific knowledge at our disposal. The final tuning of the micro-manipulation task for one of these specific applications could be done in some future collaboration with scientific partners from the respective target domains.

In the subsequent sections, we discuss the possible variations and extensions of the described system that can be made on demand, and that could possibly further render some new application opportunities.

6.2 Possible functional extensions

6.2.1 Other types of micro-objects

The function and performance of the presented system were demonstrated in experiments of manipulation with artificially-made SU-8 micro-objects. In theory, the objects can be made of any material or composition of materials, and they can have any arbitrary shape as long as their shape does not change substantially in time (they should be rigid enough). Note, however, that for any combination of materials of the object and its surrounding medium, it is not guaranteed that a sufficient DEP force and torque can be generated. The computational issues related to shape complexity and material composition are discussed below in section 6.3.1.

6.2.2 Full 3D position and orientation control

Using the described control-oriented model, it should be, in theory, possible to achieve full 3D position and orientation control of the micro-objects. This was, however, not demonstrated in the experiments of the previous chapter. There, the object could revolve only around the z -axis, while its orientation around the x - and y -axes was kept fixed. Similarly, its motion was limited to a plane at a constant levitation height z .

The reasons for not implementing the full 3D position and orientation control so far are the lack of measurements and insufficient freedom of actuation. The currently used experimental setup does not provide us with real-time measurements of the current position and orientation. For measuring the levitation height z , it should be possible to adapt the twin-beam sensor described in [1, 2], which could work with minor or no modifications. The advantage of our experimental setup is that the area where the object is located is not patterned with electrodes obstructing the view. The measurement of full 3D orientation could, however, be more challenging. Here a solution similar to [3] based on a simple neural network could be used. The initial training dataset could be obtained using a ray-tracing image rendering system to avoid daunting (and maybe even impossible) manual labeling. An alternative pose detection and tracking approaches include [4–7].

6.2.3 Simultaneous manipulation with multiple objects

Similarly, as it was already shown in [8] for spherical micro-objects, it should be possible to simultaneously control the position and orientation of more than one non-spherical objects. Doing so, it should be then even possible, for example, to automatically assemble various puzzle-like objects. This all, however, assumes that mutual electrical and hydrodynamical interactions between the micro-object are either negligible or the feedback control would cope with them. Otherwise, the used control-oriented model would have to be extended to include these effects.

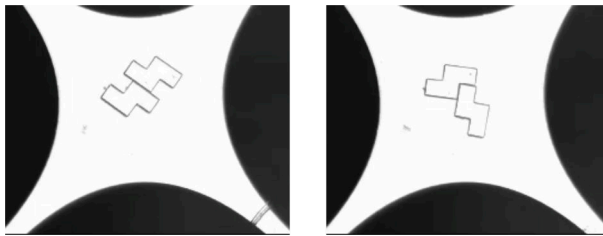


Figure 6.1: Photos from the preliminary experiments of manipulation with two non-spherical objects inside a quadrupolar electrode array.

On a software side, the presented proof-of-concept manipulation device already contains all that is necessary for doing such an experiment. The problem is, however, in the insufficient freedom of force and torque generation of the quadrupolar electrode array. By using just four electrodes for actuation, it is not possible to impose arbitrary forces and torques at any two different locations since there are limits in what electric field “profiles” can be generated. The analysis in the previous chapter even showed that for a given location and force, one could not request arbitrary torque even for a single object. Moreover, the space between the electrodes is quite limited and does not allow for larger separation distances between the objects for initial tests of manipulation. As a result, in all of the preliminary experiments, the two objects traveled to the center when they inevitably stuck one to each other and could not be otherwise than manually separated. This is shown in Fig. 6.1, where two photos from such an experiment are presented. The next step is, therefore, to try such a parallelized manipulation using an electrode array with more electrodes and thus more freedom in the “shaping” of the electric field.

6.2.4 Using more actuation electrodes

From practical reasons of physical realization, when using more electrodes, it is beneficial to arrange them differently than it is done with quadrupolar electrode array. The large distances between the electrodes required quite large voltage amplitudes to be applied to them in order to create a sufficiently strong electric field. With more electrodes, more bulky voltage amplifiers would be needed, and the whole experimental platform would become inconveniently large.

Rather than encompassing the manipulation area so that the object needs to stay always in between the electrodes, it is, therefore, better to let the object travel across them. The effect of force and torque will be furthermore much more localized. As the downside, the proximity to the electrodes means the possible presence of higher field inhomogeneities requiring usage of higher-order multipolar moments in return. Furthermore, there are computational issues related to the increasing number of electrodes themselves. These are detailed in the following section on computational limitations.

6.3 Computational limitations

A significant part of the presented work revolves around the construction of a modeling scheme, which couples the DEP and hydrodynamic effects. Making the model evaluable in real-time is the key aspect, which subsequently enables us to use it for control purposes. For assessing the feasible scale of possible future applications, it is therefore vital to know how the computational time changes when more micro-objects or more electrodes are used. Moreover, it is not only the mathematical model itself whose computational time could become prohibitively long. Similar scaling issues may arise in the tasks of image processing in the computer vision system or in the task of solving the optimization problem of model inversion.

6.3.1 Mathematical model

Several parameters are affecting the computational speed of the mathematical model. These are namely the complexity of the shape and material composition of the micro-objects, their quantity, and the number of separately driven micro-electrodes. Below, we discuss each of these individual aspects.

The intricacy of the micro-object's shape and also its proximity to the electrodes plays a crucial role in the computational complexity of the model, because it requires the usage of higher order multipolar approximation. The higher the order of the used multipolar moment is, the more computational demanding it is to compute its corresponding DEP force and torque contributions. Starting with the computation of the electric field derivatives, expressing them in a rotated frame of reference (see chapter 3), and ending by the EM calculation itself, the computational complexity of all of these tasks grows exponentially with the increasing order of used multipolar moments. This means that manipulation with micro-objects of complex shapes or with objects located in the vicinity of electrodes may be challenging. Also, the more complex the object's shape or material composition is, the longer it takes to generate the basis table for fast multipole computation. Since this is done off-line (in advance), it is, however, usually not a big problem. Because of the underlying FEM simulation and the meshing related problems, it is better if the object's aspect ratio is not too large and if any of its sharp edges are approximated by round ones. Basically, any object, for which we can simulate its polarization using FEM, is permitted.

Increasing the number of simultaneously used micro-objects does not bring such a sharp rise in computational demands. In its current form, the modeling scheme does not include any mutual electric or hydrodynamic interactions between the micro-objects, and thus its computational demands rise only linearly. The model evaluation for two identical objects lasts twice as long as for just a single object.

With more electrodes, the computation of the electric field itself also becomes more demanding. Apart from section 3.2.6 on page 59, we did not pay much attention to the way the electric field and its spatial derivatives can be efficiently calculated. For some specific situations and layouts of electrodes, there may exist simple analytical formulas, but this is not the case in most of the realistic scenarios. As described in the referred section, in a general case, we have to either utilize time and memory demanding FEM computation (whose results are additionally hard to reliably differentiate) or to settle for various degrees of approximation of the true boundary conditions. Although being in the form of analytical expressions, the results obtained by an approximate method based on Green's functions [9] are so complex that their evaluation is still prohibitively long. The only way to quickly obtain the results is, therefore, to make the calculations in advance and store the results in some form of a lookup table. By utilizing the prin-

principle of superposition [8, 10] holding for electric potential, it is sufficient to have a single lookup table for each of the electrodes and assemble the solution from their respective individual contributions. Therefore, doubling the number of electrodes also doubles the computational time required for the preparation of the lookup tables. The only performance problem that may arise here could be related to the speed of search in the lookup tables that do not fit into a RAM of the given computer. This, however, does not relate only to the number of used electrodes, but also to the spatial resolution of the stored dataset and the overall size of the manipulation area. Concerning the more important computational costs related to the online evaluation of the model, there is a linear relationship between the time t , needed for the model evaluation, and the number of electrodes $n \in \mathcal{Z}$. A linear regression from the measurements on the PC used for control resulted in the relationship $t = 0.29n + 0.083$ ms presented also in section 5.3.3 on page 109.

Therefore, although theoretically possible, many of the system extensions considered below would require further improvements in the implementation or smart usage of lookup tables. One of the ways in which it is often possible to lower the computational demands is to utilize various geometric symmetries or repeating patterns present in the system.

6.3.2 Image processing

The image processing of a single video frame using the method described in section 5.3.1 takes on average 1.2 ms. For reliable detection of more than one object, a slightly modified algorithm than the referred one has to be, however, used. Instead of determining the orientation based on the thresholded boundary of the object, it is rather the blob of its interior pixels that is analyzed. This is because if the two objects touch each other (or are too close to each other), their boundaries, as opposed to their interiors, do not form distinct entities in the thresholded binary image. This minor change, however, does not substantially increase the computational cost. Detecting the position and orientation of a couple of objects takes on average 2.5 ms and for more objects the computational cost follows the indicated linear relationship.

6.3.3 Model inversion using optimization

As described in section 5.3.3, the task of model inversion necessary for control is tackled by formulating it and solving it as an optimization problem. For a single object actuated by four electrodes, the problem has the form of Eq. (5.5). Using more electrodes increases the number of decision variables (and also constraints). Simultaneous control of more micro-objects requires an augmentation of the objective function. Moreover, the major part of the evaluation of the objective function comprises the evaluation of the model whose complexity in relation to an increasing number of electrodes and objects was discussed in the previous subsection. Adding electrodes and objects thus leads naturally to a more difficult optimization problem.

A precise evaluation of the computational demands is, however, not possible. The optimization problem at hand is non-convex, and the used randomized solvers compromise the solution speed for its quality. It is neither guaranteed that a solution at or near to the global optimum will be found nor that the solution will stay the same for two different evaluations of the same problem.

6.4 Summary of contributions

Up to now, manipulation using DEP focused mainly on spherical objects. The main contribution of this work is, therefore, the extension of the current manipulation techniques so that objects of any shape (and inner material structure) can be treated. To this purpose, a novel modeling scheme coupling DEP and hydrodynamics effects was proposed, which can be evaluated in fractions of a second. This further enabled us to use the model in a position and orientation controller utilizing its real-time inversion. This task is formulated as an optimization problem and solved in every control period.

6.5 Future research directions

The above mentioned and discussed extensions of the current experimental setup are, apart from the full 3D manipulation, precisely the ones needed for demonstration of the micro-assembly task.

Since, due to the reasons mentioned above, our preliminary experiments with two objects inside a quadrupolar electrode array were not successful, we

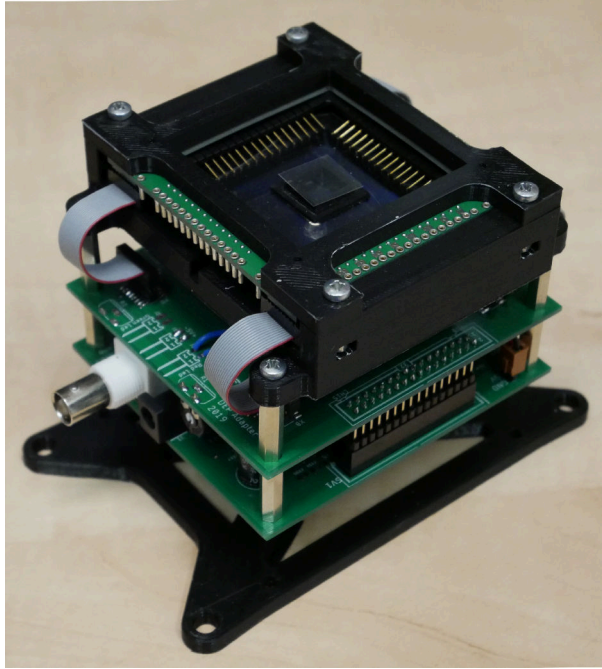


Figure 6.2: New experimental setup for manipulation with multiple non-spherical micro-objects. Several stacked printed circuit boards and 3D printed holders are used to form a compact device including the electrode array, its illumination, board with drivers, and the multi-channel generator of phased-shifted voltage signals controllable by PC.

are building a novel, better adapted, platform with more electrodes. Here, a so-called four-sector electrode array introduced in [8] will be utilized. The electrodes are made of indium-tin-oxide (ITO) to maintain the transparency of the array and enable observation of the object with back illumination. The photo of this setup is shown in Fig. 6.2.

Part of another alternative experimental setup is shown in Fig. 6.3. A printed circuit board technology was used to manufacture several electrode arrays with various arrangements of electrodes suitable for pairwise micro-assembly experiments.

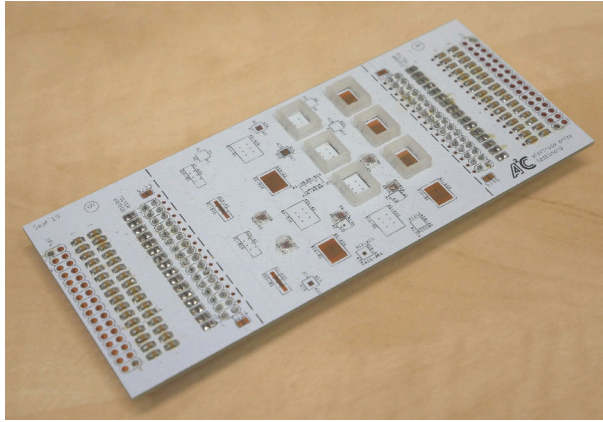


Figure 6.3: A standard printed circuit board technology was used to create a board with many various layouts of electrodes for testing the micro-assembly task.

6.6 Bibliography

- [1] Martin Gurtner and Jiří Zemánek. Twin-beam real-time position estimation of micro-objects in 3D. *Measurement Science and Technology*, 27(12):127003, November 2016. ISSN 0957-0233. doi: 10.1088/0957-0233/27/12/127003.
- [2] Martin Gurtner. Real-time optimization-based control and estimation for dielectrophoretic micromanipulation. Master’s thesis, Czech Technical University in Prague, Prague, Czech Republic, 2016.
- [3] P. Wunsch, S. Winkler, and G. Hirzinger. Real-time pose estimation of 3D objects from camera images using neural networks. In *Proceedings of International Conference on Robotics and Automation*, volume 4, pages 3232–3237 vol.4, April 1997. doi: 10.1109/robot.1997.606781. ISSN: null.
- [4] Henning Tjaden, Ulrich Schwanecke, and Elmar Schomer. Real-time monocular pose estimation of 3d objects using temporally consistent local color histograms. In *Proceedings of the IEEE International Conference on Computer Vision*, pages 124–132, 2017.
- [5] Stefan Hinterstoisser, Vincent Lepetit, Slobodan Ilic, Pascal Fua, and Nassir Navab. Dominant orientation templates for real-time detection

- of texture-less objects. In *2010 IEEE Computer Society Conference on Computer Vision and Pattern Recognition*, pages 2257–2264, June 2010. doi: 10.1109/cvpr.2010.5539908. ISSN: 1063-6919.
- [6] Martin Sundermeyer, Zoltan-Csaba Marton, Maximilian Durner, Manuel Brucker, and Rudolph Triebel. Implicit 3D Orientation Learning for 6D Object Detection from RGB Images. In *Proceedings of the European Conference on Computer Vision (ECCV)*, pages 699–715, 2018.
- [7] Reyes Rios-Cabrera and Tinne Tuytelaars. Discriminatively Trained Templates for 3D Object Detection: A Real Time Scalable Approach. In *Proceedings of the IEEE international conference on computer vision*, pages 2048–2055, 2013.
- [8] Jiří Zemánek, Tomáš Michálek, and Zdeněk Hurák. Phase-shift feedback control for dielectrophoretic micromanipulation. *Lab on a Chip*, 18(12):1793–1801, 2018. ISSN 1473-0197. doi: 10.1039/c8lc00113h.
- [9] Martin Gurtner, Kristian Hengster-Movric, and Zdeněk Hurák. Green’s function-based control-oriented modeling of electric field for dielectrophoresis. *Journal of Applied Physics*, 122(5):054903, August 2017. ISSN 0021-8979. doi: 10.1063/1.4997725.
- [10] Jiří Zemánek, Tomáš Michálek, and Zdeněk Hurák. Feedback control for noise-aided parallel micromanipulation of several particles using dielectrophoresis. *ELECTROPHORESIS*, 36(13):1451–1458, July 2015. ISSN 1522-2683. doi: 10.1002/elps.201400521.

Summary

Micro-manipulation is a task naturally needed in scientific exploration as well as novel biomedical and engineering applications. Because of the scaling laws, the micro-world is dominated by different physical phenomena than are those we are accustomed to from macro-world. Therefore it is hard or even impossible to employ there the same manipulation principles and it is necessary to search for other possible solutions.

There have been proposed many inventive micro-manipulation principles taking advantage of different physical phenomena, out of which DEP is the one, treated in this thesis. As a bio-friendly non-contact approach (there is not any tool touching the object of interest), it is already used for many task in biology and medicine as discussed in **chapter 1**. These, however, utilize so far just a fraction of its capabilities. By introducing feedback control, there is a potential for further extension of the already long list of DEP applications.

This work performed a next step towards this goal. We proposed a control-oriented modeling scheme capable to handle arbitrarily-shaped and also non-homogeneous objects and integrating it inside a control algorithm we were able to achieve simultaneous position and orientation control of micro-objects. We demonstrated this in a series of experiments, with various “Tetris”-shaped artificial micro-objects paving the way for future micro-assembly applications.

In **chapter 2** we analyzed the behavior and accuracy of the EM model compared to the reference MST solution in cases, when the inhomogeneity of the electric field at the object’s location was not negligible. Spherical objects of various sizes were used, for which the computation of higher-level multipolar approximations can be done analytically. Although the use of quadrupolar approximation proved to improve the resulting force prediction, the octupolar model yielded almost no further improvement. Furthermore, we showed that not only the location of the so-called field nulls but also the location of nulls in higher-order derivatives of electric field create naturally large relative errors in force. Interestingly, some of these depend on the type of the used potential boundary conditions. For approximate (trapezoidal)

boundary conditions, the errors between EM models with various levels of approximation lowered, while the error w.r.t. MST increased. Experiments on a parallel DEP manipulator showed that as the source of even greater errors should be considered the other non-modeled phenomena.

Chapter 3 described how the previously analyzed EM model can be extended so that fast calculation of DEP forces and torques would be possible also for non-spherical and inhomogeneous objects. This is necessary for the further usage of the model in most of the control applications. The orthonormality of spherical harmonics was used to extract the multipolar moments from a numerical FEM simulation of the polarized object. Forming a basis of such moments for a set of external electric fields, results for all of the other fields can be obtained by superposition in fractions of a second. Having the moments, calculation of gDEP force and torque using EM is similarly fast. The proposed model was successfully validated against reference numerical solutions obtained using the MST method.

This modeling scheme was later on extended by a fast-to-compute hydrodynamical model presented in **chapter 4**. At low Reynolds numbers, a series of simplifying assumptions can be made rendering the resulting set of governing equations to be linear. This, once again, enables to utilize the principle of superposition to speed-up subsequent model evaluations. The extended model provides a way for real-time prediction of the translational and rotational velocity of the micro-object in a liquid medium.

Finally, **chapter 5** describes the first experiments with simultaneous position and orientation control of Tetris-shaped artificial objects using dielectrophoresis. The presented manipulation system is based on visual feedback control with real-time optimization-based inversion of the previously introduced model. A video footage showing some of the performed experiments is available online at https://youtu.be/SBepX_Xk1BM. The achieved mean error in position was around 5 μm , while the error in orientation was around 0.01 rad.

In the last **chapter 6**, we critically discuss the limitations of the presented proof-of-concept manipulation system and highlight its known bottlenecks. We also assess the feasibility of various system extensions and outline the subsequent possible research directions.

List of publications

Journal papers

- Tomáš Michálek, Aude Bolopion, Zdeněk Hurák, and Michaël Gauthier. Electrorotation of arbitrarily shaped micro-objects: modeling and experiments. *IEEE/ASME Transactions on Mechatronics*, pages 1–1, 2019. ISSN 1941-014X. doi: 10.1109/TMECH.2019.2959828
- Tomáš Michálek, Aude Bolopion, Zdeněk Hurák, and Michaël Gauthier. Control-oriented model of dielectrophoresis and electrorotation for arbitrarily shaped objects. *Physical Review E*, 99(5):053307, May 2019. doi: 10.1103/PhysRevE.99.053307
- Jiří Zemánek, Tomáš Michálek, and Zdeněk Hurák. Phase-shift feedback control for dielectrophoretic micromanipulation. *Lab on a Chip*, 18(12):1793–1801, 2018. ISSN 1473-0197. doi: 10.1039/c8lc00113h
- Tomáš Michálek and Jiří Zemánek. Dipole and multipole models of dielectrophoresis for a non-negligible particle size: Simulations and experiments. *ELECTROPHORESIS*, 38(11):1419–1426, June 2017. ISSN 1522-2683. doi: 10.1002/elps.201600466
- Jiří Zemánek, Tomáš Michálek, and Zdeněk Hurák. Feedback control for noise-aided parallel micromanipulation of several particles using dielectrophoresis. *ELECTROPHORESIS*, 36(13):1451–1458, July 2015. ISSN 1522-2683. doi: 10.1002/elps.201400521

In preparation

- Tomáš Michálek and Zdeněk Hurák. Position and orientation control at micro- and mesoscales using dielectrophoresis. *arXiv:2002.08764 [cs, eess]*, February 2020. URL <https://arxiv.org/abs/2002.08764>

Conference papers in Web of Science

- Josef Matouš, Adam Kollarčík, Martin Gurtner, Tomáš Michálek, and Zdeňek Hurák. Optimization-based Feedback Manipulation Through an Array of Ultrasonic Transducers. *IFAC-PapersOnLine*, 52(15):483–488, January 2019. ISSN 2405-8963. doi: 10.1016/j.ifacol.2019.11.722

Other conference contributions

- J. Zemánek, T. Michálek, and Z. Hurák. Real-time optimization-based control of phase shifts for planar dielectrophoretic micromanipulation. Dielectrophoresis 2016 Conference, 2016
- T. Michálek and J. Zemánek. Comparison of several control-oriented models for dielectrophoresis against maxwell stress tensor predictions and their experimental verification. Dielectrophoresis 2016 Conference, 2016
- T. Michálek, M. Gurtner, J. Zemánek, and Z. Hurák. Overview of research in non-contact manipulation using dielectrophoresis at ctu in prague. 21st International conference on Process Control, 2017
- J. Křivánková, F. Foret, T. Michálek, and Z. Hurák. Microfluidic device for dielectrophoretic droplet sorting. International Conference Analytical Cytometry IX, 2017
- J. Zemánek, T. Michálek, M. Gurtner, and Z. Hurák. Feedback-controlled dielectrophoretic micromanipulation. International Conference on Manipulation Automation and Robotics at Small Scales, 2018
- T. Michálek, A. Bolopion, Z. Hurák, and M. Gauthier. Noncontact micromanipulation using dielectrophoresis - controlled rotation combined with positioning. 22nd International conference on Process Control, 2019
- J. Matouš, A. Kollarčík, M. Gurtner, T. Michálek, and Z. Hurák. Optimization-based feedback manipulation through an array of ultrasonic transducers. 22nd International conference on Process Control, 2019

-
- T. Michálek, Z. Hurák, A. Bolopion, and M. Gauthier. Feedback controlled dielectrophoresis high-accuracy translation and rotation at micro and meso scales. International Conference on Manipulation Automation and Robotics at Small Scales 2019, 2019

Acknowledgements

Here, I would like to express my gratitude to all the people who significantly helped me on my way during my Ph.D. studies.

First of all, I would like to thank my doctoral advisor Zdeněk Hurák for numerous precious technical, professional, and personal advice. He did the best in arranging meetings with the domain leaders as well as also in providing financial support above the fundamental scholarship. Without him, finishing this work would not be possible.

Next, I would like to thank Jiří Zemánek, my early undergraduate supervisor and later my colleague and friend, for inspiring and influencing me in many different ways. I thank Martin Gurtner, my doctoral fellow fighter, and Filip Richter, a skillful engineer, for helping me quite a few times with various strongly technical issues. Spending time in a friendly and so inspiring atmosphere with you guys is, however, what I appreciate the most.

I thank Aude Bolopion and Michaël Gauthier for a warm wellcome on my stay in Besançon, France. They directed me to an exciting research problem discussed in this thesis.

I want to thank also my wife, Pavlína, for always providing me with strong support when I need it the most. Last but not least, my thanks also belong to my family and friends. Without the great support of my parents, it would be hard to study at university at all for me.

Acknowledgements

About the author

Tomáš Michálek was born on the 14th of July 1990 in Pardubice and spent all of his childhood in Chrudim. After finishing primary school, he attended electrotechnical secondary school in Pardubice. There, he graduated with a specialization in information technology in June 2010.

After that, he started his bachelor in a study program of Cybernetics and robotics (study branch of Control systems and automation) at Czech Technical University in Prague. He followed up with his studies there and obtained a master's diploma in June 2015. His thesis, already revolving about the phenomenon of dielectrophoresis, won a dean's prize for an excellent diploma thesis, and its parts were published as journal papers. From summer 2012, he partially collaborated with the research group of Advanced Algorithms for Control and Communication (AA4CC) lead by Zdeněk Hurák, where he, later on, became a research technician.

In February 2016, Tomáš Michálek started his Ph.D. studies under the guidance of Zdeněk Hurák. Apart from ordinary courses, he took a summer school on MPC lead by J. M. Maciejowski and organized by European Embedded Control Institute (EECI). He presented his work at a few international conferences. During his studies, he also spent 4 months at a research internship at FEMTO-ST Institute in Besançon, France. Here, under the guidance of Aude Bolopion and Michaël Gauthier, he started to work on mathematical modeling of dielectrophoretic forces for non-spherical objects resulting in an extended collaboration and several journal publications. The work initiated here culminated later on in this thesis.



